ABSTRACT

Title of Dissertation:	INVESTIGATION OF THE EFFECT OF FLY ASH VARIABILITY ON CEMENT PASTE MICROSTRUCTURE AND MECHANICAL PROPERTIES USING SIMULATED FLY ASH
	Samuel Amuasi Essien, Doctor of Philosophy, 2021
Dissertation directed by:	Amde M Amde, Professor Department of Civil and Environmental Engineering

The cement and concrete industry is responsible for about 5% of global anthropogenic CO_2 emissions, and the largest source of CO_2 emissions from carbonate decompositions. Fly ash can be used as a partial replacement of cement in concrete. However, the heterogeneity of fly ash poses a challenge to its optimal utilization in concrete. Traditionally, the classification of fly ash for use in concrete is based on bulk chemical composition. This classification does not account for the inherent variability in the fly ash glass, which is the main reactive component of fly ash and a major determinant of its performance in concrete.

This research utilizes simulated fly ash modeled after a real fly ash to investigate the effect of the variation of the fly ash glass chemical composition on the performance of the fly ash, while other major properties are held constant. The chemical compositions of several thousands of individual particles from a Coal Creek, IA source fly ash was determined by computer-controlled SEM (CCSEM). The particle data was then grouped into four clusters having relatively narrow ranges of composition. A set of four synthetic fly ash glasses were prepared based on the mean chemical composition of each cluster. Three simulated whole fly ashes were made by combining varying fractions of the synthetic fly ash glasses over a range of 10% weight difference.

The microstructure and reactivities of the simulated fly ashes in cement paste at a 20% replacement factor were analyzed using an array of analytical techniques including low-temperature differential scanning calorimetry, isothermal calorimetry, SEM/EDX with multispectral image analysis, thermogravimetric analysis, electron microprobe analysis and compressive strength tests.

The simulated fly ash with the highest contents of Si, Al and Ca appears to be the most reactive across the various reactivity measurements, indicating the significance of these phases in the pozzolanic reaction of fly ash with cement. The reactivities of the individual synthetic glasses were similar within the bounds of experimental error. This could be due the smaller variations in the glass compositions as well as the 20% replacement factor.

INVESTIGATION OF THE EFFECT OF FLY ASH VARIABILITY ON CEMENT PASTE MICROSTRUCTURE AND MECHANICAL PROPERTIES USING SIMULATED FLY ASH

by

Samuel Amuasi Essien

Dissertation submitted to the Faculty of the Graduate School of the
University of Maryland, College Park, in partial fulfillment
of the requirements for the degree of
Doctor of Philosophy
2021

Advisory Committee:
Professor Amde M. Amde, Chair
Professor Mohamed S. Aggour
Professor Chung C. Fu
Professor Mohamad Al-Sheikhly
Professor Sung W. Lee

Acknowledgements

I am very grateful to my advisor, Prof. Amde Amde for his support and guidance throughout the entire research.

I am very thankful to Prof. Richard Livingston of the Materials Science Department, UMD for his immeasurable guidance and contributions to this research, and Dr. Walairat Bumrongjaroen for her assistance and contributions to this research.

Special thanks to Carol Grissom and Janet Douglas of the Smithsonian Institution's Museum Conservation Institute in Suitland, MD; Dr Jussara Tanesi of Turner-Fairbank Highway Research Center, McLean, VA; Dale Bentz and Dr Andrew Allen of NIST, Stuart Sherman of the National Ready Mixed Concrete Association in Greenbelt, MD; and Catholic University of America, Washington DC for their assistance with laboratory facilities.

I am very thankful to my family and friends for their support and encouragement throughout my research.

Financial support for this research was provided through the National Science Foundation.

Table of Contents

List of Tables

List of Figures

List of Abbreviations

ASEM	Automated Scanning Electron Microscopy
ASTM	American Society for Testing Materials
BSE	Backscattered Electrons
CCSEM	Computer-Controlled Scanning Electron Microscopy
C-S-H	Calcium Silicate Hydrate
DTG	Derivative Thermogravimetry
DSC	Differential Scanning Calorimetry
LT-DSC	Low-temperature Differential Scanning Calorimetry
EDS	Energy Dispersive Spectroscopy
EMPA	Electron Microprobe Analysis
SANS	Small Angle Neutron Scattering
SCM	Supplementary Cementitious Materials
SEM	Scanning Electron Microscopy
TG	Thermogravimetry
TGA	Thermogravimetric Analysis
XRD	X-ray Diffraction
XRF	X-ray Fluorescence Spectroscopy
w/c	Water to Cement Ratio

Chapter 1: Introduction

1.1 Statement of Objective

Fly ash is a by-product of coal combustion in coal-fired electric power plants. It is composed of fine particles resulting from the fusion of clay particles and other mineral impurities in the coal during the combustion process. Fly ash can be used as a partial replacement for Portland cement in concrete. As much as 80-90% of fly ash is composed of aluminosilicate glass. The amount and chemical composition of the fly ash glass strongly affects the reactivity of the fly ash. The chemical composition of fly ash glass is highly variable and depends on the chemical composition on the source coal. However, the current ASTM specification for fly ash, which is the industry standard, is based on the bulk chemical composition of the fly ash (ASTM C618-15 2015). This does not account for the inherent variability in the chemical composition of the reactive glass and the amount of glass, leading to sub-optimal utilization of fly ash in concrete.

The main objective of the current research is study of the effect of variation of the fly ash glass composition on various properties of fly ash cement pastes using synthetic fly ash glasses made from various clusters of glasses identified in a real fly ash as part of efforts to develop performance specifications based on standard fly ash glass compositions.

1.2 Background

1.2.1 Fly Ash Fundamentals

Concrete is the second most used material on earth by volume, only surpassed by water. The cement and concrete industry is responsible for about 5% of global anthropogenic CO_2 emissions (Worrell et al. 2001), and the largest source of CO_2 emissions from carbonate decompositions (Andrew 2018). The replacement of Portland cement with fly ash and other supplementary cementitious materials to produce more sustainable concrete and has gained widespread industry acceptance.

Fly ash is a by-product of coal combustion in coal-fired electric power plants. Coal is first pulverized in grinding mills before being blown with air into a furnace and ignited at temperatures reaching 1500^{o}C. At this temperature, most of the incombustible inorganic mineral components associated with the coal such as quartz, calcite, gypsum, feldspar and clay minerals melt to form small fused droplets and float out of the combustion chamber along with exhaust gases (Thomas 2013). These droplets are quickly cooled, forming small spherical glassy particles. A dust-collection mechanism removes the fly ash as a fine particulate residue from the combustion gases before they are discharged into the atmosphere.

In 2019, 29 million tons of pulverized coal combustion fly ash, or coal fly ash, was produced in the United States (Figure 1.1), of which approximately 60% was beneficially utilized (American Coal Ash Association 2020). The single largest beneficial utilization of fly ash is in the production of portland cement concrete (PCC) and concrete products (both as a partial cement replacement and as a

constituent in blended cements), which accounts for approximately 85% of the total fly ash beneficial use.

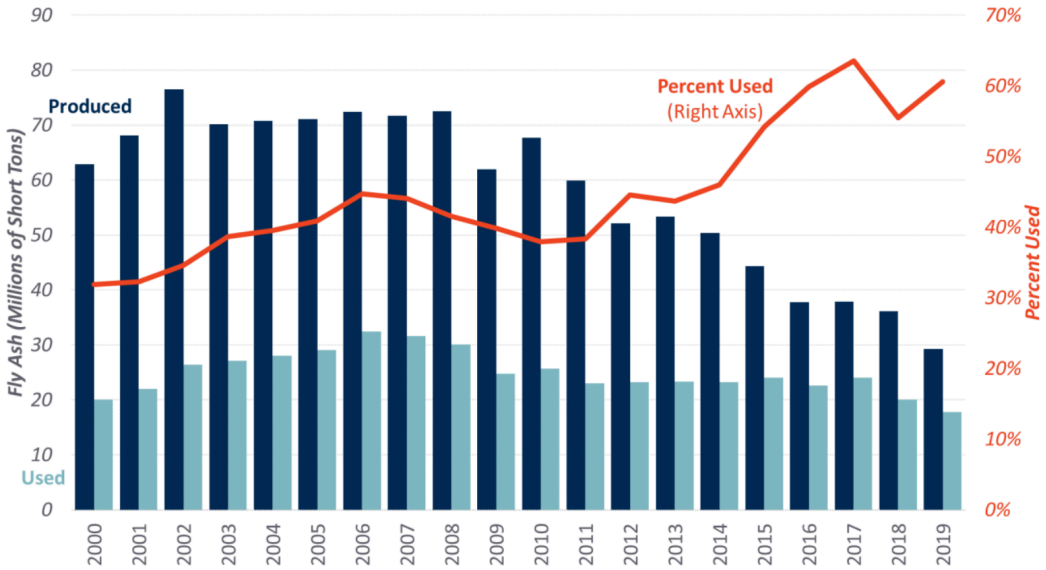

Figure 1.1 Fly ash production and use in the United States (American Coal Ash Association 2020)

Fly ash has many beneficial uses in concrete. It can improve the durability of concrete by moderating early-age cracking, inhibiting alkali-silica reaction, and reducing permeability for chloride transport. However, the use of fly ash at high replacement levels can retard cement hydration, delay setting, and reduce the rate of early-age strength development. The utilization of fly ash in concrete is hindered by inadequate characterization, leading to less predictable performance in concrete.

1.2.2 Fly Ash Classification

ASTM C618 classifies fly ash as Class C and Class F based on the source origin of the coal and bulk chemical composition of the fly ash. The chemical characterization is based on bulk oxide content usually obtained by x-ray

fluorescence (XRF) analysis. In terms of the bulk chemical composition, the sum of SiO_2, Al_2O_3, and Fe_2O_3 must be at least 70% by mass to be classified as Class F fly ash; while the sum must exceed 50% to be classified as Class C fly ash. Both classes must contain SO_3 content not exceeding 5%. This classification does not address the nature of reactivity and their inherent variability of the fly ash particles. It is used only as a quality-control or quality-assurance tool.

Class F, also known as low-calcium fly ashes, are low in CaO (less than 8%). They are normally produced from burning anthracite or bituminous coal. They are mostly composed of aluminosilicate glasses (60 to 90%) and varying amounts of crystalline quartz, mullite, hematite, and magnetite (ACI 232 2003). These crystalline phases are inert in concrete. In low-calcium fly ash, the glass requires an alkali source or lime to react and form cementitious material hydrates. These fly ashes are termed pozzolanic and have no significant self-cementing or hydraulic behavior.

Class C (high-calcium) fly ashes generally contain more than 20% CaO and are therefore termed high-calcium fly ash. Because of the high CaO content, the sum of SiO_2, Al_2O_3 and Fe_2O_3 can be significantly less than the 70% Class F minimum limit. High-calcium fly ashes are produced from lignite or subbituminous coals and consist of calcium-aluminosilicate glass, and a wide variety of crystalline phases such as anhydrite ($CaSO_4$), tricalcium aluminate (C_3A), lime (CaO), periclase, melitite, merwinite, in addition to the ones found in low-calcium fly ash (ACI 232 2003). The reactive calcium bearing glass makes these fly ashes react more readily, thus they are both pozzolanic and hydraulic in nature. Fly ash with intermediate calcium contents (8 to 20%) falls between low-calcium and high-calcium fly ashes in terms of

composition and reactivity. The calcium content is arguably the biggest contributor to the performance of fly ash in concrete (Thomas et al, 1999), although the alkalis, carbon, and sulfate can affect its performance in concrete.

1.3 Research Approach

Fly ash reactivity in concrete has been studied extensively by many researchers. The conventional engineering approach to the investigation of fly as reactivity is based on the measurement of the macroscopic properties of strength (Helmuth 1987). These studies are based on natural (real) fly ashes obtained from power plants. A major innovation in this study is the use of simulated fly ashes instead of real fly ashes. This is due to the practical difficulties associated with using raw fly ash in controlled experiments due to the heterogeneity in chemical composition and physical properties. Among the advantages of simulated fly ash is its controllable and homogeneous chemical composition. Simulated fly ash glass samples have been used successfully in the past to study the reactivity of fly ashes (Locher 1960; Watt and Thorne 1966). This research goes beyond previous work by simulating the complete fly ash, not just individual glassy phases, by adding several compositions of simulated glass in the correct proportions to match the bulk chemical composition of the real fly ash (Bumrongjaroen et al. 2007).

This study investigates the hydration of simulated fly ashes and its glass modelled after a real Class F fly ash. To study the effect of glass proportion on the reactivity of fly ash, a 10 wt.% difference in glass was used. This range is the maximum percentage that can be varied while the composition of the fly ash is still classified as Class F. The approach used here is a combination of test methods

operating at different length scales. The reactivity of the complete simulated fly ash and the synthetic fly ash glasses was measured in cement pastes using isothermal calorimetry, thermogravimetry (TGA), and SEM/EDS with multispectral image analysis. The microstructure development was observed by thermoporosimetry and SEM/EDS. At the largest scale, the development of compressive strength was measured with standard engineering tests on the mortar cubes.

1.4 Organization of Dissertation

This dissertation is divided into six chapters, including this Introduction. A literature of review of cement and fly ash is presented in Chapter 2. Chapter 3 presents the preparation of the synthetic and simulated fly ashes. Chapter 4 presents the various experimental methods used in this study. The analysis and discussions of results is presented in Chapter 5. Chapter 6 presents a summary of the research findings and recommendations for future work.

Chapter 2: Literature Review

2.1 Portland Cement

Portland cement is a hydraulic cement composed primarily of calcium silicates. It is made by burning a mix of calcium carbonate (limestone or chalk) and an aluminosilicate (clay or shale) to a temperature of about 1450°C to produce clinker nodules. The clinker is then ground with about 5% gypsum (calcium sulfate) to produce cement. The calcium sulfate (gypsum) controls the rate of set (hardening) of the cement. (Bye 1999; Taylor 1997). The following abbreviations are commonly used in cement chemistry:

Table 2.1 Abbreviations used in cement chemistry

Abbreviation	**Formula**
S	SiO_2
A	Al_2O_3
C	CaO
F	Fe_2O_3
M	MgO
N	Na_2O
K	K_2O
S^-	SO_3
C^-	CO_2
H	H_2O

Clinker has a composition of approximately 67% CaO, 22% SiO_2, 5% Al_2O_3, 3% Fe_2O_3, and 3% other components, and normally contains four major phases: alite, belite, aluminate and ferrite, written as C_3S, C_2S, C_3A and C_4AF respectively in cement notation (Taylor 1997). Portland cement is hydraulic, meaning it sets and hardens when mixed with water. Hardening results from reactions between the major phases and water.

2.1.1 Composition of Portland Cement

The four major constituents C_3S, C_2S, C_3A, and C_4AF make up about 90-95% of Portland cement, with the remainder consisting of calcium sulfate, alkali sulfates, unreacted (free) lime, MgO and other minor constituents.

Alite (C_3S) is tricalcium silicate (Ca_3SiO_5) modified by ionic substitutions such as Al^{3+}, Fe^{3+}, and Mg^{2+} with smaller amounts of K^+, Na^+ and SO_3 (Bye 1999). It constitutes about 50-70% of Portland cement clinkers and is the most important constituent for strength development. It reacts quickly with water and is mainly responsible for strength development during the first 28 days (Taylor 1997).

Belite (C_2S) is dicalcium silicate (Ca_2SiO_4) modified by ionic substitutions. The β polymorph is the most common in Portland cement. Belite constitutes about 15-30% of Portland cement clinkers. It reacts slowly with water, thus contributing little to strength development in the first 28 days, but substantially to strength at later ages (Taylor 1997).

Aluminate (C_3A), which is tricalcium aluminate ($Ca_3Al_2O_6$) substantially modified in composition and structure by ionic substitutions, constitutes about 5-10% of Portland cement clinker. It reacts rapidly with water and is responsible for most of

the heat of hydration generated during the first hour of hydration. This rapid reaction can cause rapid setting. Rapid setting is controlled by the addition of gypsum.

Ferrite (C_4AF) is tetra-calcium aluminoferrite (Ca_2AlFeO_5) that has undergone substantial modification through variable Al/Fe ratio and ionic substitutions. It constitutes about 5-15% of normal Portland cement clinkers. It's rate of reaction is highly variable, but appears to higher initially and very low at later ages (Taylor 1997).

2.2 Hydration of Portland Cement

Cement hydration is a very complex process, involving a series of complex chemical reactions and processes that begin as soon as water comes into contact with the cement. The hydration of Portland cement involves a collection of coupled chemical processes which may operate in series, parallel, or in some form of complex combination, with the rate of occurrence of each process determined both by the nature of the process and by the state of the system at that instant (Bullard et al. 2011). These processes can be categorized as follows (Bullard et al. 2011):

- Dissolution/dissociation, which involves the detachment of molecular units from the surface of the cement grains in contact with water.
- Diffusion, which describes the transport of solution components through the pore volume of cement paste or along the surfaces of solids in the adsorption layer.
- Growth, which involves surface attachment or incorporation of molecular units into the surface of a crystalline or amorphous solid within its self-adsorption layer.

- Nucleation, which is the heterogeneous or heterogenous initiation of solid precipitates in solution.
- Complexation, which is reactions between simple ions to form ion complexes or adsorbed molecular complexes on solid surfaces.
- Adsorption, which is the accumulation of ions or other molecular units at interface such as the surface of a solid particle in a liquid.

For instance, a simple crystal growth from solution involves diffusion of solute to the proximity of an existing solid surface, adsorption of the solute onto the surface, complexation of several solute species into a molecular unit that can be incorporated into the crystal structure and, finally, attachment and equilibration of that molecular unit into the structure (Bullard et al. 2011; Lasaga 1981; Morel 1983).

In simple terms, the hydration of Portland cement proceeds through a dissolution-precipitation process, where the cement releases ions into the mix water (pore solution) by means of dissolution to a point where higher ionic concentrations results in precipitation of hydration products. This process is exothermic and releases a heat of hydration. The main products of cement hydration are C-S-H (a poorly crystalline and nearly amorphous calcium silicate hydrate with no fixed stoichiometry), portlandite (CH, a crystalline calcium hydroxide phase), and various calcium aluminate hydrates.

2.2.1 Mechanism of C_3S Hydration

C_3S or alite (its impure form) constitutes between 50 to 80% of Portland cement and thus dominates the hydration and strength development of Portland cement. Therefore, many studies have concentrated on the hydration of this phase.

The main products of C_3S hydration are C-S-H (a poorly crystalline and nearly amorphous calcium silicate hydrate with no fixed stoichiometry) and portlandite (CH, a crystalline calcium hydroxide phase). About 70% of C_3S reacts in the first 28 days and virtually all in one year (Taylor 1997). The reaction of C_3S proceeds as follows:

$$2C_3S + 6H \rightarrow C_3S_2H_3 + 3CH^1 \qquad 2.1$$

The hydration of C_3S is responsible for the strength gain in Portland cement. There are four main arbitrary stages with the hydration of C_3S as shown in Figure 2.1. The initial reaction, the induction or period of slow reaction, the acceleration period, and the deceleration period. After these four main periods, there is a period of slow ongoing hydration.

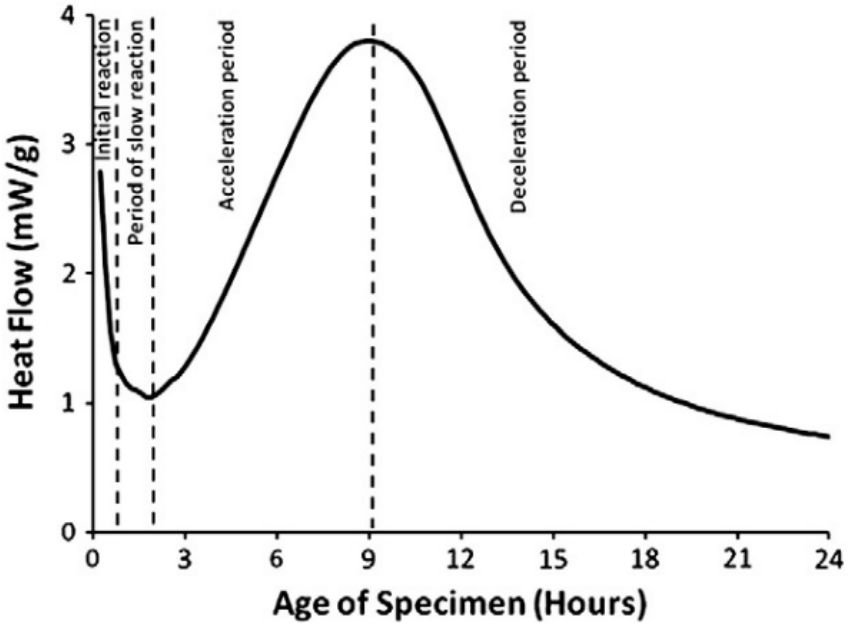

Figure 2.1 Rate of alite hydration by isothermal calorimetry (Bullard et al. 2011)

[1] Written in cement notation (see Table 2.1)

The initial reactions between C_3S and water begins immediately upon wetting. It is very rapid, highly exothermic, and is characterized by a large exothermic signal in isothermal calorimetry experiments. During this period, there is rapid and congruent dissolution of C_3S, which releases calcium and silicate ions into solution according to reaction below (Bullard et al. 2011).

$$C_3S + 3H_2O \rightarrow 3Ca^{2+} + H_2SO_4^{2-} + 3OH^- \quad 2.2$$

The main products of C_3S hydrations are C-S-H and CH. Due to the congruent nature of the dissolution, the rate depends on the specific surface area of the C_3S and the availability of active dissolution sites (Gartner et al. 2002). The dissolution rate of C_3S decelerates very rapidly while the solution is still undersaturated (Garrault and Nonat 2001). There is considerable debate as to what causes the slowdown in the dissolution rate of C_3S at this stage, with many hypotheses proposed over the years to offer an explanation. Bullard et al identify two main mechanisms that continue to offer to most plausible explanations in light of recent experimental and theoretical research. These are the mestastable barrier hypothesis and the slow dissolution step hypothesis.

The metastable barrier hypothesis states that the initial fast reaction is terminated when the mean concentrations of calcium and silica in solution reach a critical solubility product, leading to nucleation and precipitation of an initial product (Gartner et al. 2002). This initial product, a continuous but thin metastable layer of calcium silicate hydrate, effectively passivates the surface of the C_3S particles by restricting its access to water and/or restricts diffusion of detaching ions away from the surface (Bullard et al. 2011; Stein and Stevels 1964). The surface of the C_3S

becomes coated with this thin metastable layer as the C_3S serves as nucleation sites for the precipitation of the hydration products. This inhibits further dissolution of the C_3S and leads to a slowdown in the reaction. The protective coating that terminates the initial rapid dissolution of C_3S is a type of C-S-H that is probably somewhat different from the C-S-H that forms at later ages (Gartner et al. 2002).

The slow dissolution step hypothesis is based on a steady state balance between the slow dissolution of C_3S and the initial slow growth of C-S-H. When C_3S comes into contact with water, a superficially hydroxylated layer forms on the C_3S surfaces, and dissociation of ions from this layer occurs more slowly than would be otherwise expected for a mineral in highly undersaturated solutions (Barret et al. 1983; Barret and Ménétrier 1980). The apparent solubility of this superficially hydroxylated layer is much lower than that of C_3S and the dissolution rate decreases very rapidly when the calcium hydroxide concentration in solution increases. C-S-H nucleates very rapidly on the C_3S surfaces and begins to grow slowly when the solution exceeds a maximum supersaturation with respect to C-S-H (Bullard et al. 2011; Garrault-Gauffinet and Nonat 1999; Garrault and Nonat 2001). The nucleation and growth of C-S-H causes the silicate ion concertation in solution to decrease and the Ca:Si ratio in solution to increase, which leads to a steady state condition in which the solution is supersaturated with respect to C-S-H but undersaturated with respect to C_3S.

The induction period (or period of slow reaction) is a consequence of the slow down in the initial reaction. According to the metastable barrier hypothesis, the surface of the C_3S becomes coated with this thin metastable layer as the C_3S serves as

nucleation sites for the precipitation of the hydration products. This inhibits further dissolution of the C_3S and leads to a slowdown in the reaction. The protective coating that terminates the initial rapid dissolution of C_3S is a type of C-S-H that is probably somewhat different from the C-S-H that forms at later ages (Gartner et al. 2002).

In pure C_3S systems, a true and distinct induction period between the initial reaction and the accelerated period of growth of hydration exists only when chemical retarders have been added. The slow down in reaction is a result of the mechanisms of the initial reactions until a critical point is reached when the rate of nucleation and growth starts to accelerate.

The acceleration period is a period of renewed hydration that begins about an hour after wetting and is responsible for the main heat evolution peak. It is a high order growth period that results in the rapid growth of C-S-H and CH and associated increase in heat production. The acceleration period is based on a nucleation and growth mechanism. There is still considerable debate about what triggers this increase in the rate of reaction. Some of the proposed theories includes the nucleation and growth of C-S-H, in which the nucleation and growth of a stable C-S-H happens during the slow reaction period and becomes rate controlling during the acceleration period as they form a metastable protective layer of hydrates that become chemically unstable and expose the high-solubility C_3S for renewed hydration. Another theory is the exponential growth of stable C-S-H nuclei that forms during the initial reaction that makes C-S-H growth rate controlling. The third theory is the rupture in the initial metastable C-S-H barrier that exposes the underlying C-S-H particles to renewed reaction. The fourth theory is the nucleation and growth of CH that becomes rate

controlling and indirectly controls the growth of C-S-H (Bullard et al. 2011; Gartner et al. 2002).

The rate determining mechanism in this period has long been attributed to the growth of C-S-H (Scrivener et al. 2015a). There is a growing body of evidence that indicates the rate-controlling step of hydration during the acceleration period is related to the heterogeneous nucleation and growth of C-S-H on C_3S surfaces when C-S-H is observed by scanning, atomic force, or transmission electron microscopy. (Bullard et al. 2011; Garrault et al. 2005; Gartner et al. 2002; Thomas et al. 2009). The rate of C_3S hydration is proportional to the surface area of C-S-H, as the C-S-H serves as active growth sites for further nucleation and growth of C-S-H (Thomas et al. 2011).

The deceleration period is the period of slow reaction that comes after the acceleration period. The rate of hydration at later ages is controlled by a diffusion process due to the precipitation of hydration products around the C_3S particles. The rate of hydration slows down, with associated drop in heat released. By this period, small particles (below 7μm) have been consumed by reaction, leaving only large particles that react at a slower rate. The filling of the capillary pore space with hydration products leads to a decrease in the rate of reaction. Chemical shrinkage from lack of water leads to the formation of gas-filled porosity after setting, which decreases the internal relative humidity and rate of hydration. After several days, space becomes the major factor controlling hydration.

It has long been held that diffusion is the rate controlling mechanism during the deceleration period and the cause of the onset of the deceleration period. As C-S-

H continues to grow around the C_3S particles, it builds up a layer of around 1um thickness. When this layer reaches a certain thickness, the reaction slows down due to the time needed for diffusion through the layer. It is also possible that the hydration layer creates a concentration gradient and decreases the undersaturation adjacent to the C_3S particles, which slows down the reaction (Scrivener and Nonat 2011). However, recent evidence shows that it is the filling of space with hydration products and consequent reduction in the surface area of the hydrating particles that is responsible for the decrease in the rate of hydration (Gallucci et al. 2010; Scrivener and Nonat 2011). A consequence of nucleation and growth of a phase in a finite volume is the impingement of growing regions that leads to a decrease in the free surface area of reactive phases available for nucleation and growth. As the rate of reaction is proportional to the surface of area of the growing phase, this leads to a decrease in the rate of reaction (Scrivener and Nonat 2011). CH crystals continue to grow larger, filling up large water-filled voids and can totally engulf zones of C-S-H and some of the hydrating C_3S grains, thereby limiting their potential for complete hydration (Gartner et al. 2002).

C_3S and C_2S produce the same hydration products of C-S-H and CH, but C2S produces much less hydration products and reacts slower than C_3S. The hydration reaction of C_2S is represented as:

$$2C_2S + 4H \rightarrow C_3S_2H_3 + CH \qquad 2.3$$

C_2S hydration becomes significant only after about 10 days (Scrivener et al. 2015a).

2.2.2 Hydration of C_3A

C_3A is the most reactive clinker phase in Portland cement. It has significant influence on the early hydration and rheology of Portland cement and concrete. C_3A reacts with water to produce hydrates with the form of crystallized hexagonal plates with compositions C_2AH_8 and C_4AH_{19} (AFm phases). These hexagonal hydrates are metastable and are converted to stable forms of cubic C_3AH_6 (hydrogarnet) according to the reaction below (Gartner et al. 2002):

$$2C_3A + 27H \rightarrow C_4AH_{19} + C_2AH_8 \rightarrow 2C_3AH_6 \quad 2.4$$

This transformation begins within 25 mins near room temperature (Corstanje et al. 1974). The formation of the hexagonal hydrates is accompanied by high heat evolution which raises the temperature of the hydrating system and can accelerate the conversion to stable C_3AH_6. It can also lead to rapid setting of the concrete (flash set). Once C_3AH_6 has nucleated, it provides nucleation sites for the crystallization of more C_4AH_{19} and C_2AH_8, and the conversion process continues.

To control rapid setting, a source of calcium sulfate, usually in the form of gypsum ($CaSO_4.2H_2O$), is added to Portland cement. When gypsum is present, C_3A undergoes a different reaction to produce ettringite:

$$C_3A + 3C\bar{S}H_2 + 26H \rightarrow C_6A\bar{S}_3H_{32} \quad 2.5$$

Ettringite is the first stable hydration product formed in the initial period of rapid reaction and will continue to form as long as sulfate ions are available for reaction. This initial period of reaction is very rapid, after which the rate decreases within a few minutes and gives way to a period of slow reaction and low heat output. The length of the slow period of reaction depends on the quantity of calcium sulfate

(gypsum) available for reaction. When gypsum reacts completely before C_3A, this leads to a drastic reduction in the concentration of sulfate ions in pore solution. This makes ettringite unstable, leading to a conversion of ettringite to tetracalcium monosulfoaluminate hydrate (monosulfoaluminate), an AFm phase with less sulfate, according to the reaction:

$$2C_3A + C_6A\bar{S}_3H_{32} + 4H \rightarrow 3C_4A\bar{S}H_{12} \qquad 2.6$$

The rate of reaction increases rapidly again as a result of the conversion of ettringite to calcium monosulfoaluminate. This reaction happens within the first one or two days of hydration. As most cements do not contain enough gypsum to react with all the C_3A, almost all the ettringite is converted to monosulphoaluminate. There is considerable debate surrounding the reason for the slowdown in the initial reaction. It has long been held that gypsum forms a continuous coating on the surface of the reacting C_3A, which impedes the diffusion of SO_4^{2-}, OH^- and Ca^{2+} ions, which slows down the reaction (prevents flash set), resulting in an induction period, and that the kinetics of ettringite formation is diffusion controlled, so the more gypsum there is in the system, the longer the induction period (Gartner et al. 2002). When the SO_4^{2-} and Ca^{2+} ions in hydrating solution are depleted, the protective coating is disrupted, which results in the renewed hydration of C_3A to form AFm phases. However, a recent review by (Bullard et al. 2011) concluded that the early slowdown in C_3A reaction in the presence of gypsum is likely due to the absorption of sulfate ions on reactive dissolution sites on the surface of C_3A as suggested by (Minard et al. 2007).

C_4AF reacts in a similar way to C_3A, though more slowly. Some of the aluminum in the reactions products is substituted for iron.

$$C_4AF + 3C\bar{S}H_2 + 21H \rightarrow C_6(A,F)\bar{S}_3H_{32} + (F,A)H_3 \quad 2.7$$

$$C_4AF + C_6(A,F)\bar{S}_3H_{32} + 7H \rightarrow 3C_4(A,F)\bar{S}H_{12} + (F,A)H_3 \quad 2.8$$

where (A,F) indicates aluminum with variable substitution of iron, and (F,A) indicates iron substitution of aluminum. Because of the substituted iron, the main reaction products are not pure ettringite and monosulfoaluminate, though they have the same crystal structure. Therefore, they are denoted as AFt and AFm respectively, where m indicates monosulfate (one sulfate ion) and t indicates trisulfate (three sulfate ions). In portland cement, C_3A and C_4AF are intimately mixed together, so the aluminum bearing reaction products are denoted AFm and AFt.

2.2.3 Hydration of Portland Cement

The hydration of Portland cement is similar to that of the individual clinker phases though more complex. The dissolution of anhydrous phases leads to the precipitation of much less soluble products, typically colloidal and micro-crystalline hydrates that form the hardened paste (Gartner et al. 2002). The hydration mechanism is dominated by C_3S and C_3A. The hydration of Portland cement is an exothermic process that produces heat. This heat of hydration can be followed by isothermal calorimetry. The hydration reactions proceed until either a lack of reactants (cement components and water) or a lack of space to deposit the hydration products causes the reactions to cease. There is considerable debate in the literature about the exact mechanisms, stages, and durations of the kinetics of hydration. However, there is general consensus that the hydration kinetics can be divided into about four arbitrary stages: initial reaction, dormant or induction period, acceleration period, and deceleration period.

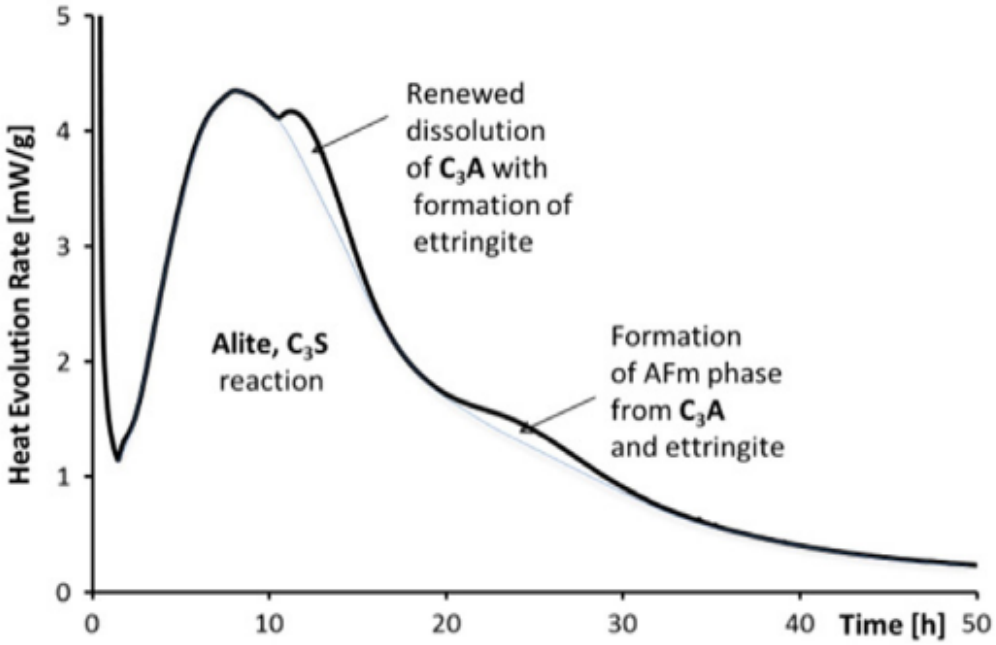

Figure 2.2 Rate of Portland cement hydration by isothermal calorimetry (Scrivener et al. 2015a)

As soon as cement touches water, a series of rapid reactions involving the clinker interstitial phases (i.e. the aluminates, aluminoferrites, alkali sulphates and free lime) and calcium sulphates (gypsum, hemihydrate, and/or anhydrite) begins. C_3A is mainly responsible for the heat released at this stage as it dissolves very fast. The aluminate phases react very rapidly, releasing calcium and aluminate ions into the pore solution. This reaction is exothermic. The aluminate ions in solution precipitate to form ettringite or AFt, an aluminate hydrate layer, on the surface of the cement particles. The ettringite (AFt) phase contains a lot of sulphate, which is readily available from the soluble alkali sulphates and gypsum. The free lime in

clinker also dissolves rapidly and exothermically at this state, and in sufficient quantities can lead to supersaturation of portlandite.

During stage 1, there is rapid formation of an amorphous layer of hydration products around the cement particles, which inhibits access to pore solution and thus prevents further rapid dissolution.

The first peak (initial period) denotes the period of rapid heat evolution due to the rapid reactions between cement and water as soon as they come into contact, which leads to the rapid dissolution of ionic species into the liquid phase. The alkali sulfates in the cement dissolve very quickly, releasing Ca^{2+}, Na^{+} and SO_4^{2-} ions. Evidence from chemical analyses of the solution phases have shown that C_3S dissolves congruently and rapidly in the first seconds after wetting (Bullard et al. 2011) as a layer of C-S-H precipitates at the surface of the cement particle (Odler 1998). C_3S hydration in this phase increases the Ca^{2+} and OH^{-} concentration in the liquid. C_3A and the ferrite phases also dissolve and react with Ca^{2+} and SO_4^{2-} ions to produce ettringite (AFt). Because of its slow reaction rate, only a minute fraction of C_2S reacts during this initial period. The duration of this phase is very short, about 15 minutes. These fast early hydration reactions deposit a layer of hydration products on the surface of the cement particles, which slows down the hydration, leading to a dormant or induction period. During this induction period, the heat liberation rate is very low. This period of inactivity is due to the time required for the ions in solution to reach a critical concentration before nucleation occurs in order for hydration to continue. This period lasts for about 2 to 4 hours, and it is during this time that setting begins, and the time limit at which placing of concrete occurs.

The dormant period is followed by the acceleration period (second peak), where the progress of hydration accelerates again. This period is dominated by C_3S hydration, leading to the formation of more C-S-H. Portlandite also precipitates from the liquid phase, resulting in a gradual decrease in the Ca^{2+} in the liquid phase. Complete dissolution of calcium sulfate in the cement occurs during the period, leading to a decline in the concentration of SO_4^{2-} in the liquid phase due to the formation of AFt as well as adsorption of SO_4^{2-} into the surface of the C-S-H. This phase is controlled by nucleation and growth of hydration products (Odler 1998).

At stage 3, the rate of reaction increases drastically, reaching a maximum within 24 hours after initial mixing. C_3S hydration is mostly responsible for this stage. The rate of hydration at this stage is controlled by nucleation and growth. During this stage, there is continuous and rapid deposition of hydration products (mainly C-S-H gel and CH) into the capillary porosity (the space originally occupied by the mix water). This process causes a large decrease in the total pore volume and a resulting increase in the strength of the paste. The microstructure of the cement paste at this stage consists of unreacted cores of cement particles surrounded by a continuous layer of hydration products. This continuous layer of hydration products has very fine internal porosity filled with pore solution, and larger capillary pores. For further hydration to occur, dissolved ions from the cement must diffuse outward and precipitate into the capillary pores, or water must diffuse inward to the unreacted cement cores.

At stage 4, diffusion of ions from the cement outward into the capillary pores occurs at a much slower rate, and so is water diffusing inward into the unreacted

cement cores due to formation of thicker hydration products around the cement particles.

2.3 Fly Ash

2.3.1 Physical Properties

The physical and chemical properties of fly ash vary widely and depend on the type and mineralogical composition of the source coal, the degree of coal pulverization, the type of furnace and emission control devices, and the manner in which the fly ash is collected and handled (Siddique and Khan 2011). Therefore, fly ashes are very heterogeneous in nature.

Most fly ash particles can be classified into two groups: plerospheres, which are hollow spheres packed with smaller spheres and cenospheres, which are hollow and empty spheres. They may also include irregular or angular particles, which include both unburned coal and mineral particles (Helmuth 1987).

Fly ash particle sizes vary greatly depending on the coal source. Most fly ash particles range from less than 1μm to over 100 μm. The median particle size is generally from in the range of 5μm to 20μm (Thomas 2013). In general, a large fraction of fly ash particles is less than 3μm in diameter. The fineness and spherical shape of fly ash particles improves the fluidity and workability of fresh concrete and contributes to the reactivity of the fly ash.

There are wide variations in particle densities. This is as a result of the presence of bubbles in glassy particles and voids in the agglomerated particles (Helmuth 1987). The bulk density of fly ash depends on the degree of compaction of

the powdered material. Typical values are in the range of 500 to 1500 kg/m^3. The specific gravity ranges from 1.9 to 2.8. The unique spherical morphologies of fly ash particles create a large range in specific gravity for fly ashes. This value is dependent on the chemical composition of the fly ash, especially the carbon and iron content. It has also been shown that the specific gravity increases with calcium content due to the formation of a denser glass (McCarthy et al. 1989). The specific surface area is generally in the range of 300 to 500m^2/kg (Thomas 2013).

2.3.2 Chemical Composition

Fly ash is made up of mainly aluminosilicate or calcium-aluminosilicate glass (about 75-90 weight%) as well as varying amounts of residues of crystalline phases such quartz, hematite, magnetite, mullite, and magnetite. The major elements in fly ash are O, Si, Al, Ca, and Fe, along with lesser amounts of Mg, S, and C. These elements are found in fly ash because of their lower volatility and the short period of time the particles actually remain in the furnace during combustion (Helmuth 1987). The composition of the glass is highly variable and depends on the rate of cooling and on the amount of substitution or modification by other ions such as Fe, Ca, Na, K, and Mg. Although the constituents of fly ash are not normally present as oxides, the chemical composition of fly ash is reported in oxides. The ternary diagram shown in Figure 2.3 shows the CaO, SiO_2 and Al_2O_3 contents in Portland cement and other cementitious materials.

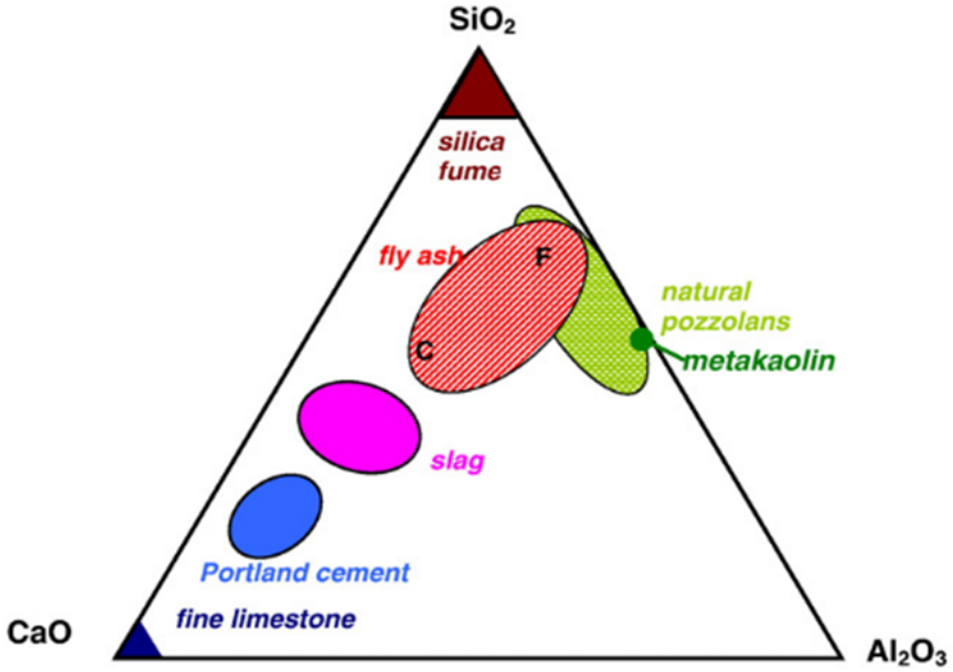

Figure 2.3 Ternary diagram of cementitious materials (Lothenbach et al. 2011)

Fly ash is a heterogeneous material at the micrometer and even the nanometer scale (Hemmings et al. 1986). The chemical composition and mineral assemblage in a given fly ash is characteristic of the coal source from which it is derived. The amounts of the four principal constituents (SiO_2, Al_2O_3, CaO, and Fe_2O_3) vary widely. Bulk chemical analysis shows that SiO_2 (35% to 60%), Al_2O_3 (10 to 30%), CaO (1% to 35%), and Fe_2O_3 (4% to 20%) are the major constituents (ACI 232 2003).

Other phases that may be present include MgO, Na_2O, K_2O, SO_3, MnO, TiO_2 and unburned carbon. Both crystalline and non-crystalline phases form on the surface of the fly ash particles when the elements react with oxygen in the flue gases, and condensation and crystallization occur within the melt droplets. The chemical composition of fly ash depends largely on the mineral composition of the coal from

which the fly ash was obtained, that is, the inorganic part of the coal (Massazza 1998). In general, low calcium fly ashes (<8% CaO) are obtained from bituminous coal and are predominantly made of aluminosilicate glasses and inert crystalline phases. High-calcium fly ashes (>20% CaO) are obtained from sub-bituminous coal and are made up of calcium-aluminosilicate glass and crystalline phases that may be reactive.

2.3.3 Crystalline Phases in Fly Ash

Fly ash consists of crystalline and amorphous (glassy) phases. Crystalline solids are solid materials whose constituent atoms or molecules exhibit long range order, that is, a regular and periodic repetition of atoms or molecules in three-dimensional space (Pecharsky and Zavalij 2009). This repeating pattern constitutes a crystal lattice. Due to rapid cooling of burned coal in power plants, fly ashes consist mainly of non-crystalline phases or glass (<=90%), and a small amount of crystalline phases. The mineralogy of the source coal influences the type of crystalline phases that occur in the fly ash. Fly ashes contain one or more of these four major crystalline phases: quartz (SiO_2), mullite ($Al_6Si_2O_{13}$), magnetite (Fe_3O_4), and hematite (Fe_2O_3). Other crystalline phases that may be present in fly ash include alite (C_3S), belite (C_2S), tricalcium aluminate (C_3A), lime, anhydrite, periclase, melitite and merwinite. There are fewer crystalline phases in Class F fly ash, whereas there can be many crystalline phases in Class C fly ashes as a result of more variable chemical composition. XRD analysis has shown evidence of the following phases crystalline phases in lignite fly ashes: quartz, lime (free), periclase, anhydrite, ferrite, spinel, mullite, hematite, alkali sulfates, and melilite. In Class C or subbituminous fly ashes,

the crystalline phases may include C_3A, C_4A, C_4AS (Massazza 1998; McCarthy et al. 1989).

The quartz in fly ash is a result of the impurities in the coal that failed to melt during the combustion process. Small amounts of volatilized Si may also oxidize to form very fine crystals of quartz with the fly ash glass (Diamond 1983). Quartz is the most intense peak in the XRD pattern of fly ash.

Mullite is found in substantial quantities only in low-calcium fly ashes. It is the principal aluminum bearing mineral in low-calcium bituminous fly ash and is normally not chemically reactive in concrete. Mullite is almost twice as abundant in low-calcium fly ash as compared to high-calcium fly ash, mainly due to differences in the Al content of the clay minerals associated with the source coal (McCarthy et al. 1984). Mullite forms within the glass spheres as they solidify around it.

The principal iron oxides in fly ash are magnetite and hematite, which are largely not reactive. Approximately one-third to half of the iron present in fly ash is in the form of magnetite or hematite (McCarthy et al. 1989). The rest of the iron in fly ash is contained in the glass phases (Helmuth 1987). Magnetite (Fe_3O_4), in its purest form, is the crystalline spinel structure closest to that found in fly ash (ACI 232 2003). Hematite (Fe_2O_3) is formed by the oxidation of magnetite.

High-calcium fly ashes contain several calcium-bearing minerals that are reactive. The most common is C_3A. The cementitious nature of C_3A contributes to the self-cementing properties of high-calcium fly ashes. C_3A is very reactive in the presence of calcium and sulfate ions in solution. Other Ca-bearing minerals present in high-calcium fly ashes include C_3S and C_2S.

2.3.4 Amorphous (Glass) Phases in Fly Ash

A material is amorphous (glass) when it has no long-range order, that is, when there is no regularity in the arrangement of its molecular constituents on a scale larger than a few times the size of these groups (Doremus 1994). When a crystalline solid (mineral) is heated to its melting point and changes into a liquid, the crystal lattice collapses and the lattice elements do not return to their bonded sites upon rapid cooling, leading to the formation of glass. Fly ash glass is amorphous aluminosilicate that is formed when the molten coal by-product is cooled rapidly, locking the elements into disordered, non-crystalline structure. Among the major oxides in fly ash (SiO_2, Al_2O_3, Fe_2O_3, and CaO), only SiO_2 is a glass former by itself (Diamond 1983). The siliceous glass can contain relatively large amounts of other oxides. The aluminosilicate glass found in fly ash consists of a random network of silica tetrahedra which may be linked to each other silica tetrahedra at their corners without periodicity (Doremus 1994). Aluminum and other cations such as Fe, B, and P may substitute for silicon within the silicon tetrahedra in the form of polymeric network former substitutions, while Ca, Na, K, Mg, Fe and various other cations can be incorporated as network modifier additions and occupy holes between the tetrahedra. These substitutions and modifications break the silica bonds in the tetrahedra, resulting in bridging and non-bridging oxygen atoms in the network. The negatively charged non-bridging oxygen atom creates a net negative charge that must be balanced by a cation. The disorder in the glass structure depends on network substitution and modification by the cations. These modifications affect free energy and reactivity of the fly ash glass (Hemmings and Berry 1987). The modifications of

the amorphous silicates and aluminosilicates originate from the co-melting with other oxides during the fly ash formation and the rate of cooling. Therefore, fly ash glass is highly heterogenous, with varying chemical composition within the same fly ash glass.

As much as 80-90% of fly ash is composed of aluminosilicate glass. The amount and chemical composition of the fly ash glass composition strongly affects the reactivity of the fly ash, since most of the crystalline phases are inert. Fly ash glass composition is highly variable. The composition and amount of glass in a particular fly ash depends on the origin and composition of the coal, as well as plant operating conditions such boiler temperature. The major differences in fly ash glass composition lie in the amount of calcium present in the glass, as well as the amount of substitution and modification by other ions in the glass such as Fe, Na, K, and Mg. Coal with only small amounts of calcium, such as anthracite and bituminous or some lignite coals, result in aluminosilicate fly ash glass (Class F). Sub-bituminous and some lignite coals leave larger amounts of calcium in the fly ash and result in calcium aluminosilicate fly ash glass (Class C) (Roy et al. 1984).

The presence of glassy and crystalline phases in fly ash is evidence in the location of crystalline peaks and broad ‘hump’ or diffuse bands in XRD patterns. The position of this hump depends on the composition of the glass, and it will be located near the main peak of the crystalline compound if the glass is devitrified (Diamond 1983).

2.3.5 Characterization of Fly Ash Chemical Composition

Fly ash chemical composition is typically characterized in terms of bulk XRF, which includes both glassy and crystalline phases. However, this does not make any distinction between the glassy and crystalline phases. The crystalline phases in fly ash have been well studied and characterized due to well established methods for studying crystalline phases by XRD. Advances in XRD techniques have made qualitative and quantitative characterization of fly ash crystalline phases feasible. Detailed qualitative XRD studies on fly ash have been carried out by (Diamond 1983; McCarthy et al. 1984, 1989; Winburn et al. 2000) and many others. However, apart from determining the total amount of amorphous phases, characterizing the chemical composition of the amorphous phases in fly ash has been very challenging because of difficulties in studying amorphous phases in XRD due to the absence of long-range molecular order in glass phases. This has hampered efforts to fully characterize fly ash in terms of isolating the more reactive glassy phases from the less reactive crystalline ones, and the variability within the glass phase itself. Bulk XRF characterization does not make that distinction. XRF data represents bulk averages over heterogeneous glass compositions, including crystalline phases. Therefore, indexes established based on this bulk characterization, such as ASTM C618, fail to take into consideration the complexity and variability of the glassy phases. There have been recent efforts to characterize the glassy phase using various SEM/EDS techniques. These techniques fall into two broad categories: point X-ray analysis, which calculates the elemental composition of a point in the fly ash image using standards-based or standardless algorithms, and X-ray mapping with EDS which

maps the location and relative amounts of individual elements in the fly ash. (Williams et al. 2005) used EDS spot analysis and image mapping to characterize the composition of fly ash glass. Composite images were made from Al, Si, and Ca compositional maps. The composite images were used to select regions for x-ray spot analysis for more detail quantification. The composite imaging combined with quantitative spot analysis suggested for types of particles within the fly ash based on chemical composition, indicating interparticle variances in chemical composition. A quantitative image analysis algorithm developed by (Bentz et al. 1999), which uses a combination of BSE images and x-ray elemental maps as inputs, was used to quantify the various phases in the fly ash. (Bumrongjaroen et al. 2011) used a computer automated SEM to analyze thousands of individual fly ash glass particles. The spherical glass particles were identified using aspect ratios estimated from SEM micrographs of each particle. The major elements in a selected particle and its diameter were measured along several orientations. The analysis showed that the chemical composition of the particles within the same glass can vary widely. A k-means clustering algorithm was used to define phases in each fly ash by grouping the particles into clusters based on weighted compositional centroids.

(Chancey et al. 2010) used SEM/EDS with multispectral image analysis to characterize various groups of glasses in Class F fly ash. This was based on earlier work by (Stutzman 2007), where multispectral imaging techniques were used to characterize clinker phases in anhydrous and hydrated cements. (Aughenbaugh et al. 2016) used k-means clustering coupled with multispectral image analysis to identify the glass phases in fly ash. The k-means algorithm was used to cluster glass

compositions based on spot analysis of 120 points. The compositions identified by the clusters were used as training sets for the multispectral image analysis.

(Durdziński et al. 2015) used full element mapping in EDS to map millions of points, and grouped them using various visual techniques to obtain glass subgroups, whose hydration over time was then followed. (Oey et al. 2017) used network indexes to relate glass composition to reactivity and performance.

2.3.6 Chemical Reactions in Fly Ash

ASTM C618 defines a pozzolan as a siliceous or siliceous and aluminous material which possesses little or no cementitious value by itself but will, under ideal conditions of particle size and moisture content, chemically react with calcium hydroxide at ordinary temperatures to form compounds possessing cementitious properties. The hydration products of Portland cement and fly ash are very similar to that of pure Portland cement. The hydration products include C-S-H, calcium hydroxide (portlandite), ettringite (AFt), monosulfoaluminate hydrate (AFm) and hydrogarnet.

The hydration of alite (C_3S) and belite (C_2S) in Portland cement produces calcium hydroxide according to Equations 2.9 and 2.10.

$$2C_3S + 11H \rightarrow C_3S_2H_8 + 3CH \quad (2.9)$$

$$2C_2S + 11H \rightarrow C_3S_2H_8 + CH \quad (2.10)$$

The pozzolanic reaction between CH and the silica from a pozzolan can be represented as:

$$xCH + yS + zH \rightarrow C_xS_yH_z \quad (2.11)$$

As the pozzolanic reaction progresses, the amount of calcium hydroxide diminishes with time and may be nearly reduced to zero (Helmuth 1987). The use of fly ash influences not only the amount and kind of hydrates formed but also modifies the composition of the hydrates. The calcium to silica ratio (C/S or x/y) for the C-S-H formed from the pozzolanic reaction above is typically lower than that formed from the hydration of Portland cement without fly ash and is generally agreed to have a tobermorite-like structure. C-S-H with low C/S leads to an increased uptake of aluminum in the C-S-H, resulting in the formation of C-A-S-H (Richardson and Groves 1993). Results from thermodynamic modelling by Lothenbach et. al (2011) indicates that the presence of moderate amounts of fly ash results in the destabilization of portlandite and the formation of additional C-S-H with a decreased Ca/Si ratio. As fly ash contains significant quantities of alumina but little sulfate, fly ash in Portland cement results in a decrease in ettringite and an increase in AFm content (Lothenbach et al. 2011). The C-S-H from pure Portland cement hydration has a composition of approximately 1.5-1.9CaO.SiO_2.nH2O, where the number of water molecules n depends on temperature and relative humidity. At Ca/Si ratios exceeding 1.5, C-S-H is described by disordered jennite-like units or a tobermorite structure with calcium hydroxide-like regions. At lower Ca/Si ratios, a tobermorite-like structure with defects in the silicate chains has been proposed. When aluminum is incorporated into C-S-H, C-A-S-H, a C-S-H with tobermorite-like structure is formed (Lothenbach et al. 2011). The alumina in fly ash also reacts with CH to form stratlingite or gehlenite hydrate and hydrogarnet, and calcium aluminate hydrate, ettringite, calcium monosulfoaluminate, and calcium carboaluminate (Thomas 2013).

This reaction of calcium hydroxide and silica gel produces two calcium silicate hydrates known as C-S-H I and C-S-H II. C-S-H I is a poorly crystallized material with CaO/SiO_2 molar ratios ranging from 0.8 to 1.5. C-S-H II is semicrystalline with CaO/SiO_2 molar ratio of 1.5 to 2.0 (Helmuth 1987).

Fly ash impacts the hydration of cement through the filler effect and by taking part in chemical reactions to form hydration products. The chemical reactions follow a dissolution-precipitation mechanism. The three main components of the chemical reactions are the solid reactants, the solid hydrate reaction products, and the pore solution.

In general, fly ash has lower calcium content than Portland cement. Therefore, there are differences in the hydrates formed during hydration. The main reactive phases in fly ash are the aluminosilicate glasses. The blending of Portland cement with fly ash leads to a reduction of the total amount of portlandite in the hydration products. However, this is constrained by the fact that the reactivity of fly ash is very limited, and also the CaO in the fly ash is an additional source of calcium. Due to the relatively high contents of alumina in Class F fly ashes (between 15 and 35%), the blending of Portland cement with Class F fly ash results in high amounts of alumina-rich phases.

(Takemoto and Uchikawa 1980) suggested a mechanism of for pozzolanic reaction of in the presence of C_3S and C_3A. This is more complicated than the reaction with calcium hydroxide. The pore solution is saturated by the release of calcium ions from the surface of the C_3S. These calcium ions are adsorbed onto the pozzolan particle surfaces. C-S-H formed by the hydration of C_3S precipitates on the

surface of the C_3S particles and as porous hydrates of low Ca/Si ratio on the pozzolan particles. As the pozzolan surface interacts with the pore fluid, Na^+ and K^+ ions are gradually dissolved from the surface, resulting in Si and Al-rich amorphous layers on the surfaces. These dissolved alkali ions increase the pH of the pore solution and accelerate the dissolution of SiO_4^{4-} and AlO^{2-}, which combine with Ca^{2+} to increase the thickness of the hydrate layer. Swelling by osmotic pressure in this layer creates a void between the pozzolan particle and the layer, which could rupture the layer, and release SiO_4^{4-}, AlO2-, Na+, and K+ ions into the Ca^{2+} rich pore solution, leading to the formation of additional calcium silicate and aluminate hydrates on the outer hydrates of the C_3S particles (Helmuth 1987).

The C_3A pozzolan mechanism is similar to that of C_3A clinker reaction. The pozzolan accelerates the hydration of C_3A by adsorption of calcium ions from the liquid phase, and by providing precipitation sites for ettringite and other hydrates (Helmuth 1987). The products of this interaction include ettringite, monosulfoaluminate hydrate, calcium aluminate hydrate, and C-S-H which are formed on the surface film outside the pozzolan particles or on the surface hydrate layer of the C_3A particles.

2.3.7 Effect of Fly Ash on Hydration Kinetics

Fly ash is known to have effect on hydration kinetics of Portland cement due to the "filler effect" and the chemical reactivity of the fly ash itself. The presence of a mineral addictive or even an inert material can have a significant impact the hydration of the clinker phases (Cyr et al. 2006; Gutteridge and Dalziel 1990). This is known as the filler effect. The filler effect manifests itself in two ways: through the dilution

effect, and the provision of nucleation sites for the hydration of the clinker phases (nucleation effect). The substitution of Portland cement by fly ash at the same water to binder ratio increases the effective water to cement ratio. This implies a "dilution" of the total amount of clinker phases available for hydration. Therefore, there is more space (water-filled capillary pores) for the formation of hydration products as there are fewer clinker grains. The higher effective water to cement ratio can enhance the degree of reaction of the clinker phases compared to the unsubstituted material (Baert et al. 2008; Bentz 2006; Berodier and Scrivener 2015). They can also extend the time of commencement of the deceleration period of hydration by diluting the cement content, thus providing additional space for the growth of C-S-H (Juenger and Siddique 2015).

For nucleation effects, the surfaces of the fly ash act as nucleation sites for hydrates, especially for finer fly ash particles. Fly ash and other SCMs with very small particle sizes can enhance hydration kinetics during the acceleration period by serving as nucleation sites for the precipitation of C-S-H and CH. Some researchers have observed the formation of a layer of C-S-H around siliceous fly ash particles when little of the fly ash has reacted, suggesting that the fly ash was acting as a nucleation site (Deschner et al. 2012; Juenger and Siddique 2015).

The reactivity of fly ash is dependent on the alkalinity of the pore solution, which builds up over the first few days. The reaction of fly ash ambient temperatures is slow and fly ash does not react for at least 7 days (Sakai et al. 2005). As a result, the reaction of fly ash in the first few days is usually negligible, and changes in hydration kinetics is dominated by the filler effect (Lothenbach et al. 2011).

Fly ash also influences the setting time of Portland cement systems. Low-calcium Class F fly ashes in general retards the setting of Portland cement at ambient temperatures (Carette and Malhotra 1987; Jawed and Skalny 1981). A similar effect has been reported for high-calcium Class C fly ashes (Grutzeck et al. 1984). Setting time may be retarded due to the dilution of the cement and the supply of additional sulfate from the fly ash itself.

2.3.8 Effect of Fly Ash on Compressive Strength

The compressive strength of concrete containing fly ash depends on several factors. This includes the type and characteristics of the fly ash such as its chemical and mineralogical composition, fineness, and pozzolanic reactivity; the type of cement, the replacement level of the cement with fly ash, mix proportions such as water cement ratio and air content, ambient temperature, curing temperature, curing environment, and age. The rate of reaction of fly ash is slow at ambient temperatures, so the rate of strength development is correspondingly slow, especially at early ages (Cyr et al. 2006). The pozzolanic reaction consumes lime, and the reaction products are efficient in filling up space and densifying the concrete. Due to its fineness as well as pozzolanic reactivity, fly ash in concrete significantly improves the quality of cement paste and the microstructure of the interfacial transition zone between the binder matrix and the aggregate, resulting in continual pore refinement and a gain in strength development with age (Siddique and Khan 2011). Numerous studies have shown that the long term strength and transport properties of fly ash cement blends are usually superior to those of plain Portland cement due to the refinement of the pore structure (Scrivener and Nonat 2011). In an extensive study by (Lawrence et al.

2005), it was shown that for short hydration times, the nature of the mineral admixture was not a significant parameter as mortars containing the same amounts of crushed quartz, limestone filler and fly ash of equivalent fineness had similar compressive strengths at early ages. It was also reported that the compressive strength increased with fineness of the mineral admixture due to physical effects (heterogenous nucleation), and that the gain in compressive strength due to pozzolanic activity alone in the Class F fly ashes tested was shown to be maximum when replacement rate was around 35% to 40%. In a related study by (Cyr et al. 2006), the maximum gain in compressive strength due to pozzolanic effect for the Class F fly ashes was when the replace rate was around 25% to 30%.

Low calcium Class F fly ashes do not exhibit significant pozzolanic activity to affect strength until after about two weeks of hydration. Some high calcium Class C fly ashes with calcium oxide content over 15% may start contributing to strength development in as early as 3 days because of their self-hardening and pozzolanic properties (Siddique and Khan 2011). In addition to pozzolanic activity, some Class C fly ashes are hydraulic and will react with water to produce their own space-filling hydration products.

2.4 Methods for measuring fly ash reactivity

Measuring the degree of reaction of fly ash separately from the reaction of Portland cement in blended cement mixes is very challenging. This is due to the similarity of hydration products, the filler effect of fly ash, the complex mineralogy of the amorphous and crystalline phases in fly ash, and the varying rate of reaction of fly ash depending on the alkaline environment in which it hydrates (Haha et al. 2010;

Lothenbach et al. 2011; Scrivener et al. 2015b). Several methods have been proposed to determine the degree of reaction fly ash. These can be grouped into two broad categories: direct and indirect methods. Direct methods involve quantifying the amount of unreacted fly ash or SCM remaining, while indirect methods quantify phases in the microstructure such as portlandite and bound water, enabling the back-calculation of the degree of reaction (Scrivener et al. 2015b). Direct methods include Selective Dissolution, BSE with image analysis, and NMR. Indirect methods include thermogravimetric analysis, isothermal calorimetry, and XRD.

Selective dissolution methods are based on the principle of dissolving the unreacted clinker phases, and the hydrated clinker and SCM phases, leaving behind only the unreacted SCM or fly ash as residue. Choices of dissolving agents include EDTA with NaOH, salicylic acid, piric acid, HCl and sometimes a combination of two or more dissolution agents (Haha et al. 2010). However, opinions are divided over the accuracy of such methods. Recent studies on residues by XRD and SEM methods revealed that significant amounts of clinker and hydrate phases may remain in the residue, and proposed methods to remedy them may also revealed large, non-quantifiable systematic errors (Durdziński et al. 2017; Haha et al. 2010; Lothenbach et al. 2011; Scrivener et al. 2015b).

Backscattered electron imaging can be used to determine the degree of reaction of plain Portland cement clinkers(Igarashi et al. 2004; Scrivener 2004; Scrivener et al. 1986; Zhao and Darwin 1992). It has been extended to determine the degree of reaction of blended cements to varied degrees of success (Deschner et al. 2013; Feng et al. 2004; Haha et al. 2010). In backscattered electron mode, differences

in atomic number of cement paste constituent phases produces differences in grey-level intensities of the resulting images, with the brightest phases representing clinker, and the darkest phases representing pores. This allows for identification, segmentation, and quantification of cementitious phases (Scrivener 2004). However, in fly ash blended cement pastes, there is a considerable overlap in greyscale intensities between clinker phases, anhydrous fly ash glass, C-S-H and portlandite (Feng et al. 2004; Haha et al. 2010). The heterogeneous nature of fly ash itself also makes identification and segmentation difficult and near impossible using conventional grey scale methods. Several methods have been used by various authors to mitigate this issue with varied degrees of success, including SEM point counting and various filtering algorithms to isolate and fill in fly ash particles, and manipulation of grey-level histograms.

In recent times, multi-spectral imaging analysis, a technique used for analyzing hyperspectral data such as satellite imagery has been used to characterize fly ash particles, and follow the hydration of fly ash in cement paste (Chancey et al. 2010). Lydon (Lyndon 2005) described a method of using Multispec, a multi-spectral image analysis software, to perform hyperspectral image analysis for modal analysis of mineralogy of rocks, which was later adapted by Chancey (Chancey et al. 2010) for the characterization of fly ash. In this method, a clustering algorithm is used to identify and quantify groups of mutually exclusive chemical compositions obtained by combining various elemental x-ray intensity maps in succession. This allows for the display of segmented images that provide insights into the various phases present

and their quantities. The quantities are based on the area fractions of the identified phases, which can then be converted to volume fractions based on their densities.

XRD coupled with Rietveld analysis have been used in numerous studies for identifying phases in hydrated cementitious materials and quantifying the degree of hydration of Portland cement (Juenger and Siddique 2015; Lothenbach et al. 2011; Scrivener et al. 2004; Snellings et al. 2014; Snyder and Stutzman 2013). Because XRD can only quantify crystalline phases, an internal or external standard is required in order to quantify the amorphous phases. However, this approach is not very useful in blended cements with fly ash where the main hydrate phases, C-S-H and fly ash glass are amorphous. This makes it impossible to isolate the degree of fly ash reaction from the overall degree of reaction. Therefore, studies of hydrating blended cements with XRD have largely been limited to the quantification of the degree of hydration of the clinker phases, and the identification of crystalline hydration phases. Other issues that confound XRD analysis of hydrated phases is the high number of hydrate phases and their complex composition and crystal structure. This leads to significant peak overlaps. Broad, diffuse peaks from the amorphous fly ash, C-S-H, and other hydrate phases makes phase assignment in these regions challenging. In recent times, there has been considerable interest in looking at whether the quantities of different amorphous materials can be quantified from this broad diffuse hump in the XRD diffractograms by the so called partial or no known crystal structure (PONCKS) technique (Snellings et al. 2014). The PONCKS approach combines profile summation methods with the Rietveld method. In this method, the contribution of a phase that has no or no fully known crystal structure is accounted for by assigning a

phase constant that relates the diffraction signal of the phase to its content (Scrivener et al. 2015b). However, the accuracy of this method was found to be very low compared to other methods due to no defined or standardized protocols for implementing the method, among other factors such as difficulties defining the correct background of the XRD diffractogram (Durdziński et al. 2017).

Thermogravimetry (TGA) measures the degree of reaction indirectly by measuring either bound water or calcium hydroxide. TGA has been used widely to determine the degree of reaction of Portland cement. However, it is of limited usefulness in measuring the degree of reaction of fly ash. The measurement of bound water content based on weight loss typically between 105ºC to 1000ºC is a widely used technique to assess the degree of reaction of plain Portland cement. However, when SCMs are present, the analysis becomes much more complicated as it is unrealistic to separate the bound water due to the SCM reaction from that due to the reaction of the clinker phases. Despite these drawbacks, the results of Portland cement and blended cements with SCMs can be compared to assess differences in the hydration of the two types of cements. Another technique to assess degree of reaction with TGA is the measurement of calcium hydroxide (portlandite). Since the pozzolanic reaction of fly ash and other SCMs consumes calcium hydroxide, the amount of calcium hydroxide compared to that of plain Portland cement gives an indication of the degree of reaction of the SCM. However, a serious drawback of this method is that it neglects the calcium provided to the pozzolanic reaction from the C-S-H formed from the clinker reaction. The decreasing Ca/Si ratios of the C-S-H formed from pozzolanic reactions indicates that the reaction of SCMs not only forms

new C-S-H with lower Ca/Si ratios, but also takes up Ca existing in C-S-H. This means the consumption of portlandite observed corresponds to much more SCM reaction than will be if no calcium was provided from the C-S-H (Durdziński et al. 2017). Therefore, the degree of reaction obtained by analysis of portlandite consumption is underestimated. TGA also neglects the filler effect. The reaction of the clinker may be accelerated and enhanced due to filler effect, leading to the production of more portlandite especially during the first few days of hydration. As fly ash reacts slowly in the first few days, more portlandite may be observed in Portland cement fly ash pastes than in pure Portland cement pastes.

Isothermal calorimetry involves the measuring of the heat released during hydration. The intensity of the various hydration peaks can be used as a measure of the progress of reaction. Isothermal calorimetry has been used to quantify the hydraulic activity of Portland cement and the pozzolanic activity of fly ash and other supplementary cementitious materials in numerous studies (Baert et al. 2008; Gruyaert 2010; Pane and Hansen 2005). The advantage with isothermal calorimetry is that the reaction can be followed continuously. However, it is of limited value in the early days of hydration where fly ash reaction is limited. It is useful for comparative analysis. The filler effect can also confound results at early ages, but it can distinguish the aluminate hydration bump, which is useful for qualitative analysis.

A method of measuring the growth of the C-S-H gel by neutron scattering is small angle neutron scattering (SANS). This measures the distribution of pore sizes by the contrast in the neutron scattering cross-sections at the interface between the gel

structure and the pore space. It can measure pore sizes to less than a nanometer. Bumrongjaroen et al. (2009) applied it to the investigation of fly ash reactivity.

Chapter 3: Preparation of Simulated Fly Ashes

3.1 Particle Analysis by Automated SEM (ASEM)

The preparation of synthetic fly ash glasses used in this research is a continuation of earlier work done by (Bumrongjaroen et al. 2011), where the details of the automated SEM procedure used to characterize the fly ash can be found. Synthetic fly ash glass refers to the glass that was made from various oxides. Simulated fly ash refers to the fly ash made from the combinations of the synthetic fly ash glasses and crystalline phases. The approach is summarized below:

Instead of using bulk chemical composition to characterize the fly ash, an automated scanning electron microscopy (ASEM) that analyses the chemical composition of thousands of fly ash particles is used. Using this approach, the major elements in a selected particle and its diameter along several orientations are measured. Since glassy particles are formed from cooling droplets of melted clays and other minerals, they have nearly spherical shapes in contrast to more angular shapes of crystalline particles. The glass particles are identified using their circularity (aspect ratio) estimated from a 64 x 64-pixel micrograph of each particle, while the crystalline particles are identified using their characteristic elemental ratios. X-ray intensity data and size and shape parameters for approximately 10,000 particles were collected at 2000x magnification. The system was set to select glass particles for analysis based on their circularity (≤ 1.3) and particle size (< 100 μm). This length scale is the size range of typical fly ash particles. Each selected particle was analyzed for 16 elements: Na, Mg, Al, Si, P, S, K, Ca, Ti, Fe, Ni, Zr, Ba, Ce, and Pb. A typical

analysis of Coal Creek fly ash is shown in Figure 3.1. For better visualization of the elemental data, the particle compositions are plotted in triaxial coordinates corresponding to glass formers (right), alkali modifiers (bottom) and alkali-earth (left). Each point in the plot represents the composition of a single particle.

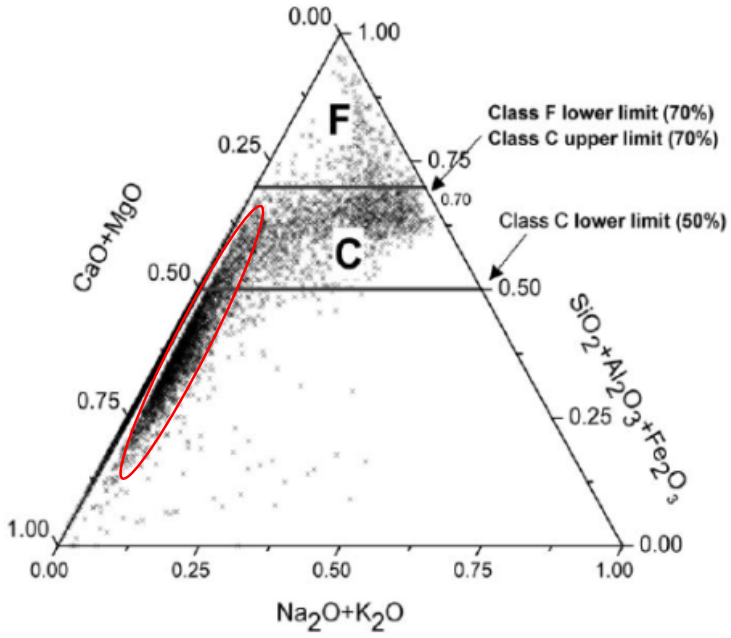

Figure 3.1 Composition of Coal Creek fly ash glass particles

As can be seen, the composition of the particles varies widely across the ASTM C618 Class C and F classifications, illustrating the inadequacy of the ASTM C618 classification.

Cluster Analysis

The particle compositions shown in Figure 3.1 can be grouped into clusters based on mean chemical compositions. Several clusters can be seen in the plot, for example the cluster that runs parallel to the CaO+MgO axis below the lower limit of

the Class F line ($SiO_2+Al_2O_3+Fe_2O_3 = 0.7$), highlighted with the red circle. Each cluster has a characteristic chemical composition that reflects the precursor clay minerals, and thus a characteristic reactivity. This suggests that it might be possible to predict the reactivity of the overall fly ash based on the quantities (fractions) and characteristic reactivities of these clusters. Each cluster is defined by its weighted compositional centroid and the boundary in chemical compositional space which encloses all the members of the cluster using a k-means clustering algorithm. The number of clusters, k, is specified in advance. The centroid of the cluster is the mean chemical composition of the cluster. The cluster algorithm assigns a particle to a cluster based on some distance metric in the compositional space. The distance metric in the compositional space used for the clustering was Euclidian, following the rules of orthogonal vector space geometry. Once all the particles belonging to a cluster have been assigned to the cluster, the cluster boundary is drawn around the extreme values of the cluster. Outliers are generally ignored. With the Coal Creek fly ash, seven constituents K_2O, Na_2O, CaO, MgO, SiO_2, Al_2O_3 and Fe_2O_3 were used for the analysis, and the number, k, of clusters was also limited to 7. The cluster analysis was done using open-source software in R. The number of clusters is arbitrary but decreasing the number of clusters tends to reduce the precision of in class statistics. Consequently, increasing the number of clusters reduces the summarization and predictive power of the derived clusters. The clusters obtained by analyzing spherical particles using this approach for Coal Creek fly as is shown below. The seven clusters found in the analysis appear red, magenta, green, blue, cyan, yellow and black.

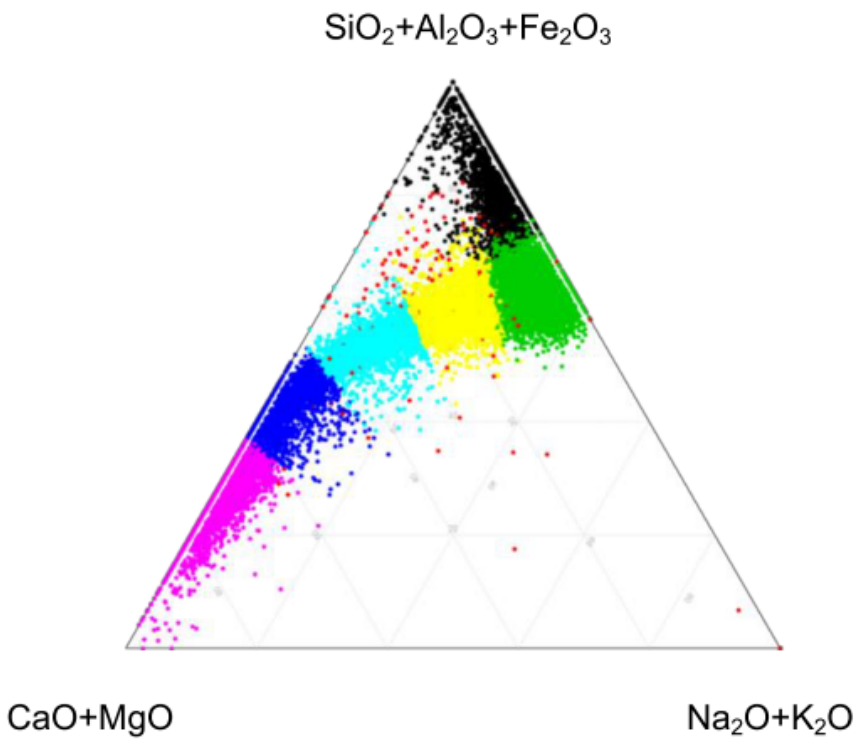

Figure 3.2 Clusters of spherical particles of Coal Creek fly ash in CaO+MgO-$SiO_2+Al_2O_3+Fe_2O_3$-Na_2O+K_2O coordinates

Table 3.1 Classification of Glassy Phase based on Cluster Analysis of Coal Creek Fly Ash

Cluster No.	Color	Name	Number (%)
1	Black	Si-Al-Fe glass	9.57
2	Red	Trace element	1
3	Green	Si-Al-Fe glass	32.67
4	Blue	CAS glass	11.85
5	Cyan	CAS glass	11.93
6	Magenta	Ca rich glass	15.64
7	Yellow	CAS glass	17.34

It can be seen the boundaries of the clusters are clearly separated from one another. The green cluster, Si-Al-Fe, has the highest number of particles (33%). The average composition of this cluster is 56% Si-Al-Fe and 28% alkali content. In order to relate the clustering observed in the ASEM data to conventional mineralogical analysis, the cluster data is also plotted as oxides in a CaO-Al_2O_3-SiO_2 ternary diagram. Note that the colors in this CaO-Al_2O_3-SiO_2 diagram do not represent the same clusters as found in Figure 3.1.

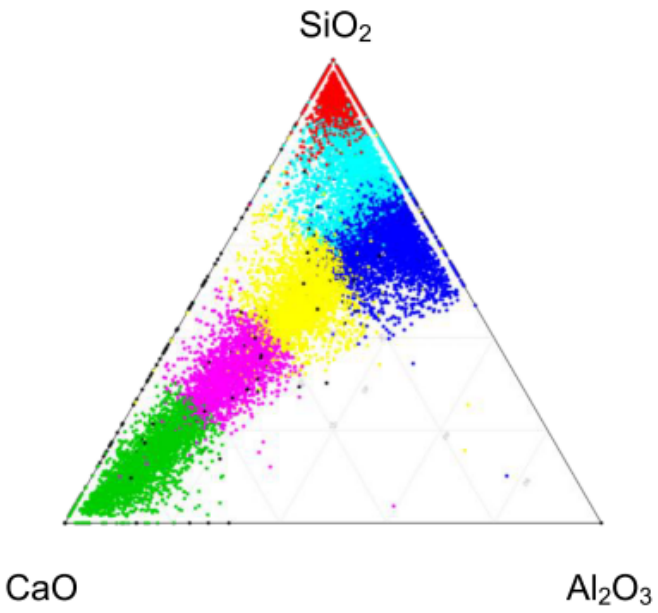

Figure 3.3 Clusters of spherical particles of Coal Creek fly ash in CaO-Al_2O_3-SiO_2 coordinates

The ternary diagram suggests that the clusters arise from the original chemical composition of the inorganic minerals in the coal. Most of the clusters found in Coal Creek fly ash are the green, blue, cyan magenta and yellow clusters. The difference between these clusters is the CaO and SiO_2 content for which as CaO decreases the SiO_2 content increases in compensation.

Clusters vs Standard Classes

A fly ash classification system based directly on clusters will be problematic, since the set of clusters are specific to a given data set. The cluster centroids and boundaries will vary from one fly ash sample to another. The number of clusters, k, may even be different, making it impossible to compare fly ashes using their respective clusters. A way to get around this is to develop a set of standard clusters

and then evaluate how well a data set fits that standard set. This set is developed based on statistical analysis of the clusters analyzed from a variety of actual fly ashes. Since the centroid of each of these standard clusters is of a specific chemical composition, this also defines a set of standard glasses. The composition of Coal Creek fly ash (CC) obtained by cluster analysis is given in Table 3.2. The clusters are named Hi-Si, Al-Si, Lo-Ca, and Hi-Ca. CC is the chemical composition of Coal Creek fly ash.

Table 3.2 Composition of Major Clusters in Coal Creek Fly Ash (Hi-Si, Al-Si, Lo-Ca, Hi-Ca)

Phase (Wt. %)	**CC**	**Hi-Si**	**Al-Si**	**Lo-Ca**	**Hi-Ca**
SiO_2	52.37	76.37	54.01	44.34	21.90
Al_2O_3	16.01	6.40	21.50	17.77	13.31
Fe_2O_3	6.12	5.63	5.35	7.53	11.78
CaO	12.43	3.72	6.67	24.56	44.14
Na_2O	3.10	2.46	4.16	1.30	0
MgO	3.93	1.64	3.41	1.35	2.69
P_2O_5	0.24	0	0	0	1.07
SO_3	1.16	0	0	0	4.37
K_2O	2.64	3.52	4.05	0.79	0.08
TiO_2	0.60	0.26	0.72	1.90	0.66

3.2 Preparation of Synthetic Fly Ash Glasses

The synthetic fly ash glasses were prepared from mixtures of the oxides of pure SiO_2, Fe_2O_3, Al_2O_3, Na_2O, CaO, MgO, and K_2O based on the composition of the clusters analyzed in the Coal Creek fly ash in Table 3.2. When necessary, small adjustments were made in the composition to correct for any crystalline component

that may have been included in the glass composition due to misclassification of particles by the CCSEM algorithm. This was done by comparing the CCSEM results with bulk XRD data.

Table 3.3 shows an example of the recipe used to prepare Lo-Ca glass. The recipe shows the oxides and the corresponding chemicals from which they were obtained, as well as the weight proportions used to prepare about 200g of glass. The weight of the raw mixture is slightly higher than 200g to account for losses during the melting, grinding, and sieving process. The pure oxides were carefully weighed in a high precision balance according to the prepared recipe. After batching according to the recipe, the mixture is thoroughly mixed and melted in a platinum crucible to a temperature of 1450-1600°C for three hours (Figure 3.4).

Table 3.3 Recipe for Lo-Ca glass

Oxide	**Expected Weight (%)**	**Chemicals**	**Assay**	**Real Assay**	**Target (g)**	**Real Target (g)**	**Actual Weight (g)**
Al_2O_3	17.77	Al_2O_3	0.995	0.99	35.72	35.90	35.9
CaO	24.56	$CaCO_3$	1	0.99	87.66	88.55	88.55
Fe_2O_3	7.53	Fe_2O_3	0.999	0.99	15.08	15.22	15.24
K_2O	0.79	K_2CO_3	0.99	0.99	2.36	2.36	2.36
MgO	1.35	MgO	0.997	0.975	2.71	2.77	2.77
Na_2O	1.3	Na_2CO_3	0.9997	0.995	4.44	4.46	4.46
SiO_2	44.34	SiO_2	0.995	0.995	89.13	89.13	89.13
TiO_2	1.9	TiO_2	0.995	0.995	3.83	3.83	3.82
SO_3	0.45	Na_2SO_4	0.99	0.99	1.62	1.62	1.62
Sum	99.99	Total batch (g)			242.55	243.84	243.82
Total glass (g)					200		

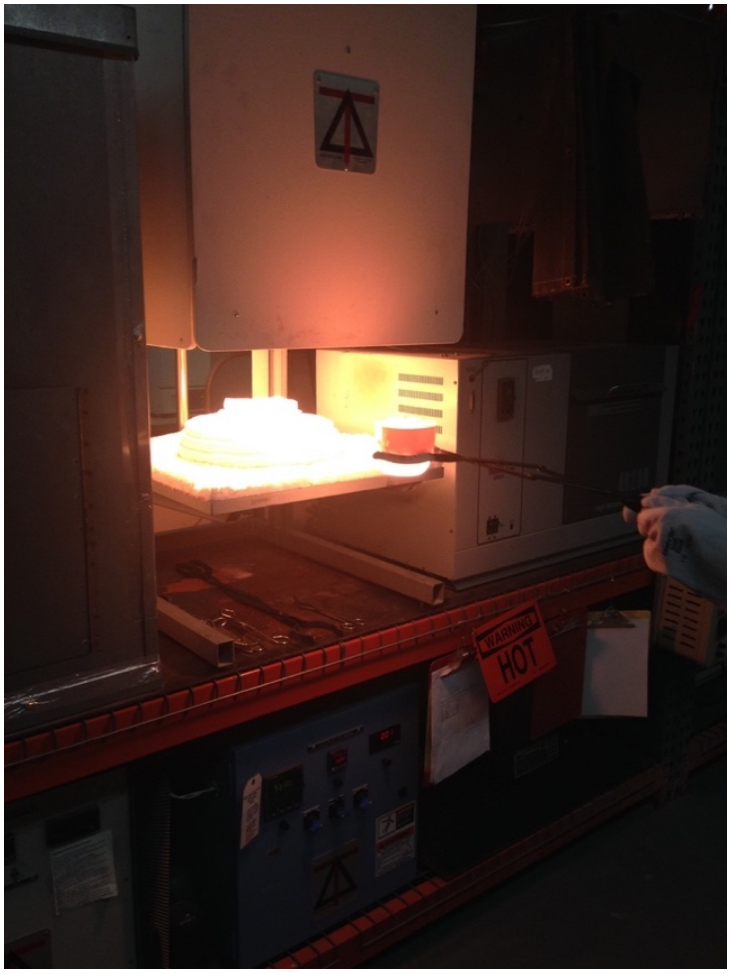

Figure 3.4 High temperature oven used for melting glass

Figure 3.5 Molten glass removed from oven

The mixtures with high contents of SiO_2 and Al_2O_3 require high temperatures to achieve a low enough viscosity to allow homogenization and pouring from the crucible. The melts were immediately quenched on ice and left to cool in air to create the fly ash glass (Figure 3.6).

Figure 3.6 Simulated fly ash glass in platinum crucible after cooling

3.2.1 Grinding and Sieving of Synthetic Glass

The glass was ground in a grinding machine sieved through ASTM sieve nos. 100, 200, and 325, corresponding to sizes 150µm, 75µm and 45µm respectively. For each synthetic glass, the particle size distribution was as follows:

Table 3.4 Particle size distribution for synthetic fly ash glasses

Size (µm)	**Sieve Mesh**	**% passing**
<45	passed 325 mesh	82.13
45-75	325-200	12.01
75-150	200-100	5.29
>150	retained on 100 mesh	0.57
	Total	100

3.2.2 Verification of Glass Composition

The chemical composition of the glass was verified by XRF in order to ensure that the targeted composition was met. The glass was deemed satisfactory when the XRF composition was within +/-1% of the chemical composition of the starting oxides. The composition of the glass was verified by XRF. The XRF results for LoCa glass is shown in Table 3.5 below.

Table 3.5 Expected composition versus XRF composition for Lo-Ca glass

Oxide (Wt. %)	**Expected**	**XRF**
Al_2O_3	17.77	17.068
CaO	24.56	24.832
Fe_2O_3	7.53	7.152
K_2O	0.79	0.856
MgO	1.35	1.288
Na_2O	1.3	1.795
SiO_2	44.34	44.843
TiO_2	1.9	1.921
SO_3	0.45	0.213

3.2.3 Glass Densities

The densities of the synthetic fly ash glasses were measured by helium pcynometry at NIST. The results are shown in Table 3.6.

Table 3.6 Densities of synthetic fly ash glasses

Synthetic Fly Ash Glass	**Al-Si**	**Hi-Si**	**Hi-Ca**	**Lo-Ca**
Density (g/cm^3)	2.6032	2.4424	3.1209	2.8605
Standard Deviation (g/cm^3)	0.0024	0.0019	0.0027	0.0031

3.3 Preparation of Simulated Fly Ashes

The simulated fly ashes were made from the four synthetic glasses. Various proportions of the glasses were combined to obtain the desired chemical compositions. Minerals were added to obtain the crystalline phases. Each simulated fly ash had about 90.64% glass, 8.44% crystalline phases and 0.92% Fe. The crystalline phases added to each simulated fly ash is shown in Table 3.7.

Table 3.7 Mineral (crystalline) phases in synthetic fly ash glass

Phase	**Wt. (%)**
Quartz	4.89
Anhydrite	0.56
Hematite	0.44
Magnetite	0.44
Periclase	2.11
Sum	8.44

Three simulated fly ashes (CC1, CC2, and CC3) were prepared to investigate the effect of their glass variation on their performance. CC1 was prepared based on composition of Coal Creek fly ash. CC2 has 5% lower Al-Si glass content than CC1 which is compensated by a 5% increase in Hi-Si content. CC3 has 5% higher Al-Si content, 5% lower Hi-Si content, 10% higher Hi-Ca, and 10% lower Lo-Ca content compared to CC1. This fly ash is designed to be more reactive than the other fly ashes since it has higher fraction of reactive glasses. To obtain the various simulated fly ashes, the glass and crystalline phases were combined in the weight proportions shown in Table 3.8 below.

Table 3.8 Glass and crystalline proportions in simulated fly ashes

Wt (%)	**CC1**	**CC2**	**CC3**
Hi-Si	21.97	26.55	17.40
Al-Si	35.71	31.13	40.29
Hi-Ca	10.99	10.99	21.97
Lo-Ca	21.97	21.97	10.99
Fe	0.92	0.92	0.92
Mineral	8.44	8.44	8.44
Total FA	100.00	100.00	100.00

The mixture of the various glasses and crystalline phases were mixed thoroughly using a resonance acoustic mixer to obtain the simulated fly ash (Figure 3.7). The simulated fly ash after mixing is shown in Figure 3.8.

Figure 3.7 Mixing of simulated fly ash in resonance acoustic mixer

Figure 3.8 Simulated fly ash after mixing

Figure 3.9 shows the composition of raw fly ash, each simulated fly ash and each synthetic fly ash glass in ternary diagram. Although the bulk composition of CC1, CC2, and CC3 are quite similar but their glass fractions are varied. The difference in reactivity that they may have would depend on the combining effect of these glasses.

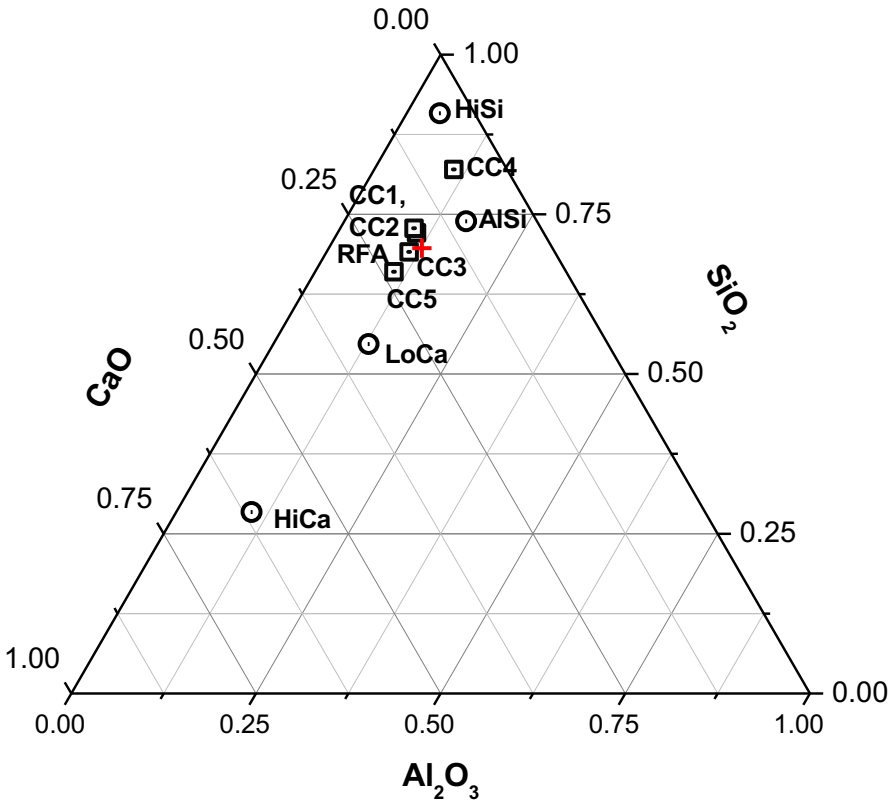

Figure 3.9 CaO-Al_2O_3-SiO_2 diagram of raw fly ash (RFA), Hi-Si, Al-Si, Lo-Ca, Hi-Ca, CC1, CC2, CC3 in mole ratio

3.3.1 XRF of Synthetic Glass and Simulated Fly Ashes

The chemical composition of the simulated fly ashes was measured using XRF. The results are shown in Table 3.9.

Table 3.9 XRF results of simulated fly ashes

Phase	**CC1**	**CC2**	**CC3**
Al_2O_3	13.884	13.094	14.321
CaO	12.242	12.331	13.897
Cl	0.013	0.012	0.015
CuO	0.008	0.008	0.007
Fe_2O_3	6.413	6.413	6.593
K_2O	2.384	2.314	2.223
MgO	6.636	6.57	7.061
Na_2O	2.506	2.365	2.605
P_2O_5	0.152	0.157	0.313
SiO_2	54.931	55.965	52.286
SO_3	0.064	0.056	0.046
TiO_2	0.749	0.708	0.62
Total	**100.00**	**100.00**	**100.00**

3.3.2 Density of Fly ash

The density of the simulated fly ash glasses was determined by helium pycnometry at NIST.

Table 3.10 Density of cement, real fly ash, and simulated fly ashes

Sample	**Density (g/cm^3)**
CEM	3.1029
RFA	2.4474
CC1	2.6838
CC2	2.6743
CC3	2.7195

3.3.3 Particle Size Distribution

The particle size distribution of the synthetic glasses and simulated fly ashes were measured at VSL and NIST.

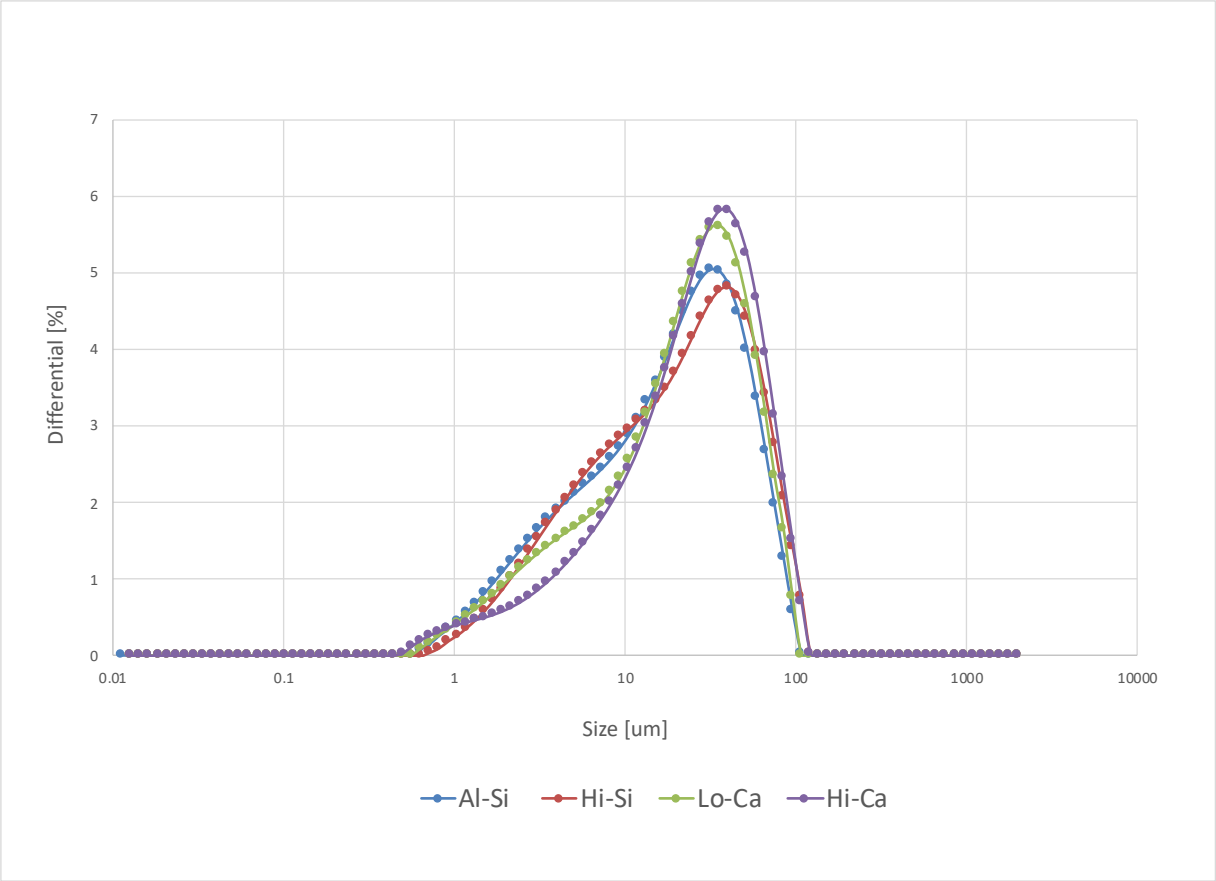

Figure 3.10 Particle size distribution of synthetic fly ash glasses

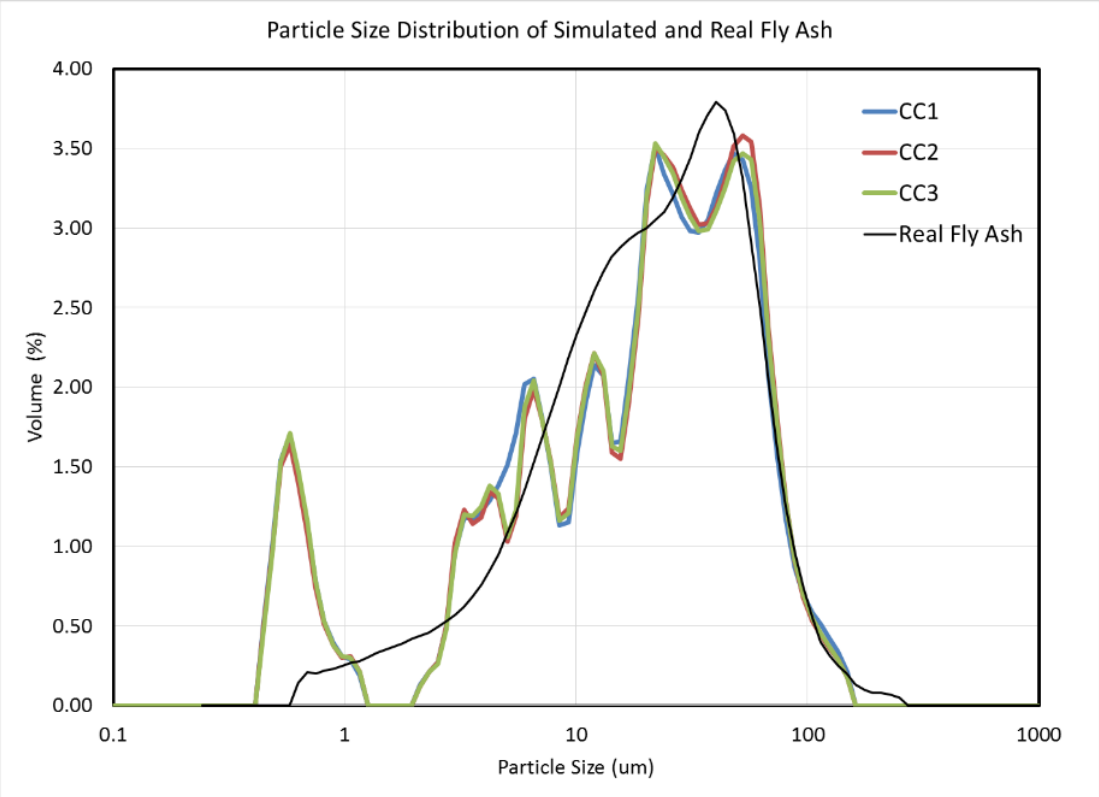

Figure 3.11 Particle size distribution of simulated fly ashes

Chapter 4: Sample Preparation, Materials, and Experimental Methods

4.1 Experimental Methods

4.1.1 Scanning Electron Microscopy

Scanning electron microscopy (SEM) uses a focused beam of electrons to reveal the structure and details of organic and inorganic materials to micro (μm) and nanometer (nm) scale in details that cannot be revealed by optical microscopy. The area or sample to be observed is bombarded with a beam of electrons generated by an electron gun. The electron beam scans across the sample and a detector records the signals. When coupled with Energy Dispersive X-ray spectroscopy (EDS), it can be used for elemental analysis on a micrometer scale.

The SEM consists of a microscope column which includes an electron gun at the top, a column down which the electron beam travels, and a sample chamber at the base of the column. The column is used to focus and illuminate the specimen using the electron beam generated by the electron gun. As the electron beam scans the specimen, secondary and backscattered electrons are produced and detected by a signal processor, which amplifies the signal to produce an image. Unlike optical microscopy, the SEM uses magnetic lenses instead of optical lenses. Secondary electrons are produced through inelastic scattering of loosely bound valence electrons in the atoms of the specimen by the beam electrons. The interaction of the beam electrons with the sample causes these secondary electrons to be ejected from the atom and set into motion. Therefore, some of these secondary electrons will

propagate through the sample, and some will intersect the surface and escape. Secondary electrons have energies less than 50eV (Goldstein et al. 2003). Because of these low energies, secondary electrons are ejected only from surface layers, making them suitable for revealing topographical information. A positively charged detector is used to attract these low-energy electrons where the signal is processed to produce an image.

Backscattered electrons are high energy electrons produced from elastic scattering of the incident electron beam by the atoms in the sample that results in the incident electrons re-emerging from the specimen. Therefore, the electron is said to have backscattered or re-emerged from the sample. A detector attracts these electrons to produce an image. Because of the large scattering angles (more than 90 degrees), the scattered electrons propagate towards the direction the incident beam. Backscattered electrons have higher energy than secondary electrons and so are detected to greater depths in the sample than secondary electrons (Figure 4.1). Thus, secondary electron (SEM) has higher resolution (finer detail) than backscattered electron (BSE) images.

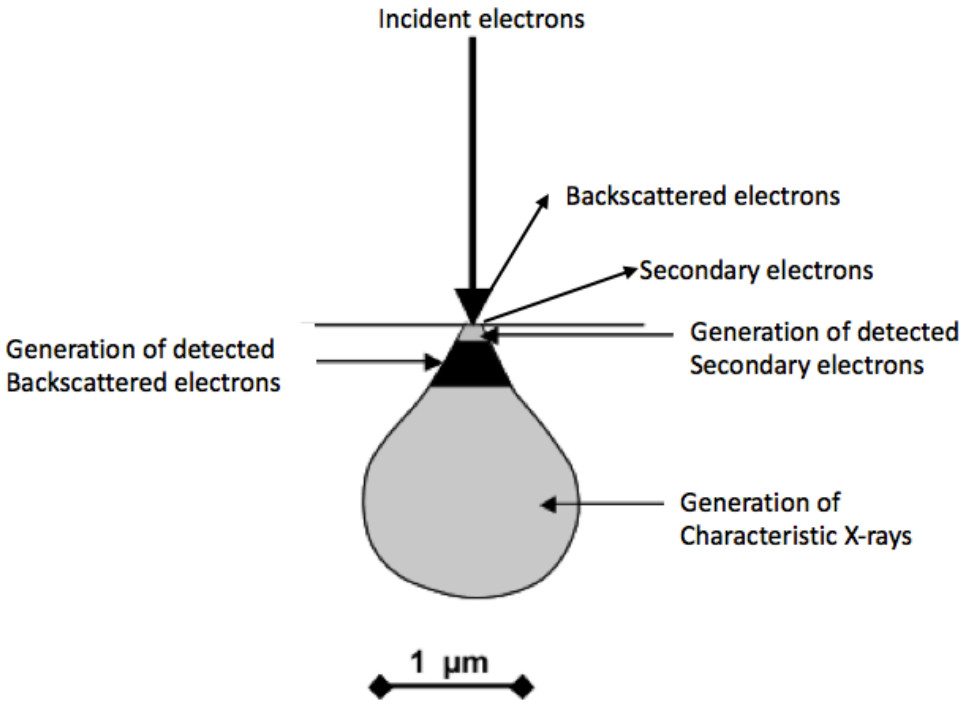

Figure 4.1 Generation of SE and BSE (adapted from (Scrivener 2004))

BSE images are commonly used for compositional analysis to determine the chemical composition in a sample and the spatial differences in the sample's chemical composition. The intensity of the BSE signal is a function of the average atomic number of the local sample area. The higher the mean atomic number of a material, the higher the intensity of its BSE signal (backscatter coefficient), and the brighter it appears on a backscattered image. Conversely, phases with lower average atomic numbers have lower backscatter coefficients and appear less bright on backscattered images (Zhao and Darwin 1992). This makes BSE images very useful for determining the chemical composition of a sample. The incorporation of water during hydration leads to hydrate phases which have much lower average atomic numbers than the anhydrous phases, and thus a strong contrast is obtained between unreacted

(anhydrous) and reacted (hydrate) phases (Scrivener 2004). The differences in contrast correspond to the grey level intensity of BSE images. BSE images captured in an SEM have grey level intensities ranging from 0 (black) to 255 (white). There is weaker, but still discernible, contrast in the anhydrous phases, with the ferrite phases appearing brightest, followed by alite, aluminate, and belite which have similar grey level intensities. Within the hydrates, portlandite is significantly brighter than the other hydrates. However, it is not possible to differentiate between the other hydrates (i.e., C–S–H, ettringite, AFm phase, etc.) on the basis of grey level alone (Scrivener 2004). A representative grey level histogram of BSE images of Portland-fly ash blend after 28 days of hydration is shown in Figure 4.2 (Deschner et al. 2013).

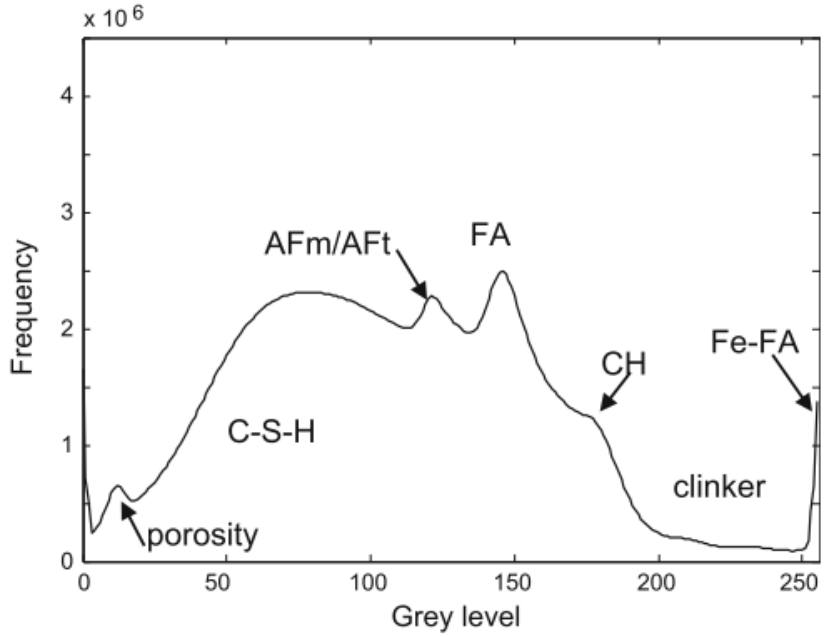

Figure 4.2 Representative grey level histogram of BSE images of Portland-fly ash blend after 28 days of hydration (Deschner et al. 2013)

BSE images are most useful when topographical effects are eliminated, hence the need for flat polished surfaces.

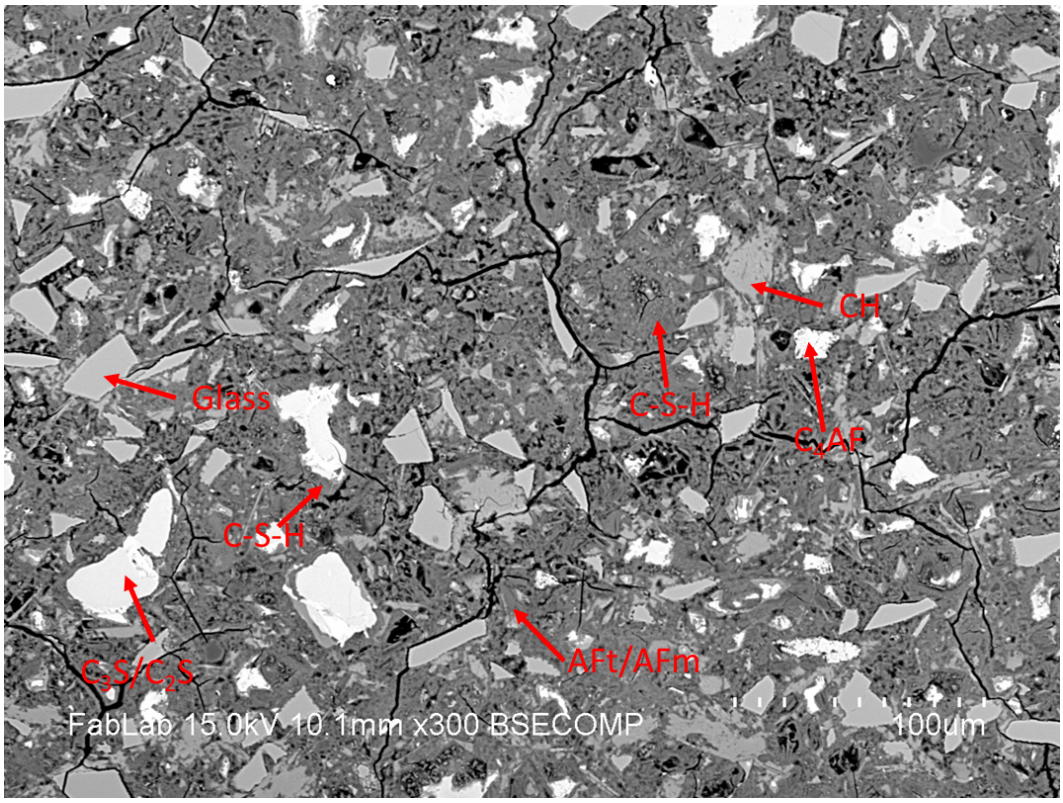

Figure 4.3 BSE image of LoCa sample at 90 days

When equipped with energy dispersive X-ray spectroscopy (EDS), the EDS can be used to determine the chemical composition of specific areas of the sample through spot analysis or the collection of x-ray maps of various elements over a specified area. The incident electron beam generates x-rays in the interaction volume beneath the surface of the sample with energies specific to the elements within the interaction volume. The EDS equipment is used to detect these characteristic x-rays, from which the chemical composition of the interaction volume can be determined. EDS generates spatial maps of each element being analyzed separately. These maps can be overlapped to determine the elemental composition of the area being observed. For cementitious materials, the interaction volume is around 1-2µm across, which is

larger than the size of many hydrate phases, therefore the analyses typically come from mixtures of phases.

Coupled with image analyses, they can be used for quantitative analyses of hydrate and anhydrous phases. However, due to the heterogeneity of fly ash, the application of BSE/image analysis to fly ash cement pastes faces a lot of challenges. Grey scale sedimentation falls short, and dilation-erosion techniques are cumbersome and subjective. This is due to the overlap of grey level intensities of certain hydrate phases such as calcium hydroxide with that of the fly ash particles. Several methods have been tried to various degrees of success, such as SEM point counting. Recently, multispectral imaging has been used as a way to overcome some of these challenges.

4.1.2 Multispectral Imaging Analysis

A multi-spectral image is a collection of several monochrome images of the same image, each of them taken with a different sensor sensitive to a unique wavelength. A well-known example of a multi-spectral image is an RGB color image, consisting of a red, a green, and a blue image taken with sensors with different sensitivities. Multi-spectral imaging is commonly used in satellite imagery. Many satellites, such as the Landsat group of satellites, produce multispectral images by recording images of the earth surface in different wavelengths or bands in the visual and non-visual range such as visible light, infrared and ultraviolet. The images from these individual bands can then be linked together to form a composite multispectral image. Lyndon (2005) adapted this principle to the investigation of rock mineralogy by analyzing a series of overlayed x-ray maps obtained from EDS analysis. Each spectrum or band is represented by an x-ray map of an element. By combining images

from different element x-ray maps, the chemical composition of various regions in the image can be identified and quantified. The individual x-ray images or channels are mathematically linked together into one multispectral image. The multispectral image is then divided into areas with similar multi-channel characteristics, defined by similar gray-level values (0-255) of the multispectral image, by automated mathematical cluster analysis or user defined training sets. Based on the cluster analysis or user defined training sets, the image is segmented into areas of similar fields and quantified.

Images from cement-based materials are complicated by the fact that a pixel could represent multiple phases. This makes grey-scale segmentation difficult. An alternative to grey-scale segmentation is to statistically analyze the matrix of greyscale values which are formed by a series of overlaid x-ray maps to determine clusters with similar statistical distributions. This can be done with training sets, which are used to train and assign similar phases, and automated clustering which utilizes statistical similarities based on the grey scale matrix.

4.1.3 Electron Microprobe Analysis (EMPA)

Electron microprobe analysis (or electron probe microanalysis) is very similar to SEM but is mainly used for chemical analysis instead of imaging. EMPA is a fully qualitative and quantitative method of non-destructive elemental analysis of micro-sized volumes at the surface of materials. EMPA works by probing the surface of a sample with high-energy electrons, thereby emitting characteristic X-rays by the various elements in the sample. Because the wavelengths of the X-rays are

characteristic of the emitting elements, the sample composition can be determined. The emitted X-rays can be identified by wavelength-dispersive spectroscopy (WDS) or EDS. WDS spectrometers operate based on Bragg's law and use various moveable, shaped monocrystals as monochromators. The microprobe used in this work is JOEL JXA-8900 Microprobe equipped with WDS and EDS.

4.1.4 Thermogravimetric Analysis (TGA)

Thermogravimetric analysis measures physical and chemical changes in a material of a function of increasing temperature applied at a constant rate. Many researchers have used TGA to measure calcium hydroxide in hydrating Portland and blended cements. TGA can also be used to determine the presence of other phases in Portland cement pastes. The differential of the TG curve (DTG) produces peaks that signify the presence of certain phases at certain temperatures.

4.1.5 Phase identification with TGA

Certain reactions occur in the cement paste at high temperatures. The DTG reveals peaks that are otherwise not visible in TG curve (Figure 4.4). The first major endothermic peak, which corresponds to a mass loss on the TG curve up to about 150^{o}C, is attributed to the de-hydration of the C-S-H phase and other hydrated phases such as ettringite, monocarbonaluminate, and monosulfoaluminate (Alarcon-Ruiz et al. 2005; Esteves 2011). Within this major peak, there are smaller peaks around 105^{o}C and 175^{o}C. The peak around 105 ^{o}C is due to the dehydration of ettringite, while the peak around 175 ^{o}C is due to the AFm phase (Deschner et al. 2012). The mass loss is due to weakly bound water in the gel solid, which is physically adsorbed.

The evaporable water and some part of the bound water escapes with the temperature range of 50°C to 105°C. In general, the evaporable water is considered to be completely eliminated around 120°C (Alarcon-Ruiz et al. 2005). The second major endothermic peak, which corresponds to the mass loss from 420°C –550°C, is due to the dehydroxylation of calcium hydroxide (CH) (Taylor 1997). The mass loss above 550°C is partly due to CO_2 (the decomposition of calcium carbonate) and partly to the final stages of the dehydration of C-S-H and the hydrated aluminate phases (Taylor 1997). The decarbonation of calcium carbonate (calcite) is due to the carbonation of the samples during sample preparation and storage and happens over a temperature range of 550°C to 750°C. The decomposition of calcite around 750°C results from the carbonation of C-S-H. The peak around 900°C is also due to decomposition of calcite (Alarcon-Ruiz et al. 2005). These peak positions will vary based on the technique and equipment, but their relative positions will not (Taylor 1997).

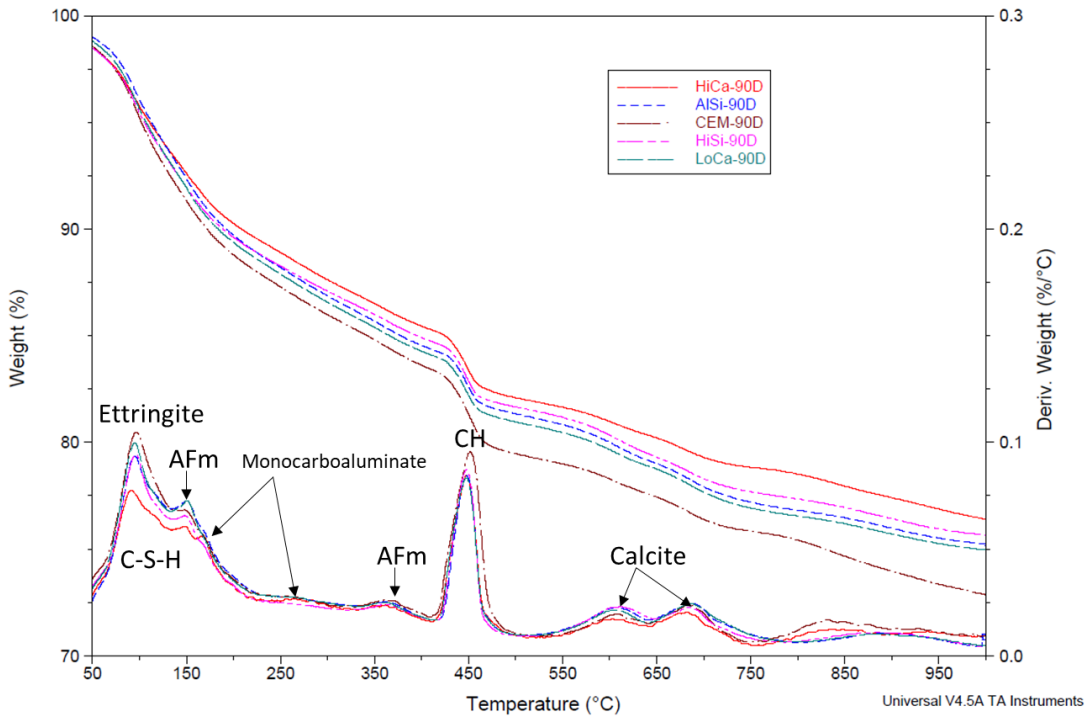

Figure 4.4 Typical TG/DTG of hydrating synthetic fly ash glass

4.1.6 Degree of Hydration

Several methods have been proposed for determining the degree of hydration of cementitious materials using TGA. The most widely used method to assess the degree of reaction of plain Portland cement is the evaluation of the bound water content based on the weight loss between 105ºC and 1000ºC (Scrivener et al. 2015b). The method proposed by (Bhatty 1986) is used in this work to calculate chemically bound water and the degree of hydration as shown in Equations 4.1 and 4.2. In general, the decomposition of cement hydrates can be divided into three major phases. The first phase between 25ºC and 400ºC represents the evaporable water and decomposition of hydrates. This peak can be divided into two phases. The first phase with the temperature range of 25-105 ºC corresponds to the free water, and within 105-400 ºC represents the dehydration reaction. The second phase, between 400ºC

and 600°C corresponds to the dehydroxylation of portlandite (Ldx). The third phase between 600°C and 800°C (Ldc) corresponds to the decarbonation of calcite (Deboucha et al. 2017).

$$W_B = Ldh + Ldx + 0.41(Ldc) \quad (4.1)$$

$$\alpha = \frac{W_B}{0.24} * 100 \quad (4.2)$$

$$Ca(OH)_2 + CO_2 \rightarrow CaCO_3 + H_2O \quad (4.3)$$

$$CaCO_3 \rightarrow CaO + CO_2 \quad (4.4)$$

$$W_{B\ carbonated\ CH} = \frac{W_{mH_2O}}{W_{mCO_2}}.Ldc = 0.41Ldc \quad (4.5)$$

where Ldh, Ldx, and Ldc are the relative mass loss on the TGA curves during dehydration of C-S-H and the AFt/AFm hydrates, dehydroxylation of CH, and decarbonation of $CaCO_3$, respectively. W_B is the chemically bound water at any given time and α is the degree of hydration. The value of 0.41 is a conversion factor to calculate the chemically bound water derived from carbonated portlandite. Equations 4.3 and 4.4 represent the reactions that take place during the carbonation of calcium hydroxide (CH) and the subsequent decomposition of carbonates. This value is obtained by dividing the molecular weight of H_2O by the molecular weight of CO_2 (molecular weight of H_2O=18 $gmol^{-1}$; molecular weight of CO_2=44 $gmol^{-1}$). In

Equation 4.2, the value of 0.24 is the chemically bound water at infinite time, estimated from theoretical stoichiometry of cement using Bogue's formulae. Bhatty used this value for both pure and tailing cement. The limit temperatures for Ldh, Ldx, and Ldc vary by authors. The limits used by (Bhatty 1986) were 105-440°C, 440-580°C, and 580-1000°C for Ldh, Ldx, and Ldc respectively. In this work, the limits were obtained from the DTG curve as shown in Figure 4.5.

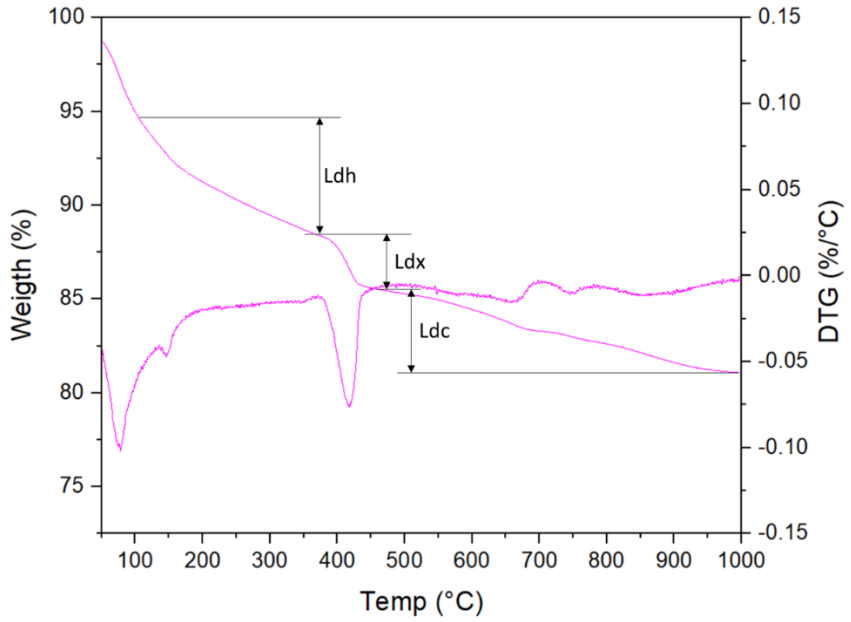

Figure 4.5 Generic TGA-DTG curve showing limits of Ldh, Ldx, and Ldc

4.1.7 Isothermal Calorimetry

Isothermal calorimetry involves measuring the heat of hydration of the reaction. The intensity of the various hydration peaks can be used as a measure of the reactivity. Isothermal calorimetry has been used to follow the reaction of fly ash and cementitious materials in numerous studies. The advantage with it is that the reaction

can be followed continuously. However, it is limited value in the early days of hydration, where fly ash reaction is limited. However, it gives an indication of the modifying effects of fly ash, in terms of nucleation and the filler and dilution effects, and the enhancements of the aluminate peaks due the effect of fly ash.

4.1.8 Thermoporometry (Low Temperature DSC)

Cement paste has a porous microstructure with pores ranging from macropores to micropores. Pores in cement pastes include gel pores, capillary pores, hollow-shell pores, air voids, as well as internal discontinuities in the cement paste associated with dimensional instabilities such as cracks resulting from drying shrinkage (Aligizaki 2006). Gel pores are the pores contained in the colloidal amorphous C-S-H gel. They are a few nanometers in size. The Jennings model has been proposed to explain the pores inside the C-S-H gel.

Thermoporometry relies on the principle of water freezing and thawing in confined pores. This method has been used to investigate the porosity of cementitious materials. The method is based on the liquid-solid transformation of a capillary fluid inside a porous medium with changing temperature. For a porous material saturated with water or some other organic solvent, there is a progressive penetration of the solid phase that takes place inside the capillary pores during freezing. This solidification happens either by homogeneous nucleation or by a progressive penetration of the liquid-solid formed previously at the inlet of the pore (Aligizaki 2006).

Low temperature calorimetry (LTC) or LT-DSC, also known as thermoporosimetry or thermoporometry, has been applied to characterize the porosity

of cementitious materials without the need of drying the sample (Bentz and Stutzman 2006; Kjeldsen and Geiker 2008; Ridi et al. 2009, 2013; Vu et al. 2010). In LTC, the basic concept is that the freezing of water is an exothermic process while melting is an endothermic process from which the ice content involved in these processes can be calculated using the heat of fusion for the confined water/ice in the freezing or melting process and the measured heat flow with respect to ice formation or melting at different temperatures.

During freezing, the ice front penetrates the largest pores first, then the progressively smaller pores with decreasing temperature. The peaks observed by a plot of heat flow versus temperature during freezing corresponds to water freezing in pores with various size entryways or pore necks. The smaller the entry way, the more the freezing peak is depressed. Therefore, the presence of, absence of, or changes in peaks can be used to infer the characteristic sizes of the percolated water-filled pores in the microstructure of hydrating cement pastes (Bentz and Stutzman 2006). Several studies have revealed characteristic peaks centered around -15^{o}C, -25^{o}C to -30^{o}C, and -45^{o}C to -50^{o}C during cooling which evolve during the hydration process (Bager and Sellevold 1986a; b; Bentz and Stutzman 2006; Kjeldsen and Geiker 2008; Ridi et al. 2009; Snyder and Bentz 2004). Snyder and Bentz (2004) adopted the naming convention of capillary pores (CP), open gel pores (OGP), and dense gel pores (DGP) for the freezing peaks centered around -15^{o}C, -25^{o}C to -30^{o}C, and -45^{o}C to -50^{o}C respectively. These three freezing temperatures correspond to pore radii of approximately 10, 6, and 4.5 nm respectively. These values are rough estimates as the freezing point depression is influenced by the ionic concentration of the pore solution

in addition to the size of the assumed cylindrical pore entryways (Bentz and Stutzman 2006; Fagerlund 1973). The first version of the Jennings Colloidal Model-I (CM-1) was used as the bases of intepretation of the LT-DSC scans by Snyder and Bentz (Ridi et al. 2009). This model is based on the idea that the bulk microstruture is formed as a consequence of the packing of basic particles (globules) having peculiar shape and internal structure (Jennings 2008; Ridi et al. 2009). The first version of the model focused on explaining how the properties of the material depend on the packing behavior of the basic globules, without exploring the influence of the globules' internal structure on the bulk properties. In the framework of the CM-I model (Figure 4.6), the peak in the region between -20 and -35 ^{o}C was assigned to water only accessible via the inter-LD pores, and the peak below -40 ^{o}C corresponds to pores inside the low-density C-S-H (LD C-S-H), whose dimension was estimated to be around 1 nm (Ridi et al. 2009).

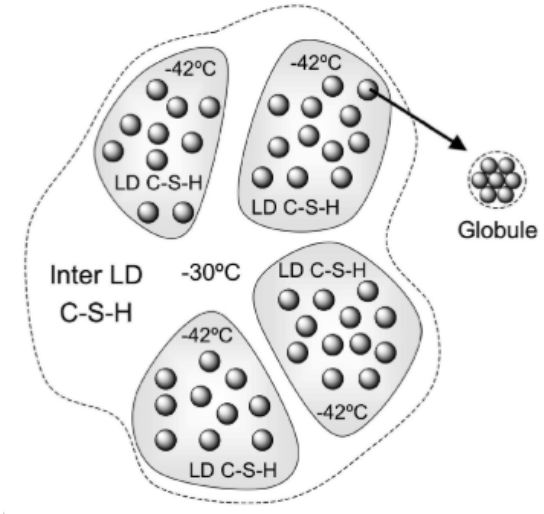

Figure 4.6 Schematic representation the Jennings Colloidal Model I (CM-I) for cement microstructure (Ridi et al. 2009)

The CM-I model was later modified to account for the smallest porosity of the C-S-H phase associated with the basic globules' internal structure (Jennings 2008). This model is known as Colloidal Model-II or CM-II. According to the CM-II model, the microstructure of a cement paste can be schematically as shown in Figure 4.7. The basic globule is a disk-like object, with a thickness of around 4 nm, having a layered internal structure. The water inside the globule is located both in the interlamellar spaces and in very small cavities (intraglobular pores, IGP), with dimensions less than 1 nm. The packing of these globules produces a porous structure, where two other main pores populations can be identified: the small gel pores (SGP), with dimensions 1-3 nm; and the large gel pores (LGP), with dimensions 3-12 nm in size (Ridi et al. 2009). The water in the intragobular pores are not detectable by LT-DSC. The open gel pores (OGP) and dense gel pores (DGP) naming convention used by Snyder and Bentz correspond to LGP and and SGP respectively.

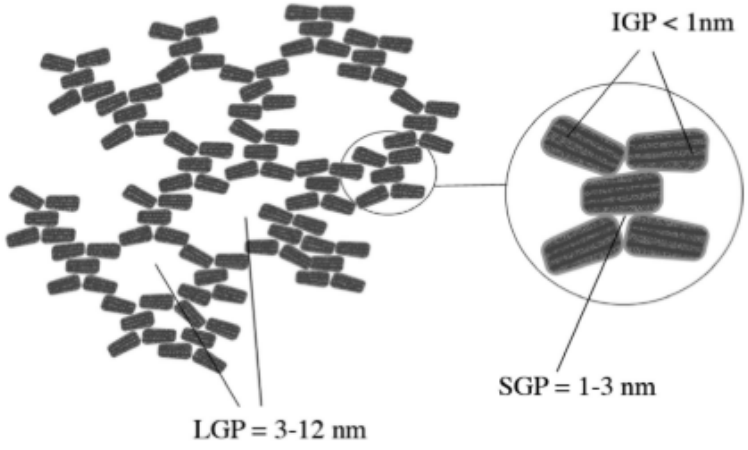

Figure 4.7 Schematic representation the Jennings Colloidal Model II (CM-II) for cement microstructure (Ridi et al. 2009)

There is only one characteristic peak or wide hump in the heating part of LTC thermograms in the freezing temperature range. This is due to the evidence that the pore size distribution in a cement paste is unimodal, and since no characteristic dimensions of the pores are present, the melting process of the ice in the pores occurs as a continuous release of heat from the ice contained in the pores with increasing dimension, thus producing only a hump during the thawing process. However, when the sample is subjected to cooling, the progressive movement of the ice front in the pores produces crystallization of the water contained in the pores. In this case, the solidification temperature will depend on the dimension of the pore entry ways, rather than the dimension of the pores (bottleneck effect) (Snyder and Bentz 2004). Hence, the characteristic freeze-thaw behavior of cement pastes, as detected by DSC, would indicate that the bulk microstructure has a unimodal pore size distribution with characteristic dimensions of the channels connecting the pores (Ridi et al. 2009).

4.1.9 X-ray Diffraction (XRD)

Powder x-ray diffraction (XRD) utilizes x-rays to investigate the structure of crystalline materials by measuring the diffraction of x-rays from the planes of atoms within the material. It can be used to measure the crystalline content of materials and identify the crystalline phases present based on their diffraction pattern. When an incident beam of monochromatic X-rays interacts with a target material, the dominant effect that occurs is the scattering of the X-rays from atoms within the target material. In crystalline materials, the scattered X-rays undergo constructive and destructive interference. The constructive interference is termed diffraction. The diffraction of X-rays by crystals is described by Bragg's Law, which relates the wavelength of the

incident X-rays to the angle of incidence and spacing between the crystal lattice places of atoms in the crystal.

$$n\lambda = 2d \sin\theta \qquad 4.6$$

where n is an integer, λ is the wavelength of the incident X-rays, d is the interplanar spacing of the crystal and θ is the incident angle. The directions of possible diffractions depend on the size and shape of the unit cell of the material, and the intensities of the diffracted waves depend on the kind and arrangement of atoms in the crystal structure. In polycrystalline or powder materials, there are many crystals in random orientations. When the incident angle is varied systematically, all possible diffraction peaks in the sample can be detected.

4.2 Test Procedures

ASTM Type I cement obtained from LaFarge was used for all the work in this study. The properties of the cement are shown in Figure 4.8.

CHEMICAL ANALYSIS

Item	Spec limit	Test Result
Rapid Method, X-Ray *(C 114)*		
SiO2 (%)	---	18.3
Al2O3 (%)	6.0 max	5.6
Fe2O3 (%)	6.0 max	2.8
CaO (%)	---	60.7
MgO (%)	6.0 max	2.7
SO3 (%)	3.0 max *	4.4
Loss on ignition (%)	3.0 max	2.5
Insoluble residue (%)	0.75 max	0.58
CO2 (%)	---	1.4
Limestone (%)	5.0 max	3.5
CaCO3 in Limestone (%)	70 min	89
Adjusted Potential Phase Composition *(C 150)*		
C3S (%)	---	51
C2S (%)	---	13
C3A (%)	---	10
C4AF (%)	--- Ma	8
C3S+4.75*C3A (%)	---	100
ASTM C 150-11 and AASHTO M 85-09 Optional Chemical Requirements:		
NaEq (%)	---	0.93

PHYSICAL ANALYSIS

Item	Spec limit	Test Result	
Air content of mortar (%) *(C 185)*	12 max	8	
Blaine Fineness (m2/kg) *(C 204)*	260 min	385	
-325 (%) *(C 430)*	---	97.1	
Autoclave expansion (%) *(C 151)*	0.80 max	0.01	
Compressive strength (MPa, [PSI]) *(C 109)*			
1 day	---		
3 days	12.0 [1740] min	26.2	3799
7 days	19.0 [2760] min	33.2	4814
28 days (Reflects previous month's data)	---	39.1	5670
Time of setting (minutes)			
Vicat Initial *(C 191)*	45 - 375	120	
Mortar Bar Expansion (%) *(C 1038)***	0.02 max	0.010	

* May exceed 3.0% SO3 maximum based on our C1038 results of <0.02% expansion at 14 days. Data available upon request.

** Current Production run not available - most recent provided

Figure 4.8 Properties of portland cement

4.2.1 Compressive Strength

In order to investigate the reactivity of the simulated fly ash samples, compressive strength tests were carried out on 2” mortar cubes according to ASTM C109 “Standard Test Method for Compressive Strength of Hydraulic Cement Mortars Using 2-in or [50 mm] Cube Specimens” (ASTM C109/C109M 2009). ASTM Type I cement and ASTM Standard Sand (ASTM C778-09 2009) were used for making the mortar cubes. The mortar was prepared with a w/b ratio of 0.4, and a fly ash replacement ratio of 20%. A control sample was prepared with no fly ash replacement. A sand to binder ratio of 2.75 was used, according to ASTM C109. Distilled water was used for the mix. No additives were added to the mortar. The mortar was mixed in an electric mixer and placed in 2” cube steel molds according to ASTM C109 specifications. The cubes were made in triplicates. The samples were

stored in a moist environmental chamber at near 100% relative humidity and 25^0C temperature for 24 hours. The samples were demolded after 24 hours and stored in a saturated lime solution until test day. The samples were tested in a compressive strength machine at 3, 7, 28 and 90 days.

Table 4.1 Mix proportion from compressive strength tests

Mix	CTRL	RFA	CC1	CC2	CC3
Cement (g)	890.00	712.00	712.00	712.00	712.00
FA (g)	0.00	178.00	178.00	178.00	178.00
Sand (g)	2447.50	1958.00	1958.00	1958.00	1958.00
Water (mL)	356.00	356.00	356.00	356.00	356.00

4.2.2 Preparations of Paste Samples

Paste samples were prepared for various experiments using the Portland cement, deionized water, and the simulated fly ash and fly ash glasses. The paste samples were prepared at w/b ratio of 0.4 and replacement factor of 20% on weight bases. The paste was prepared by following a protocol similar to (Bentz and Stutzman 2006). The batched cement and fly ash powder were mixed by hand until uniform. The mix water was first introduced into mixing container. The mixer was set to a low speed of 2500rpm for 30 secs, while the cement/fly ash mixed powder was introduced into the mixing container. The mixer was set to a high speed of 6000rpm and mixed for another 30secs. After that, there was a rest period of 150 secs, during which the sides of the mixing container were scrapped down. This was followed by another mix at 6000rpm for 30 secs. Plastic disk containers approximately 1” in diameter and

3mm thick were used to cast the paste samples. About 5g of paste was placed in each plastic disks and tapped gently to remove any air bubbles. The plastic disks were then sealed. The sealed disks were placed in an environmental chamber that was kept at a constant temperature of 21^0C. After 24 hours, the disks were opened and a few drops of deionized water was placed on top of the samples and sealed again to keep the samples in a saturated condition. The samples were stored this way until test day.

Figure 4.9 Disks for curing of paste samples

4.2.3 Stopping Hydration

The hydration of the samples were stopped using solvent exchange according to recommendations in (Zhang and Scherer 2011). On test day, the paste samples were broken into approximately 2mm pieces and stored in isopropanol for four days. They were then dried in a vacuum desiccator at room temperature for 24 hours, before being sealed in plastic bags and stored in a desiccator until test day. The hydration was not stopped for the samples for low temperature DSC. For isothermal calorimetry, the samples were prepared at the time of testing.

4.2.4 Low Temperature Differential Scanning Calorimetry

Low temperature DSC experiments were conducted on a TAQ100 DSC instrument. On test day, a small piece of the paste was broken and tested in a DSC. Hydration was not stopped in DSC samples, neither was the sample dried. This was done in order to preserve the moisture in the pores so they can be frozen. The sample was wiped clean with a microfiber cloth. About 18mg was weighed in a high precision balance and placed in a steel hermitic pan. The pan with the sample was crimped to seal it. An empty pan was also crimped to serve as a reference. The sample and reference pans were carefully placed in the instrument sample holders.

Nitrogen was used as the as the cooling gas. The sample was equilibrated at 5^0C for 5 mins, and then cooled to -50^0C at a rate of -0.5^0C/min, after which it was heated back to 0^0C at 0.5^0C/min. Rapid quenching from 25^0C to 5^0C at a rate of -10^0C/min, followed by an isotherm at 5^0C for 10min in order to obtain good thermal

stability inside the measuring cell. Quenching from 5^0C to -50C at a rate of -2C/min. Melting from -50^0C to -0.2C at a rate of 0.5C/min.

1. Equilibrate to 5°C
2. Cooling ramp from 5 to-50°C at 0.5°C/min
3. Heating ramp from -50°C to +5 at 0.5 °C/min.

4.2.5 Isothermal Calorimetry

Isothermal calorimetry was performed on fresh paste samples to study heat of hydration. Isothermal calorimetry was performed on TAM Air isothermal calorimeter. The start temperature of the instrument was set at 25C. Before the test, baseline stabilization was performed to achieve acceptable baseline slope. After the sample is placed into the instrument, it takes about 45 mins for the signals to stabilize and be correct, so the first hour or so of heat evolution is lost and not recorded by the instrument. The heat of hydration was continuously measured for 7 days.

Fresh paste samples were prepared following the same mixing protocol for the paste samples as before. About 5g of fresh paste was placed in a glass ampoule and crimped. The samples were then gently placed into the calorimeter. The second slot in the calorimetry contained a reference. The samples were run in duplicates.

Isothermal calorimetry produces graphs time versus heat of hydration. The data was normalized with respect to the amount of water. Other graphs are also shown where the normalizing parameter is cement and fly ash. Due to the baseline stabilization, the first hour after mixing was not recorded. This was deemed acceptable for fly ash reactions where it takes time for the effect of the fly ash to be observed.

4.2.6 Thermogravimetric Analysis

TGA was performed on two instruments due to equipment failure of the first instrument. The first instrument was a Perkins Elmer Pyris Diamond TG-DTA. Ceramic crucibles were used. Samples were ground into fine powder passing #200 sieve. About 10mg of the sample was placed in the pan, with an empty pan as reference. Nitrogen was used as purge gas to prevent carbonation during the test, at a flow rate of 100ml/min. The samples were heated from room temperature to 1000C at 10^0C/min. The second instrument was a TAM Air isothermal calorimeter at Turner Fairbank Federal Highway Research Lab.

About 20mg of the paste samples were ground to a fineness passing the #200 sieve. About 10-20mg of the sample was put in the sample pan and placed into the instrument for analysis. The test was run at a heating rate of 10^0C/min, under nitrogen gas flowing at a rate of 50ml/min. The hydrogen was used to provide an inert environment to minimize carbonation. Hydration in paste samples was stopped by solvent exchange. Samples were ground to sieve size passing the #200 sieve. About 50mg of sample was placed in a ceramic crucible and heated at 10^0C/m in nitrogen environment from room temperature to 1000^0C.

4.2.7 Scanning Electron Microscopy (Identification of Remaining Glass)

The degree of reaction of the fly ash was determined by scanning electron microscopy, energy dispersive spectroscopy, and multispectral image analysis. Flat polished thin samples were carefully prepared before being imaged in the SEM.

SEM/EDS was used to obtain image maps of the elemental composition of the samples. The x-ray maps were then linked mathematically to obtain multispectral images, from which the individual phases were identified, segmented, and quantified.

The samples were analyzed using the scanning electron microscope at the FabLab at the University of Maryland. The SEM is a Hitachi S-3400 variable pressure SEM, fitted with a Bruker X-Flash 4030 EDS detector.

Good sample preparation is critical for proper backscatter SEM analysis. A flat, polished cross-section is required for backscatter imaging. This is to ensure that the electron beam and sample interaction height remains constant across the sample. Typically, the sample is impregnated with epoxy, and polished with successively fine grits until the desired surface fineness is obtained. In general, the sample is vacuum impregnated with a medium to low viscosity epoxy to preserve the microstructure during cutting and polishing. After curing the epoxy, the specimen is cut using a diamond saw with a lubricant to expose the cross section. The surface damage resulting from the sawing is removed by using successively finer grades of silicon carbide paper, such as 400, 600, 1200 grit to leave a plane surface with no cutting or grinding fractures. The surface is then polished again using diamond pastes of successively finer particle size such as 6um, 3um, 1um and 0.25um to remove surface scratches and produce a mirror-like finish. The specimen is cleaned after the final polish and carbon coated for SEM imaging. Due to lack of equipment, the sample polishing was done in a commercial lab.

The SEM/EDS experiments were largely performed in the Fablab. The SEM was operated at an accelerating voltage of 15kV, which is nearly twice the x-ray

excitation energy of iron, the heaviest element for which x-ray intensity maps were collected. This 2x minimum overvoltage is suggested by (Goldstein et al. 2003). This voltage value presented an optimal number between the 2x minimum, and a value lower enough to prevent localized heating and destruction of the epoxy impregnated samples. A working distance of approximately 10mm was used.

The EDS was set up to collect high resolution element maps with size 800 x 600 pixels, at a magnification of 300x, resulting in a field of view of 423μm x 317μm per image, making the size of a pixel 0.53μm. The SEM current was measured with a Faraday cup and found to be about 4nA. The equipment was set to maintain this constant current for all samples. The EDS was operated with a dwell time of 256μs/pixel. This dwell time was used as a compromise between particle statistics and local charging effects and sample damage. Under these conditions, the x-ray count rate was approximately 30,000 cps, with a dead time of around 15%. Element maps for calcium, silicon, aluminum, iron, potassium, magnesium, sodium, and sulfur were collected. Two-line averaging was used to collect the x-ray maps. Under these conditions, it took approximately 7 mins to collect a frame. Two frames were collected for each image set. For practical reasons, about 15 image sets were collected for each sample.

After the collection of the element maps, the maps were analyzed to determine the glass phases remaining in the samples and quantify them. This was done using ImageJ and MultiSpec, both free software readily available online.

The results from the multispectral image analyses gives phase fractions in terms of area. For a flat, thin section sample, the area fractions are an estimate of the

volume fractions (Snyder and Stutzman 2013). The degree of reaction of the fly ash is given as (Haha et al. 2010):

$$Degree\ of\ FA\ reaction = \left(1 - \frac{V_{meas}}{V_{ini}}\right).100 \quad (4.7)$$

where V_{meas} is the volume fraction of fly ash glass measured by image analysis and V_{ini} is the initial volume fraction of fly ash glass in the mix proportion. The initial volume fractions were obtained from the glass replacement factor (based on mass) and the density of the glass.

$$V_{ini} = \frac{mass\ of\ fly\ ash\ glass}{density\ of\ glass} \quad (4.8)$$

4.2.8 Electron Microprobe Analysis

Microprobe analysis was performed on a Joel JXA-8900 Superprobe. The purpose was to perform quantitative analysis on the various hydrate phases present in the samples. Thin polished samples used for SEM were also used for microprobe analysis. The test was performed at a voltage of 15kV, and a current of 10nA. The voltage was selected so that it is adequate to excite the Fe-K-alpha ions, while minimizing sample damage. A beam size of 2µm x 2µm was used. Ca, Si, Al, Fe, Mg, S, Na, K, O was analyzed for each sample. For each sample, points were manually selected at various points of interest.

4.2.9 XRD

X-ray powder diffraction analysis was performed to identify and quantify the crystalline hydration phases present in the cement fly ash paste samples. XRD analyses was also performed on some of the raw glass samples to ascertain the crystalline phases present. Pure corundum was used as an internal standard to determine the relative quantities of both crystalline and amorphous phases in the samples. The XRD analysis was performed on a D8 advanced XRD equipment.

Samples for XRD were ground to fine powder passing the #325 sieve (xxx um). This was done to improve the particle statistics for quantitative analysis. About 1g of the fine powder was measured on a high precision balance. 10% by weight of 99.99% pure corundum was added as an internal standard. The internal standard and the powder were mixed thoroughly using a vortex vibrator for about 5 mins. The powdered sample was placed in a sample holder. A glass platen was used to level off the surface of the sample by applying a small vertical force. Great care was taken to prevent preferred orientation of the particles. The samples were placed in the instrument and scanned from 6^0 to 80^0 2θ.

4.2.10 Small Angle Neutron Scattering (SANS)

Due to limited availability of beam time at the NIST SANS instrument, the experiment was designed using an inverted time approach. Instead of measuring the same sample at different times during the course of the hydration reaction, this approach involved preparing multiple samples that had different starting times for hydration. They were then all measured sequentially in the SANS instrument.

Two sample sets were prepared. The early age sample (7-day) were mixed and allowed to hydrate in a 1-mm-thick quartz cell. They were hermetically sealed and kept at room temperature in a moist environment until they were tested at 7 days. Another set of samples were mixed and cast in 1" cylinder molds. They were sealed and kept in the same manner as the 7-day sample and cured for 28 and 90 days. A few days before the test date, thin coupons less than 1 mm were cut from each cylinder. SANS measurements were performed at the NIST center for Neutron Research using NG7 30-m SANS instrument with a neutron wavelength of 0.8 nm. By varying the sample-to-detector distance, data for each specimen were obtained over a magnitude range of scattering vector of $0.02<q<3\ nm^{-1}$, where $q=4\pi\sin(2\theta)/\lambda$, 2θ is the scattering angle of vector and λ is the neutron wavelength.

Chapter 5: Results and Discussions

5.1 Isothermal Calorimetry (Kinetics of Hydration)

Figure 5.1 shows the heat flow curves for the hydration of cement and the synthetic fly ash glasses. The heat flow is normalized to the mass of cement. In all the mixes, the first one hour is not recorded due to mixing outside the calorimeter and the time it takes for the signal to stabilize in the calorimeter. The curves therefore show the start of the acceleration period.

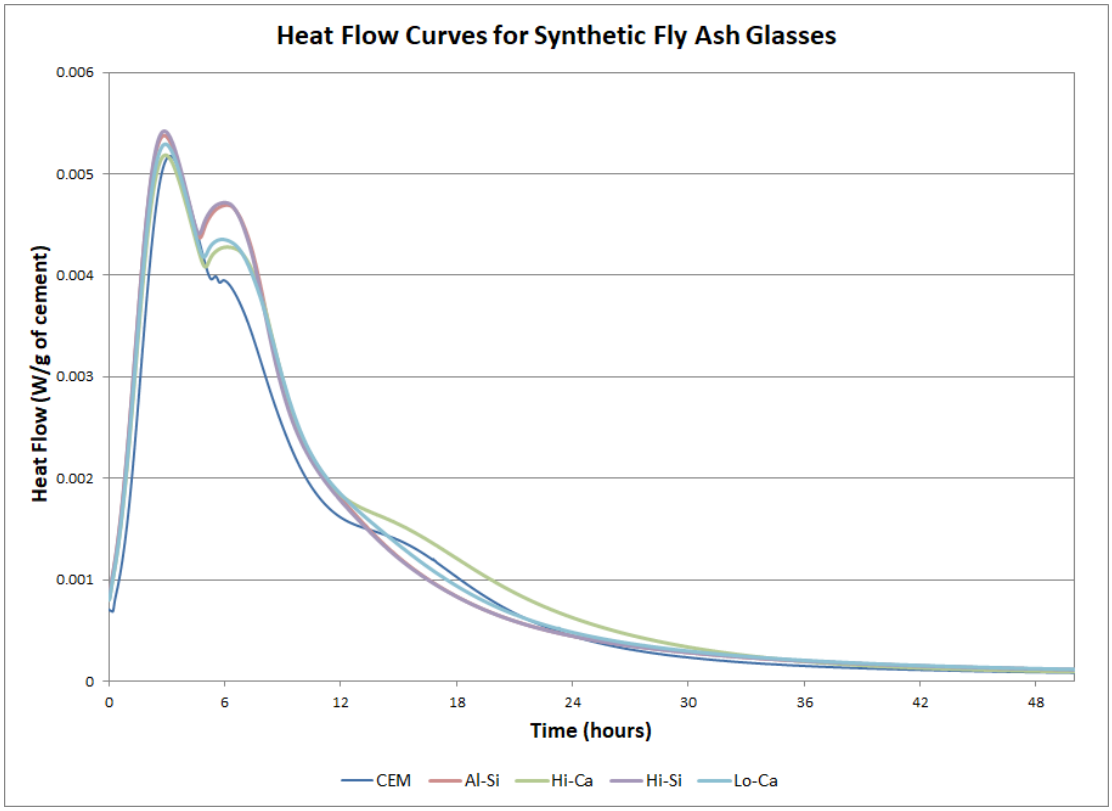

Figure 5.1 Heat flow curves for hydration of cement and synthetic fly ash glasses (normalized to mass of cement)

The acceleration period is associated with the accelerated formation rate of C-S-H due to the reaction of alite (C_3S). For the first 6 hours, the curves for the cement

and synthetic fly ash glass blends are identical, confirming that the reaction of the glasses themselves is not occurring at these early stages. When normalized to the mass of cement, it can be observed that the fly ash glasses enhance the reaction of the cement, resulting in higher peak intensities (Figure 5.1). This is due to the filler effect. When fly ash particles substitute cement or clinker particles, there is relatively more space available for the hydrates of the clinker phases to form in. The surfaces of the fly ash particles also act as nucleation sites for the heterogeneous nucleation and growth of hydrates. There are two broad shoulders associated with the deceleration period. The first shoulder, right after the alite hydration peak around the 6 to 10 hours range, is due to the renewed reaction of C_3A and the formation of ettringite and other AFt phases. Due to the retardation of C_3A by sulphate (gypsum), this peak is formed after the alite peak when the sulfate is exhausted, leading to the acceleration of C_3A reaction (Scrivener et al. 2015a). This leads to the formation of ettringite (AFt) phases. The second low broad peak around 16 hours is due to the formation of calcium monosulfoaluminate ("monosulfo" or AFm) from C_3A and ettringite due to the destabilization of ettringite. This broad peak may not be visible in typical cements. The enhanced shoulder peak of the C_3A reaction by SCMs has been attributed to the reaction of the SCMs themselves by some researchers (Kadri et al. 2010). However, other researchers have shown that this enhancement can occur in the presence of inert quartz as well as slag, and that even though the intensity of the shoulder peak was enhanced in the presence of slag, the heat evolved could all be accounted for by the amount of C_3A reacting (Scrivener et al. 2015a). (Quennoz and Scrivener 2013) also showed the height of this peak increased just by increasing the

water to cement ratio. Therefore, the dilution effect of fillers and SCMs may be a factor in this peak enhancement. The fineness of the SCM is also a factor impacting this peak through the provision of more surface for nucleation of hydrates. The Al-Si and Hi-Si have more enhancements of the C_3A peak than the Lo-Ca and Hi-Ca glasses. This could be due to the physical effects of the slight differences in their particle size distributions. The AFm peak is more enhanced in the Hi-Ca glass than the other glass. This could be due to the higher calcium content in the Hi-Ca, which provides a source of calcium for the formation of AFm from C_3A and ettringite.

The blended pastes also lead to a retardation in the hydration compared to the pure cement paste, evident in the shift of the deceleration curve of the blended pastes to the right. However, there is very little difference in the lag time for the blended pastes. This could be due to the lower replacement ratio (20%) and the similarity in the particle size distribution of the fly ash glasses.

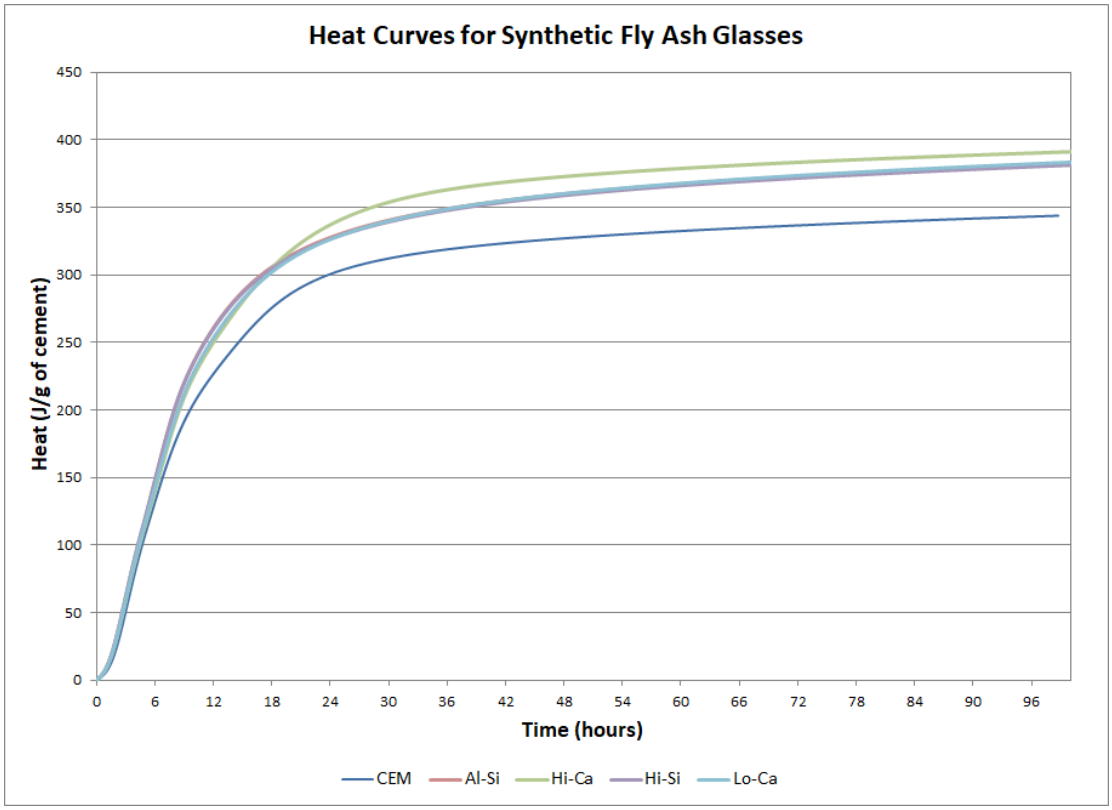

Figure 5.2 Cumulative heat flow curves for hydration of cement and synthetic fly ash glasses (normalized to mass of cement)

The total heat of hydration (Figure 5.2) also illustrates the filler effect of the fly ash. Lo-Ca has higher cumulative heat, perhaps due to the reaction of Ca. The rest of the fly ash glasses are identical. The total heat is the result of several chemical reactions happening at the same time. For the simulated fly ash, they are also the result of the contributions of the various glasses.

The dilution effect is made evident when the heat flow curves are normalized with respect to mass of water or mass of binder (cement plus fly ash) as shown in Figure 5.3 to Figure 5.6. The peaks for the blended pastes have lower intensities due to the dilution effect of the fly ash. Because the fly ash is not reactive at early days, the relatively lower content of the more reactive cement leads to lower hydration heat

intensities. This illustrates the competing effects of the filler effect and the dilution effect in the overall performance of SCMs.

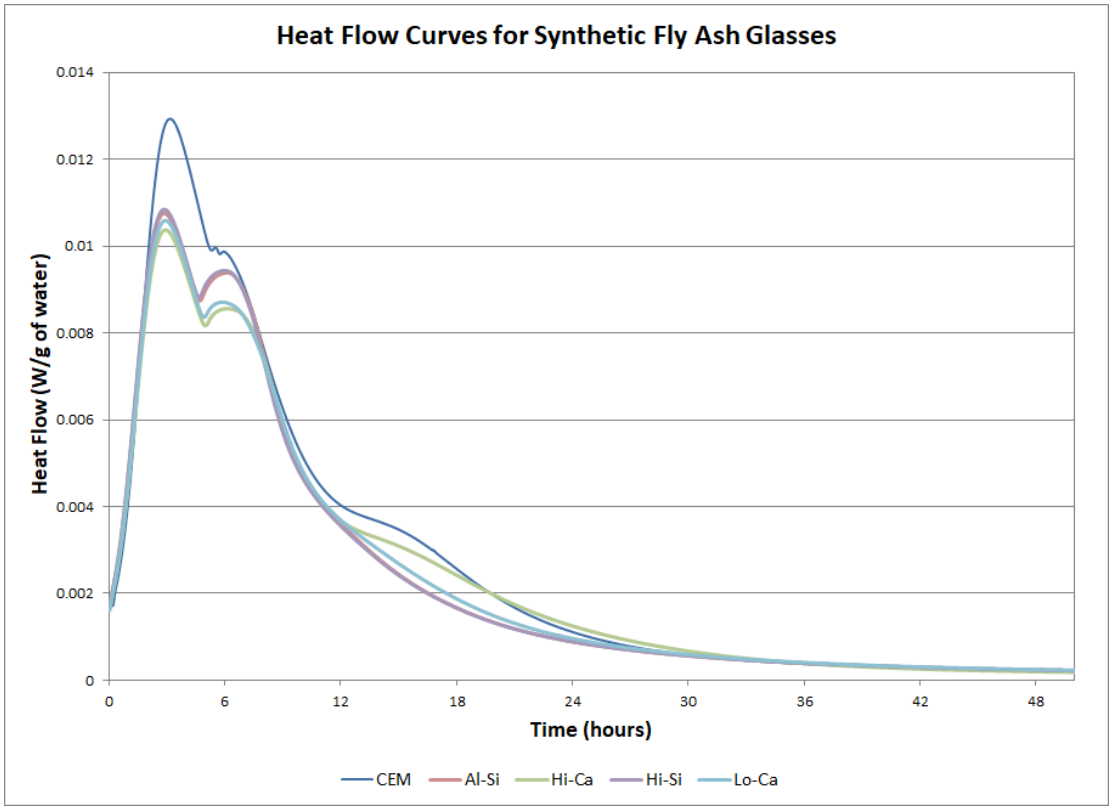

Figure 5.3 Heat flow curves for hydration of cement and synthetic fly ash glasses (normalized to mass of water)

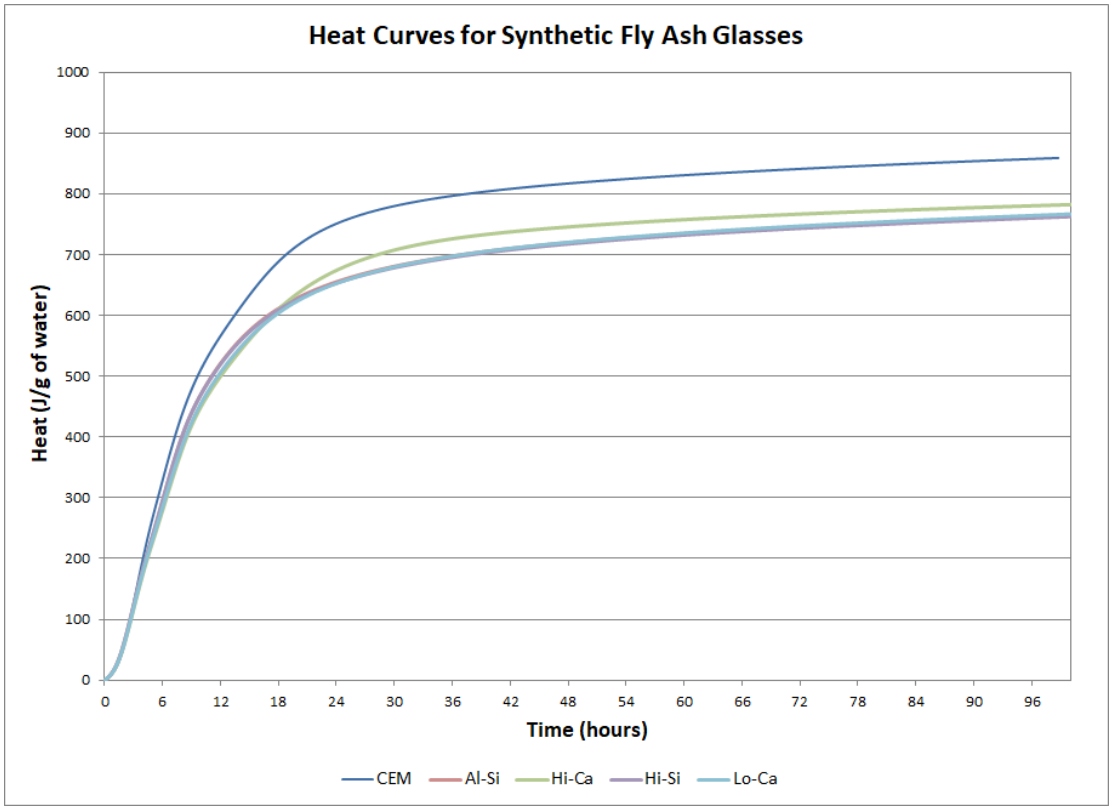

Figure 5.4 Cumulative heat flow curves for hydration of cement and synthetic fly ash glasses (normalized to mass of water)

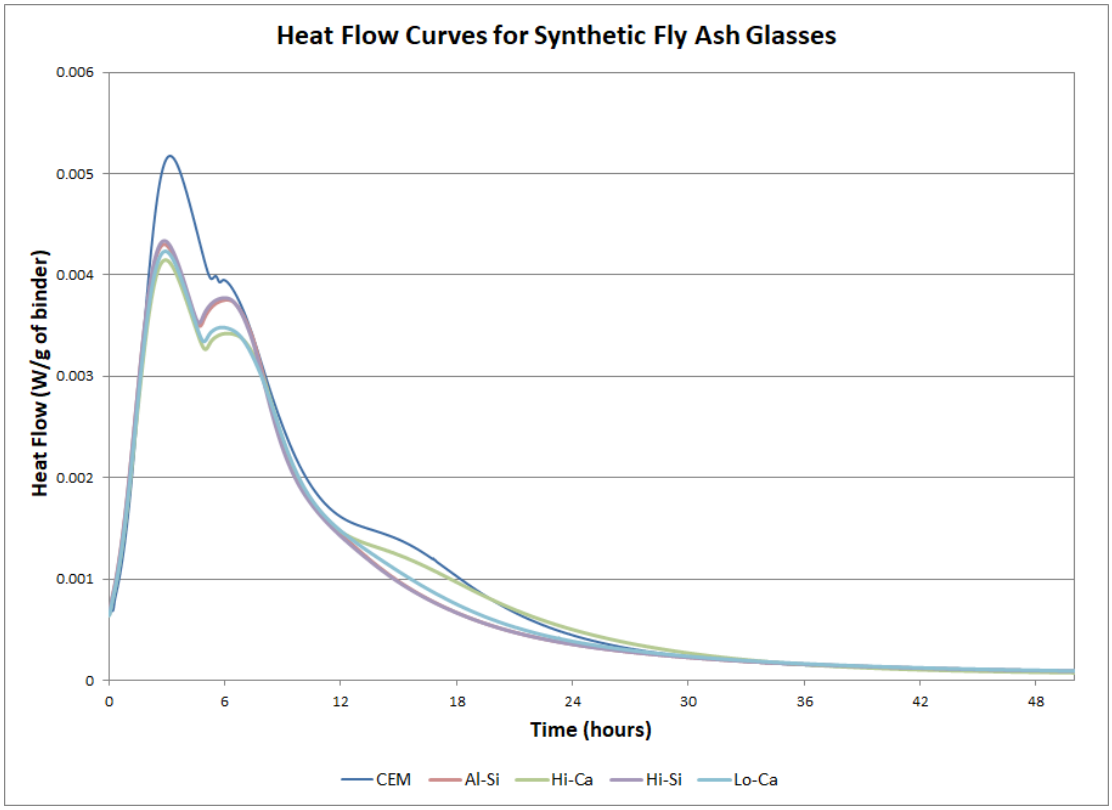

Figure 5.5 Heat flow curves for hydration of cement and synthetic fly ash glasses (normalized to mass of binder)

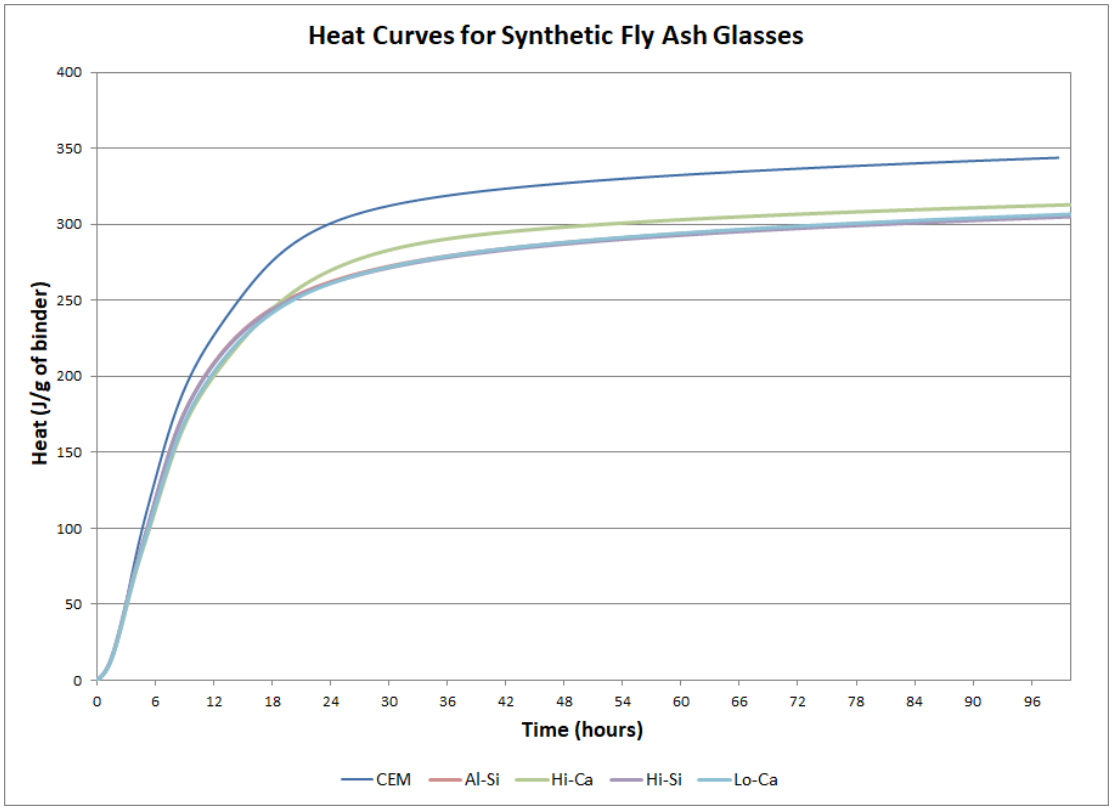

Figure 5.6 Cumulative heat flow curves for hydration of cement and synthetic fly ash glasses (normalized to mass of binder)

Similar calorimetry experiments were conducted with the simulated fly ashes. The filler effect on the hydration peaks is similar to that observed with the individual glasses. The simulated fly ashes enhance the hydration peaks due to the filler effect (Figure 5.7). The fly ashes also retard the onset of the deceleration period. The synergistic effect of the various glasses appears to even out the differences in the individual glasses. The cumulative heat flow curves also show the enhancement of the hydration curves due to filler effect (Figure 5.8). The dilution effect is also evident when the curves are normalized to the mass of water (Figure 5.9).

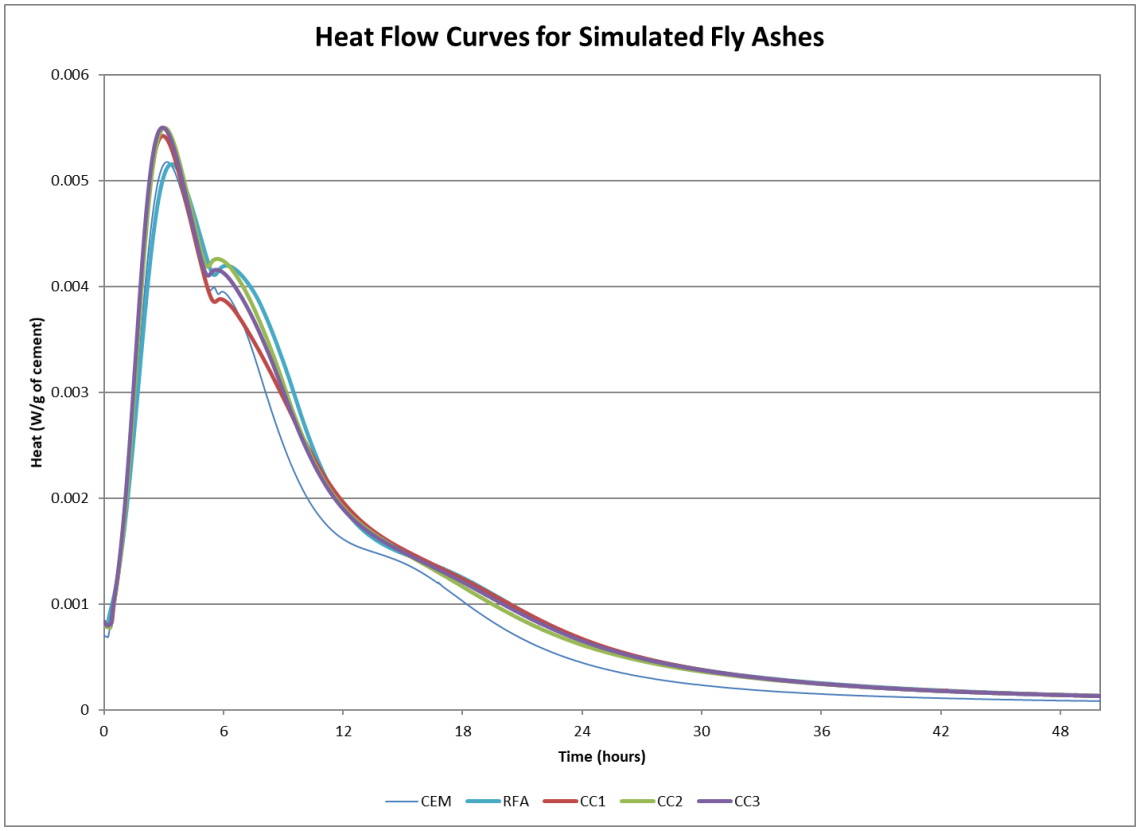

Figure 5.7 Heat flow curves for hydration of cement and simulated fly ashes (normalized to mass of cement)

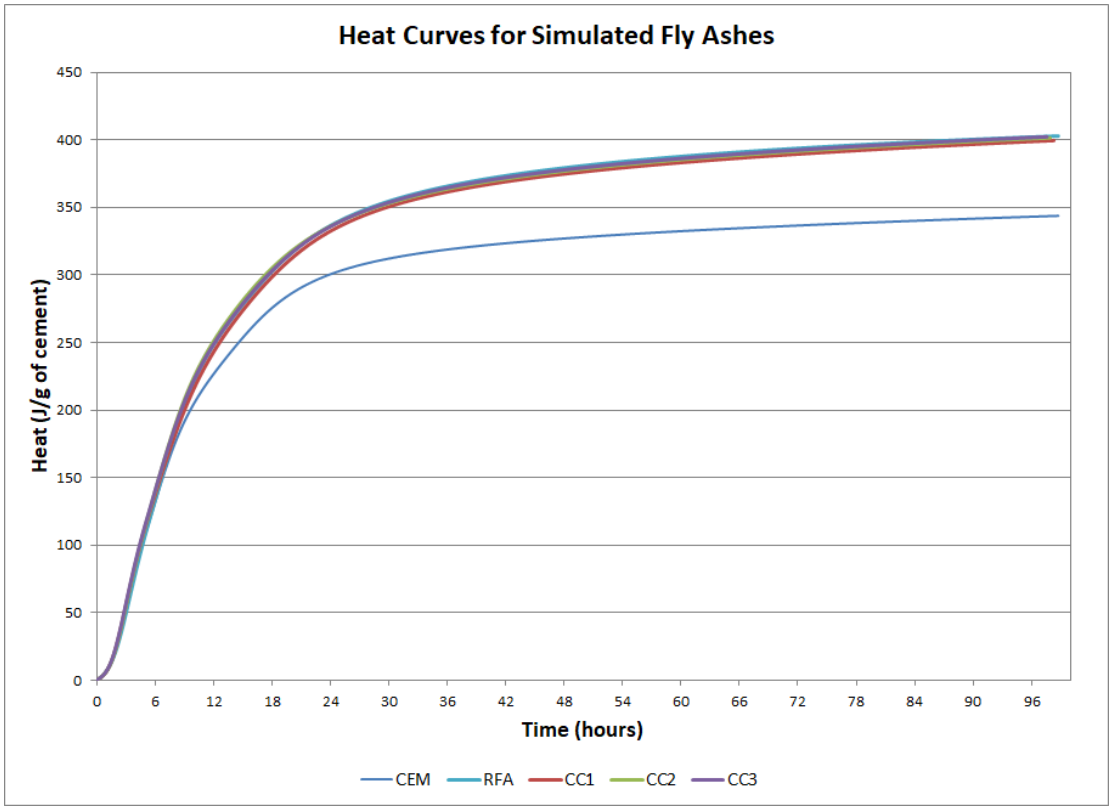

Figure 5.8 Cumulative heat flow curves for hydration of cement and simulated fly ashes (normalized to mass of cement)

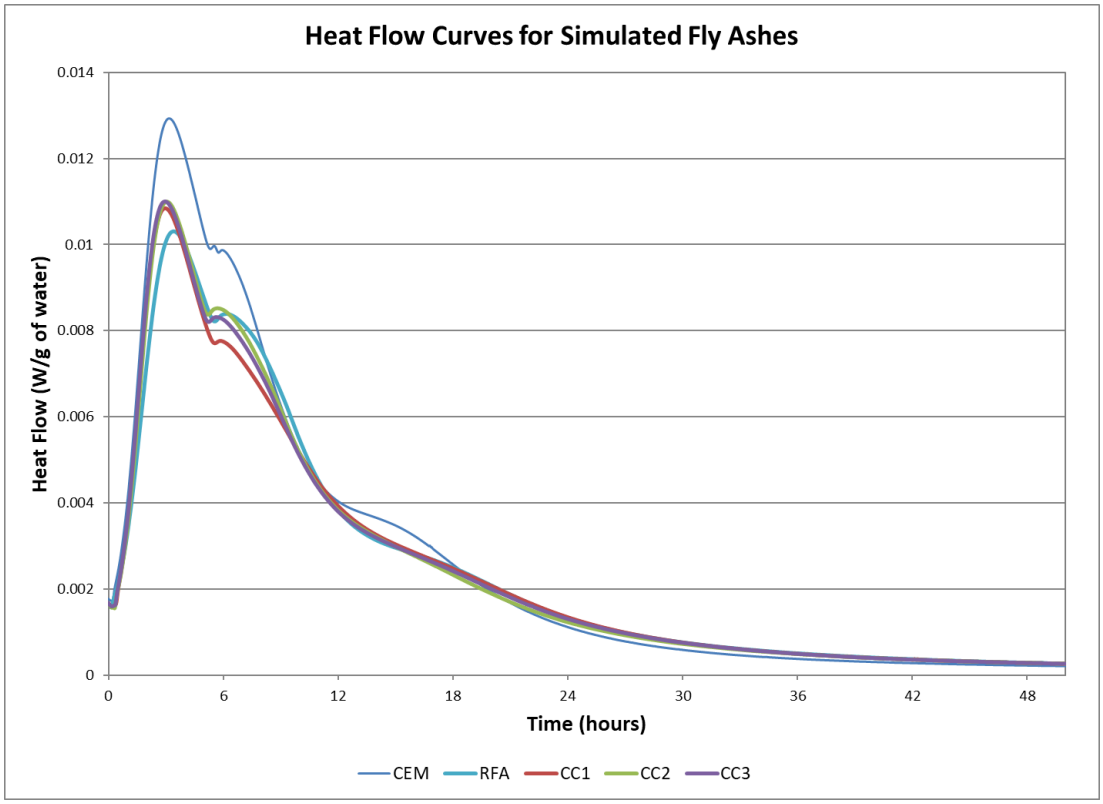

Figure 5.9 Heat flow curves for hydration of cement and simulated fly ashes (normalized to mass of water)

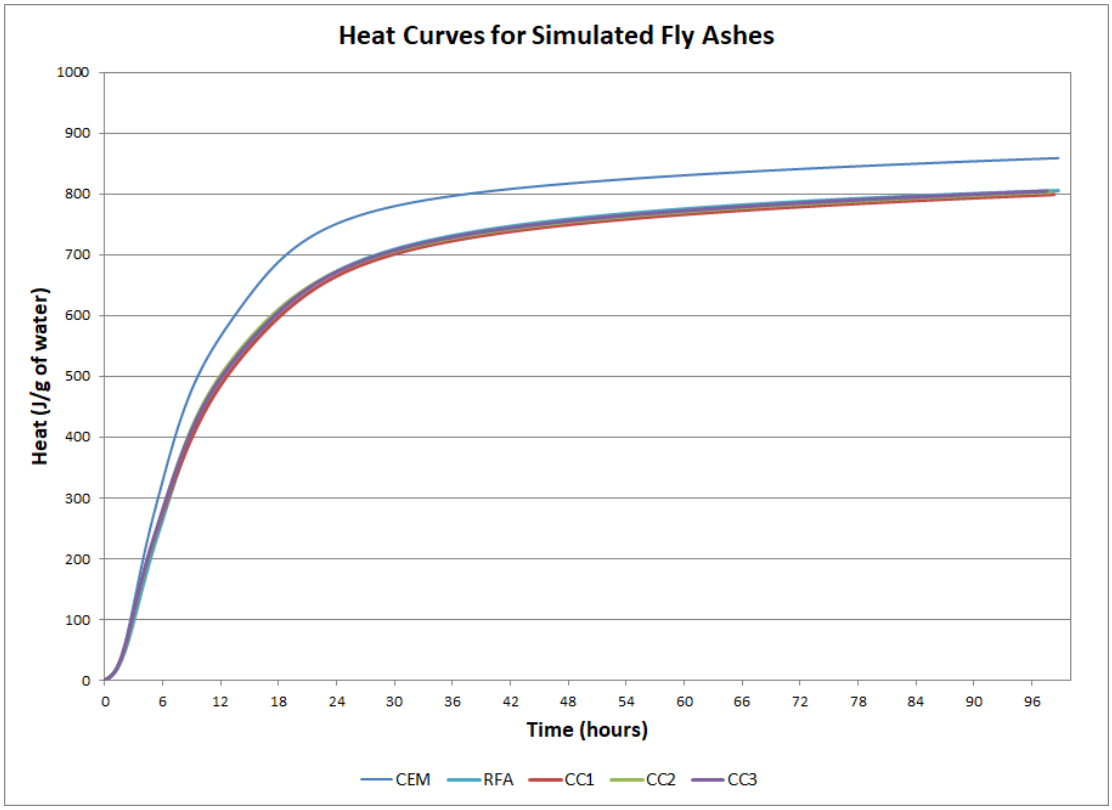

Figure 5.10 Cumulative heat flow curves for hydration of cement and simulated fly ashes (normalized to mass of water)

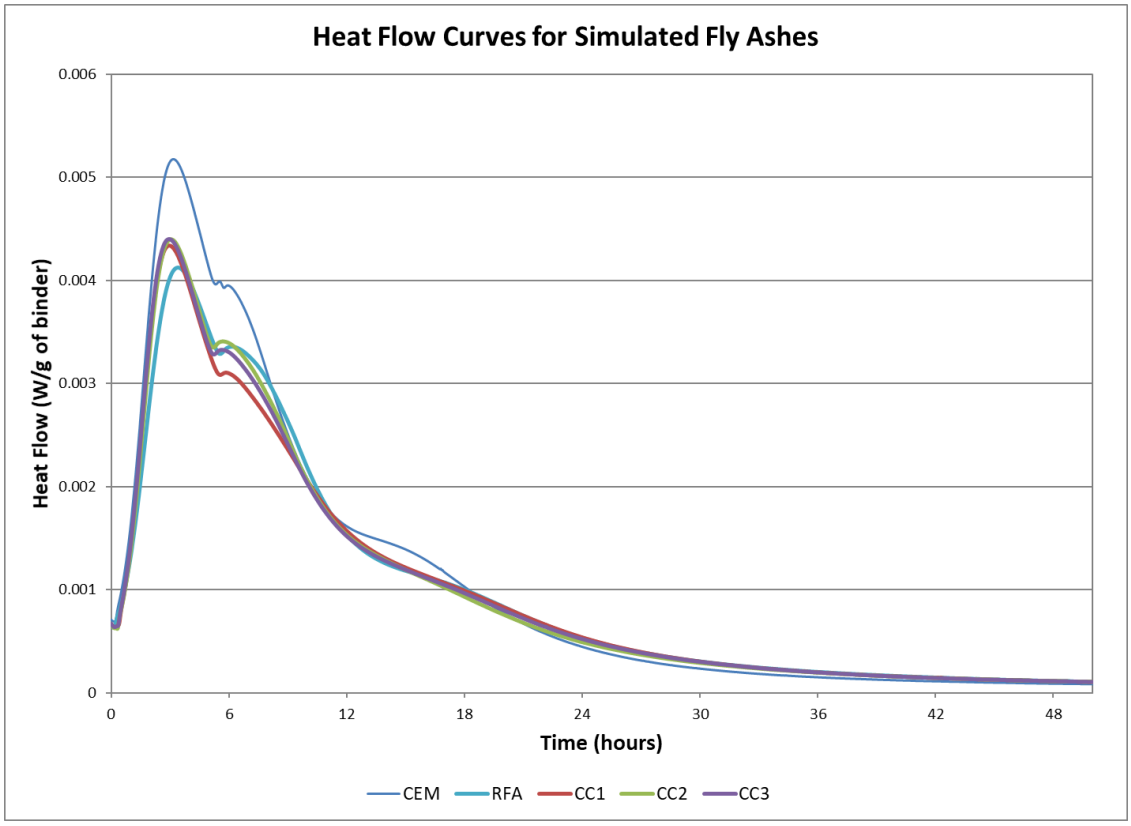

Figure 5.11 Cumulative heat flow curves for hydration of cement and simulated fly ashes (normalized to mass of binder)

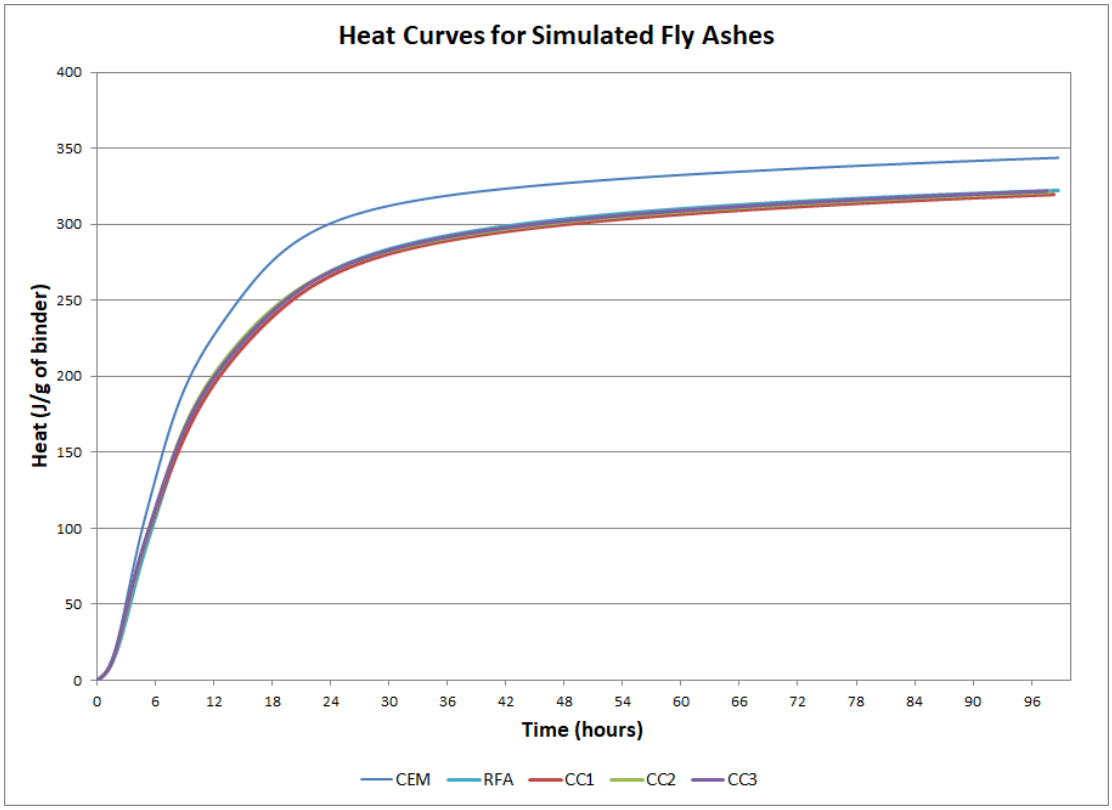

Figure 5.12 Cumulative heat flow curves for hydration of cement and simulated fly ashes (normalized to mass of binder)

Table 5.1 shows the cumulative values of the heat of hydration curves of the various samples. Based on the total heat of hydration at 7 days, the HiCa glass appears to be the most reactive, while the CC3 fly ash appears to be the most reactive simulated fly ash.

Table 5.1 Cumulative values of the heat of hydration curves

Sample	Total Heat Emission Q (mW/g)				
	12 h	24h	48h	72 h	7 d
Cement	6616	10347	12922	13500	14302
RFA	5430	9079	11719	12480	13412
CC1	5474	8938	11588	12342	13309
CC2	5649	9184	11672	12411	13375
CC3	5632	9160	11691	12442	13405
AlSi	6010	9426	11270	11864	12717
HiSi	6036	9396	11234	11830	12680
HiCa	5673	9145	11703	12316	13014
LoCa	5769	9218	11251	11870	12749

5.2 Low-Temperature Calorimetry

Low-temperature calorimetry was performed on the samples in order to study the evolution of the pore structure with time. Each peak corresponds to water freezing in a set of pores with an entryway pore diameter determined by the freezing point depression (Bentz and Stutzman 2006; Fagerlund 1973).

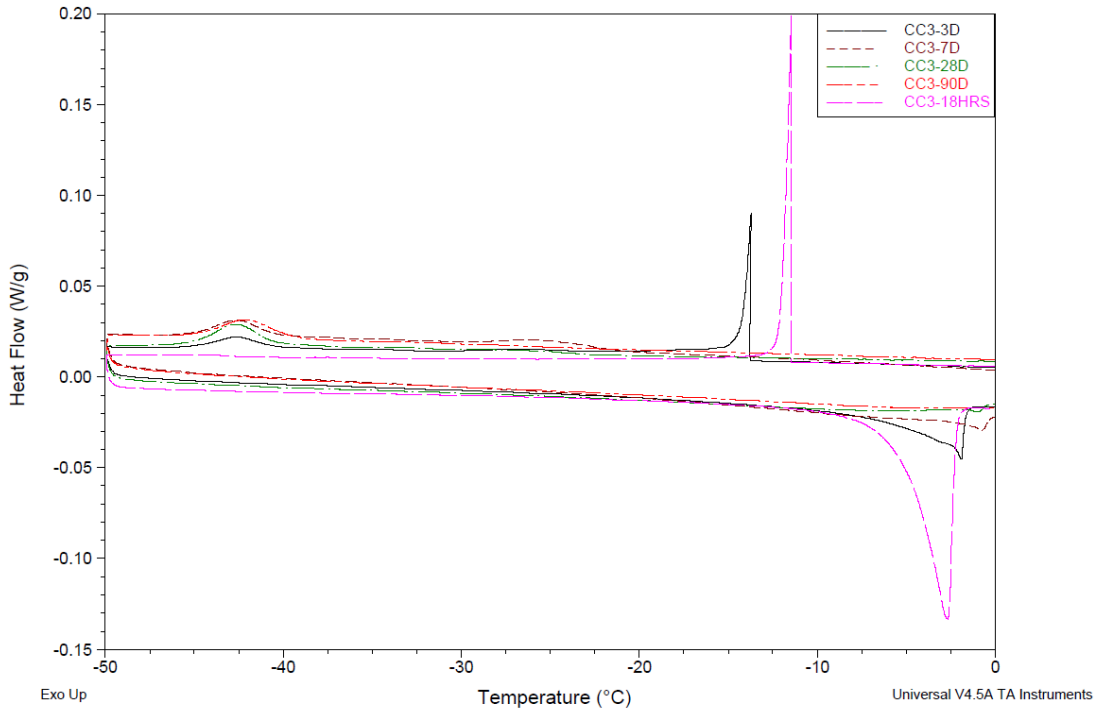

Figure 5.13 Low-temperature calorimetry scans for CC3 blended paste at 18 hours, 3, 7, 28 and 90 days of hydration

The porosity or pore sizes cluster around certain peaks and reduce progressively with time. An example of the LTC scans is shown in Figure 5.13 for the CC3 sample. Scans were performed at 18 hours, 3, 7, 28 and 90 days to illustrate the evolution of the pore structure with time. At the earliest ages of 18 hours and 3 days, the dominant feature in the LTC scans is the large peak around -15ºC corresponding to percolated capillary pores. At 7 days and later, the open gel and dense gel connected pore structures form at the expense of the capillary pores, and the capillary peak can no longer be observed, suggesting that the capillary pore entryways are being filled by gel hydration products as the hydration progresses, consistent with findings by (Bentz and Stutzman 2006). The large open gel porosity peak gradually decreases with time (becomes depercolated), converting over to the dense gel pore

structure, as the pore entryways are gradually filled by dense gel instead of open gel hydration products. The heating curve also shows a gradual decrease of the peak with time, indicating a reduction in the porosity. The pore structure gradually shifts from capillary to open gel to dense gel pore.

The LT-DSC measurements are used as a qualitative tool to assess the evolution of the pore structure. Quantitative cryoporometry, which relies on the melting scan, can be used to estimate the pore size distribution using the Gibbs–Thomson equation. However, quantitative cryoporometry of cement-based materials is based on questionable assumptions (Kjeldsen and Geiker 2008), and as such, the melting scans are only presented here for illustrative purposes.

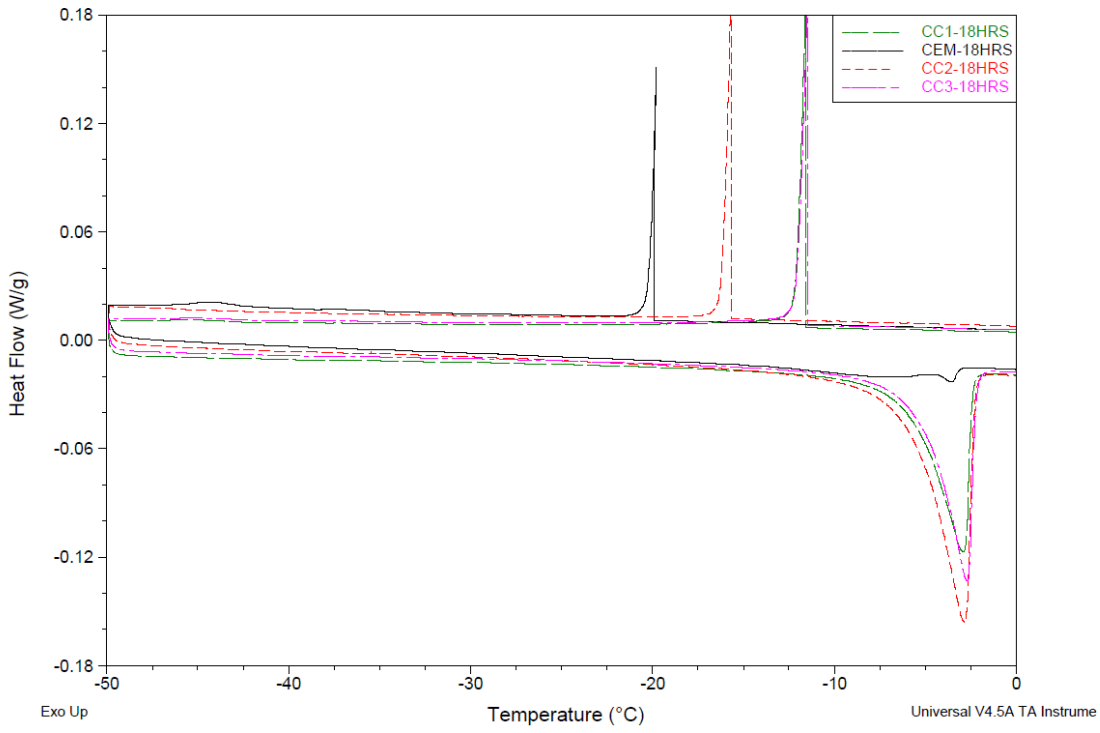

Figure 5.14 Low-temperature calorimetry scans for CEM, CC1, CC2 and CC3 at 18 hours of hydration

Figure 5.14 shows the LTC scans for CEM, CC1, CC2 and CC3 at 18 hours of hydration. At 18 hours, the capillary porosity peaks are the dominant peaks. The capillary peaks for the blended samples appear larger than the neat cement paste sample. This could be due to the unreactive fly ash particles creating a coarser capillary network in the paste. The dense gel pore peak around -45^0C is also visible for the CEM sample while barely visible in the blended fly ash samples. This indicates that even at 18 hours, there are relatively more hydration products being formed in the CEM sample than the blended samples. At 3 days, the fly ash samples show capillary peaks but not the neat cement sample (Figure 5.15). This could be due to the slow hydration of fly ash which creates coarse capillary pores that are percolated by water and thus detectable in the DSC.

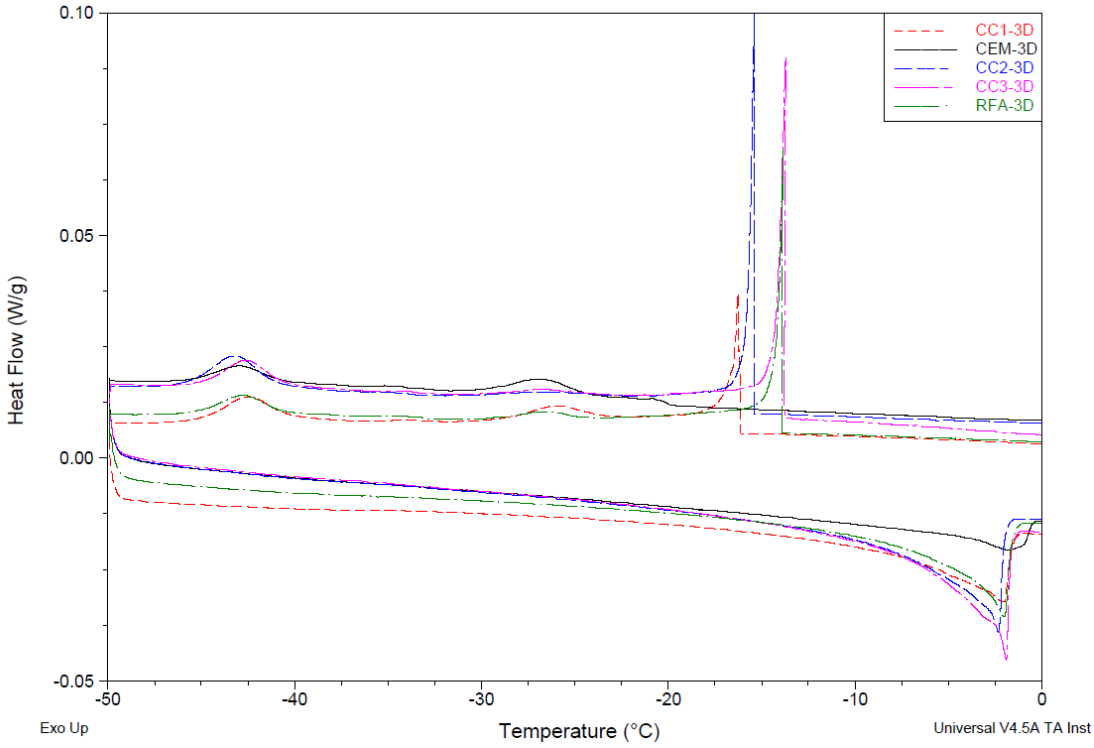

Figure 5.15 Low-temperature calorimetry scans for CEM, RFA, CC1, CC2 and CC3 at 3 days of hydration

At 7 days, the capillary peaks are not visible in any of the samples, indicating that the capillary porosity is being filled with hydration products (Figure 5.16). The open and dense gel pores begin to be more prominent in the scans. At 28 days, the OGP peaks are barely visible, only forming a broad hump (Figure 5.17). At 90 days, the dominant peak is the dense gel pore peak, indicating water freezing in the gel pores of the hydrates (Figure 5.18).

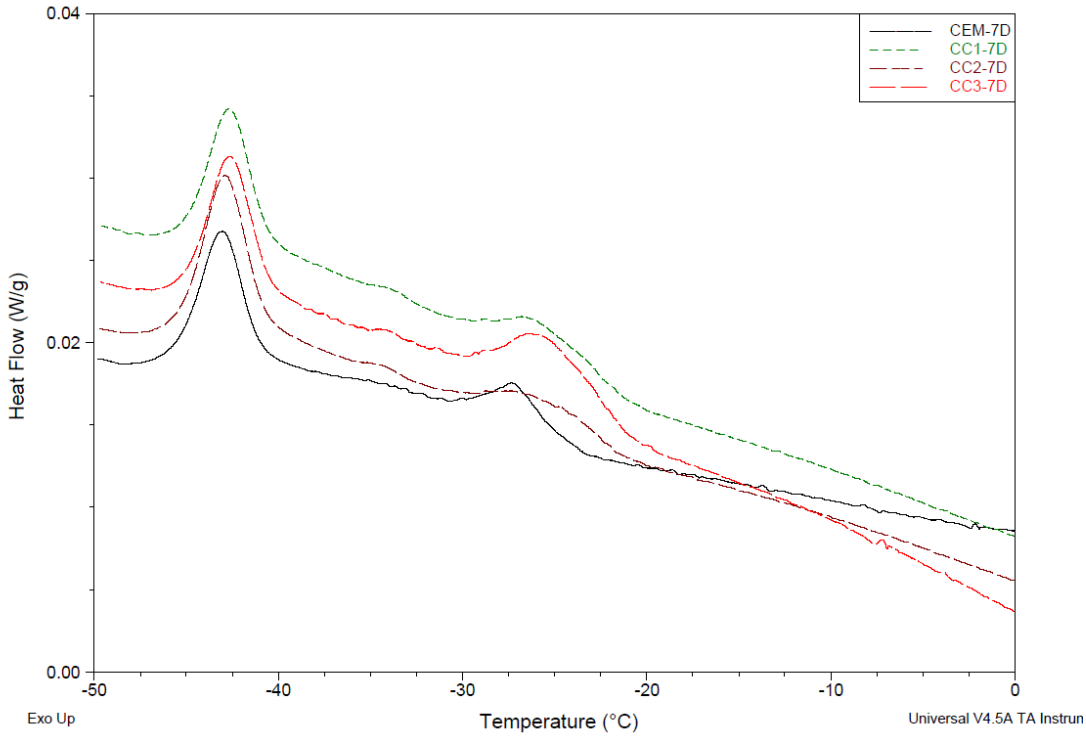

Figure 5.16 Low-temperature calorimetry scans for CEM, CC1, CC2 and CC3 at 7 days of hydration

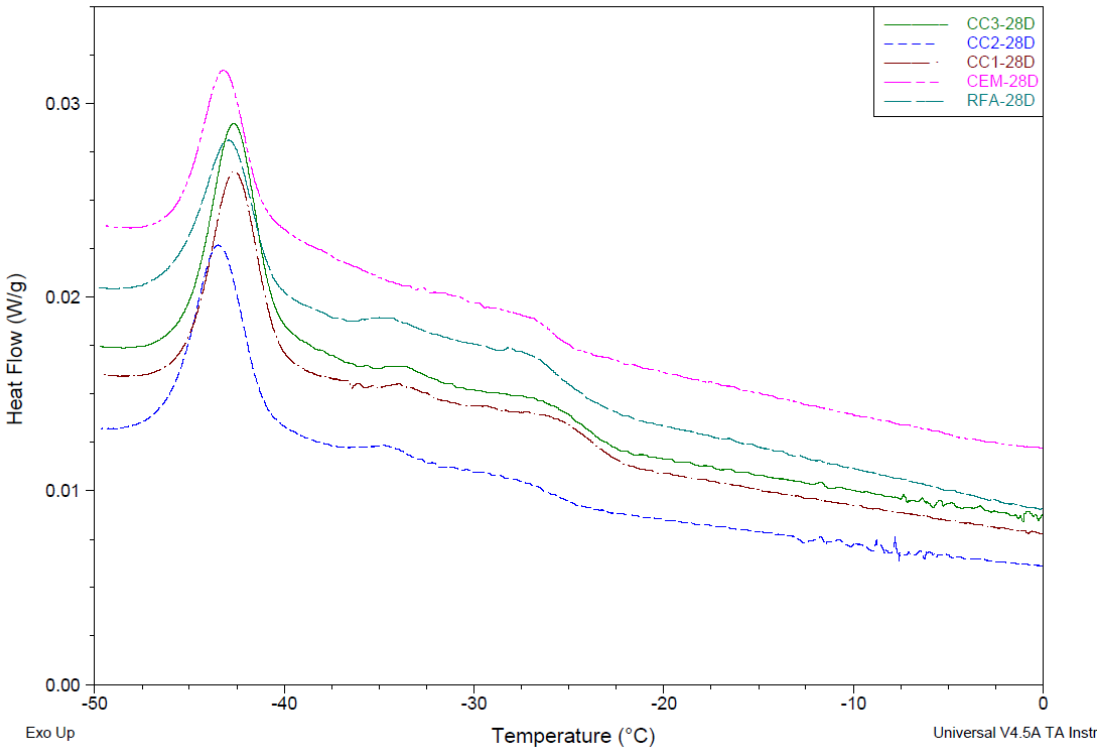

Figure 5.17 Low-temperature calorimetry scans for CEM, RFA, CC1, CC2 and CC3 at 28 days of hydration

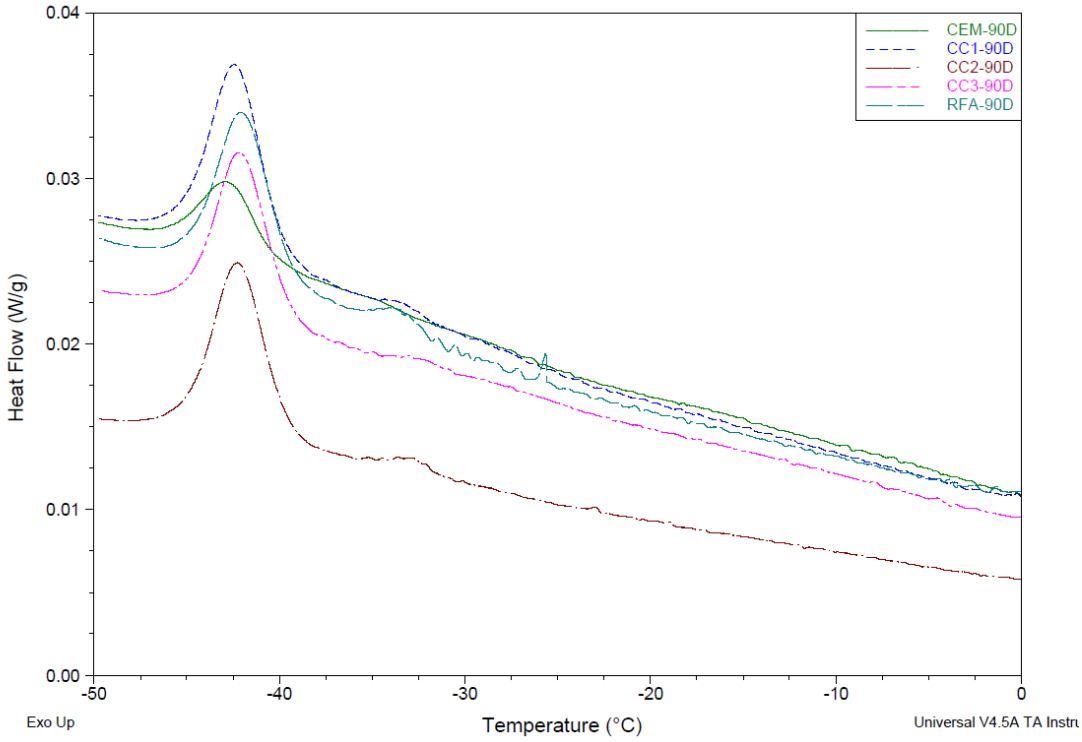

Figure 5.18 Low-temperature calorimetry scans for CEM, RFA, CC1, CC2 and CC3 at 90 days of hydration

Table 5.2 shows the estimated areas under the various peaks. Though an approximation, they indicate the evolution of the microstructure with time. As the hydration reaction proceeds, the pore structure gradually shifts from capillary to open gel to dense gel pore. The water confined in the capillary pores are consumed first, followed by the water confined in the open gel pores. The water in the dense gel pores is also consumed with time as more C-S-H is formed, leading to more water being trapped in the intraglobular layers of the C-S-H, where they are not detectable by LT-DSC. This could explain the lower peak intensity of the dense gel pore peak for the neat cement paste sample at 90 days compared to 28 days.

Table 5.2 Area under the peak for capillary porosity, open, and dense gel pores

	Area Under Peak (J/g)											
	3 days			7 days			28 Days			90 Days		
	CP	OGP	DGP	CP	OGP	DGP	CP	LGP	DGP	CP	OGP	DGP
CEM	0	1.469	1.396	0	1.089	3.078	0	0.479	3.687	0	0	2.35
RFA	3.168	0.443	1.495	-	-	-	0	1.373	3.674	0	0	4.28
CC1	2.142	1.132	2.09	0	1.455	3.14	0	1.232	4.342	0	0	4.79
CC2	4.612	0.135	2.551	0	1.143	3.791	0	0.513	4.121	0	0	4.52
CC3	4.125	0.324	1.952	0	2.452	3.293	0	1.106	4.807	0	0	4.39

5.3 TGA Analysis

Thermal analysis was performed on the samples to estimate the bound water content as an indirect measure of the degree of hydration. The tests were performed on the simulated fly ashes and the synthetic glasses. The figures below show the TG/DTG curves of the various samples for various days.

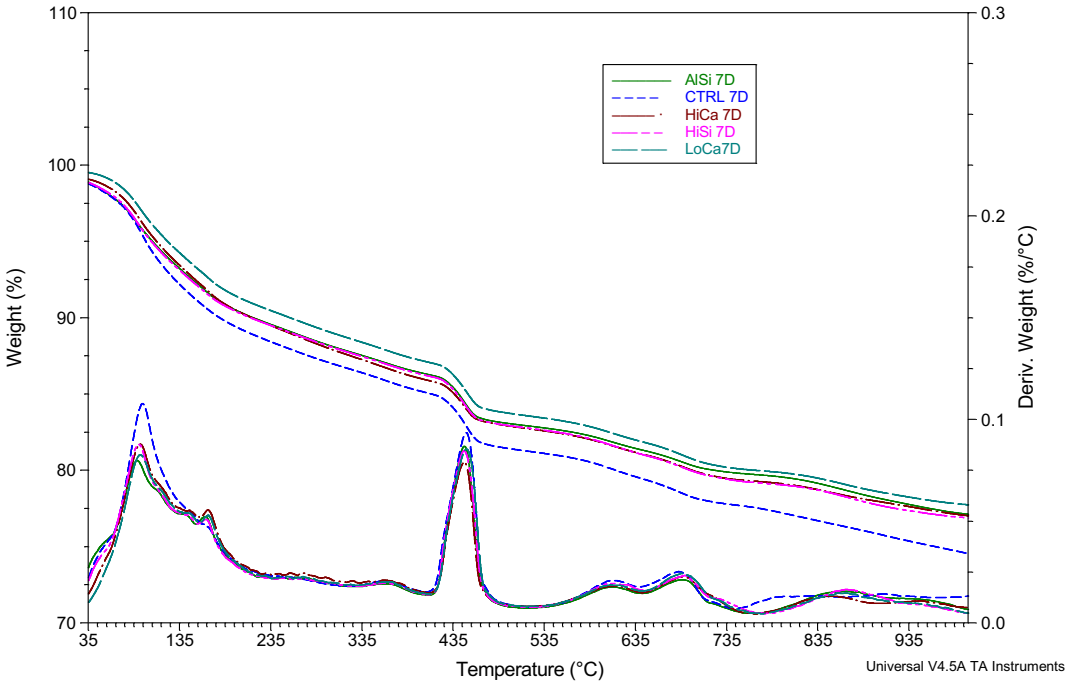

Figure 5.19 TG/DTG curves for synthetic fly ash glasses at 7 days of hydration

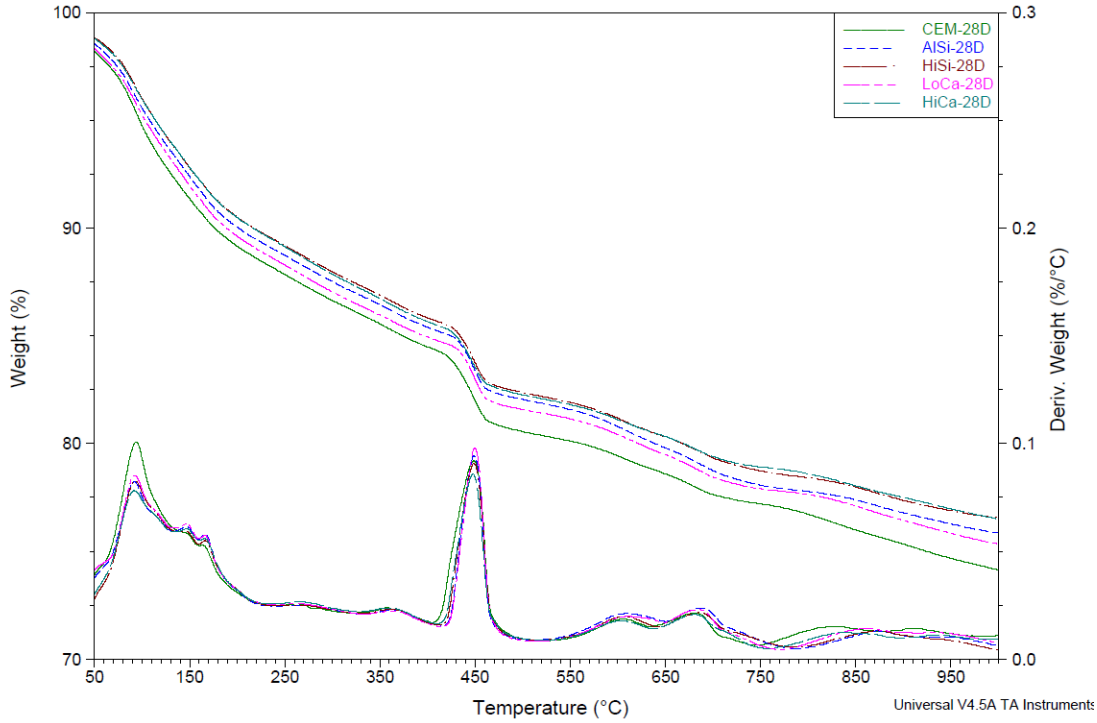

Figure 5.20 TG/DTG curves for synthetic fly ash glasses at 28 days of hydration

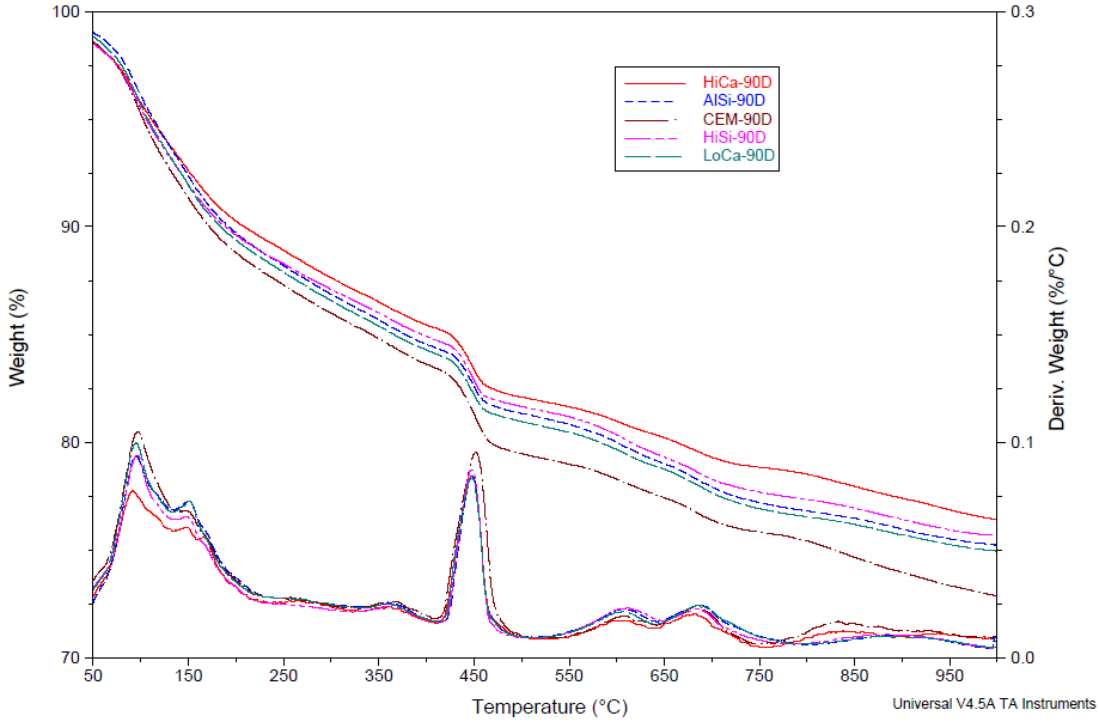

Figure 5.21 TG/DTG curves for synthetic fly ash glasses at 90 days of hydration

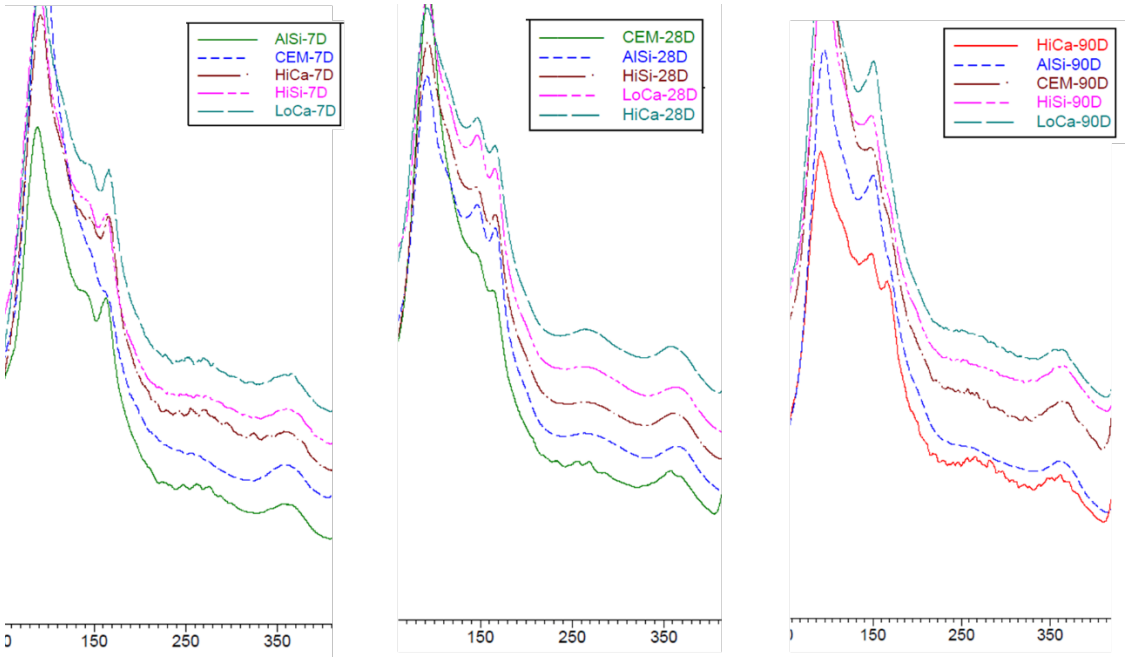

Figure 5.22 DTG curves for synthetic fly ash glasses showing AFm phases

A blow up of the DTG curves in the 50ºC to 400ºC temperature range shows the effect of the fly ash glass on the cement paste. The peaks for the AFm phases around the 160ºC temperature range are more pronounced for the blended pastes than the neat cement pastes. This is consistent with the isothermal calorimetry results where the peaks for the aluminate hydrates were more pronounced in the blended pastes than the neat cement paste. This peak in isothermal calorimetry is attributed to the excess tricalcium aluminate and replacement of tricalcium sulphoaluminate phase (AFt) by mononsulphoaluminate (AFm) or renewed formation of AFt (Baert et al. 2008). As fly ash contains significant quantities of alumina but little sulfate, fly ash in Portland cement results in a decrease in ettringite and an increase in AFm content (Lothenbach et al. 2011). The reaction of fly also provides additional alumina that lowers the sulphate to alumina ratio of the bulk paste, which promotes the conversion

of ettringite to monosulphate (Deschner et al. 2012). The Hi-Ca glass appears to form monocarbonate at 90 days. This could be due to the provision of excess calcium and alumina to form monocarbonate. When aluminum is incorporated into C-S-H, C-A-S-H, a C-S-H with tobermorite-like structure is formed (Lothenbach et al. 2011). The alumina in fly ash also reacts with CH to form stratlingite or gehlenite hydrate and hydrogarnet, and calcium aluminate hydrate, ettringite, calcium monosulfoaluminate, and calcium carboaluminate (Thomas 2013).

The chemically bound water was used as an indirect measure of the degree of hydration. The chemically bound water was calculated according to Equation 4.1. The results are presented in Table 5.3. It can be observed that the Ldh increases with hydration time, which is consistent with what has been reported in the literature. The table shows the bound water calculations. The degree of hydration was not computed for the bound water analysis because the long-term calculation using 0.24 is not justified for SCMs.

Table 5.3 Chemically bound water in mixes with synthetic fly ash glass

Sample	Age (days)	Ldh (%)	Ldx (%)	Ldc (%)	Wb (%)
CEM	7	9.63	3.36	7.07	15.88 (0.165)
	28	10.33	3.46	6.67	16.52 (0.154)
	90	11.66	3.61	6.91	18.11 (0.176)
HiCa	7	9.76	2.72	6.07	14.97 (0.134)
	28	10.41	2.94	6.01	15.81 (0.129)
	90	10.38	2.89	5.96	15.72 (0.127)
LoCa	7	9.31	3.08	6.20	14.94 (0.128)
	28	10.38	2.94	6.46	15.96 (0.133)
	90	11.42	2.85	6.26	16.84 (0.160)
AlSi	7	9.02	3.02	6.08	14.53 (0.118)
	28	10.26	2.92	6.42	15.81 (0.127)
	90	11.59	2.74	6.40	16.96 (0.149)
HiSi	7	9.03	3.00	6.24	14.59 (0.127)
	28	10.24	3.03	6.06	15.75 (0.131)
	90	10.61	2.81	6.24	15.98 (0.150)

TGA analyses on the simulated fly ashes show similar results to that of the synthetic fly ash glasses.

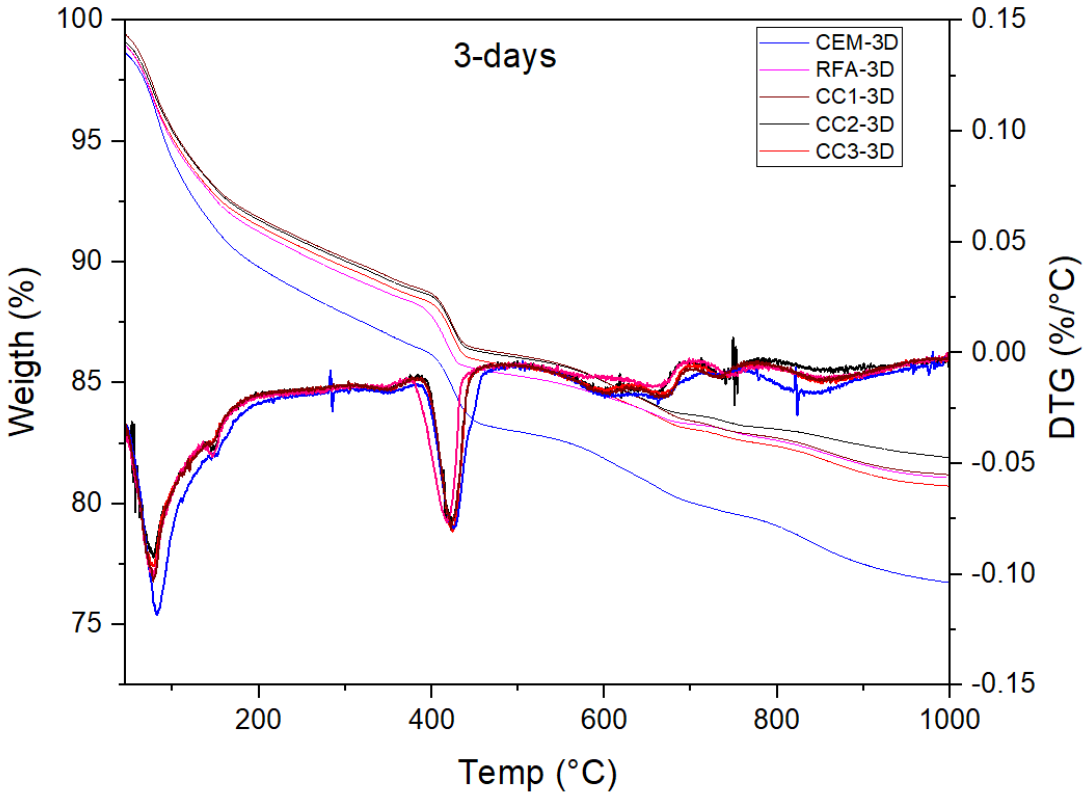

Figure 5.23 TG/DTG curves for simulated fly ash at 3 days of hydration

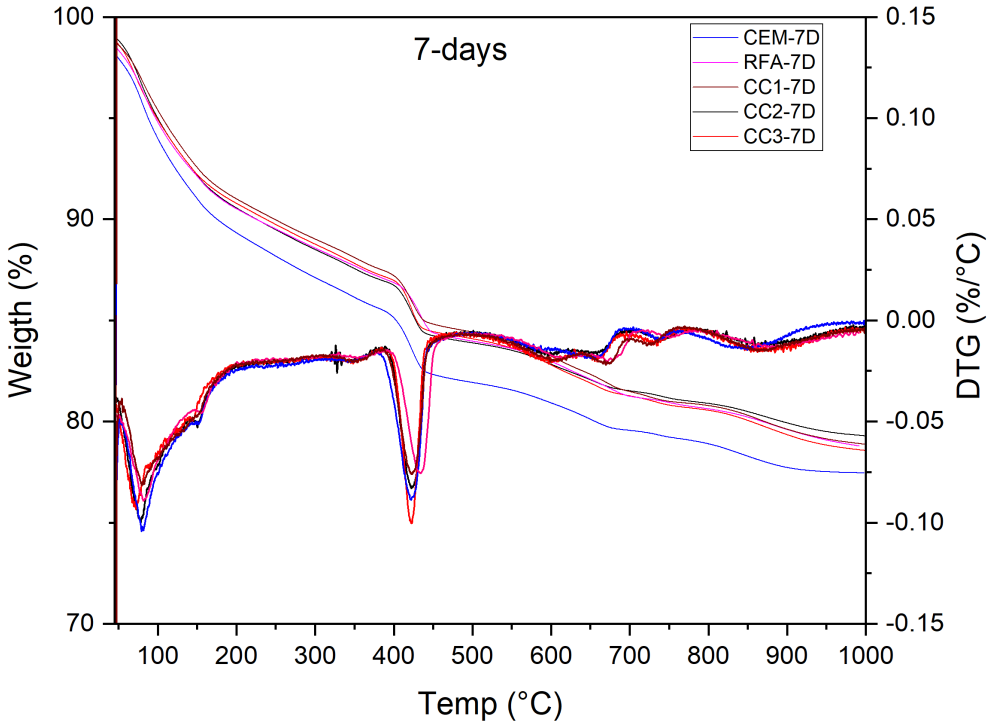

Figure 5.24 TG/DTG curves for simulated fly ash at 7 days of hydration

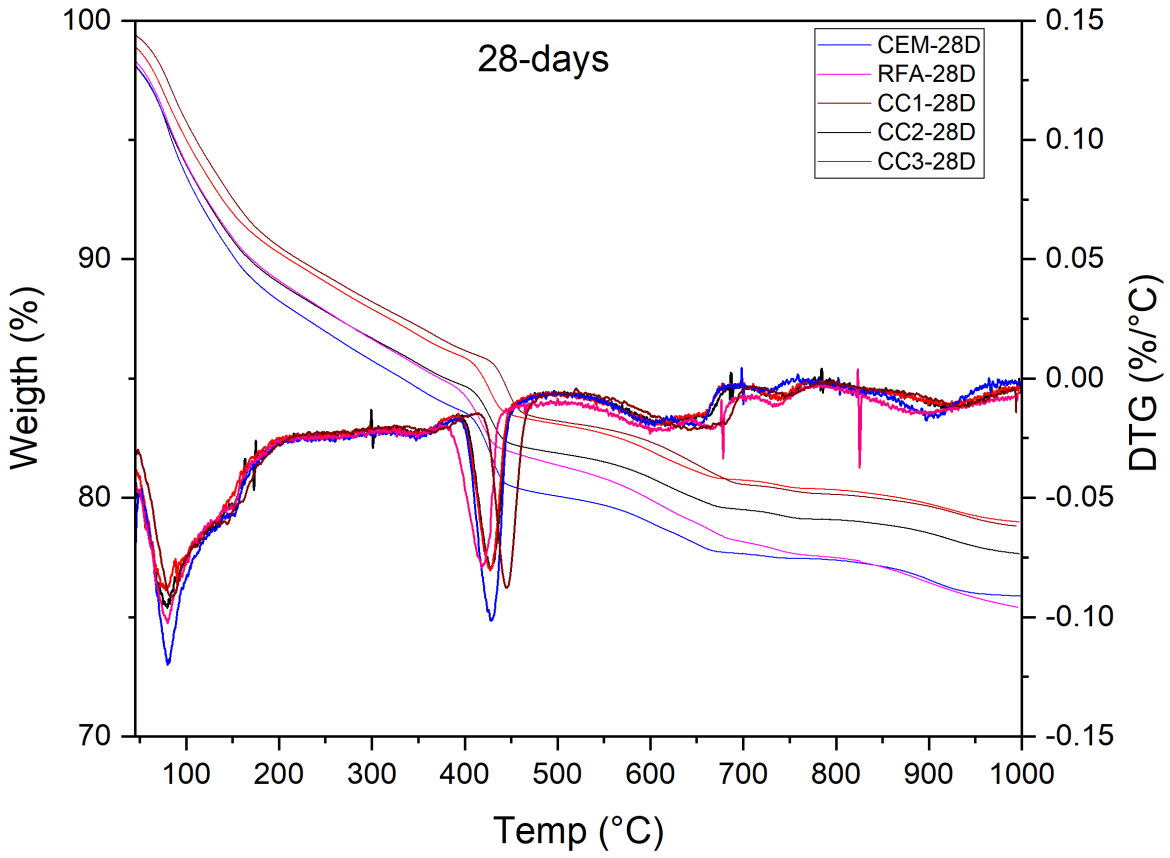

Figure 5.25 TG/DTG curves for simulated fly ash at 28 days of hydration

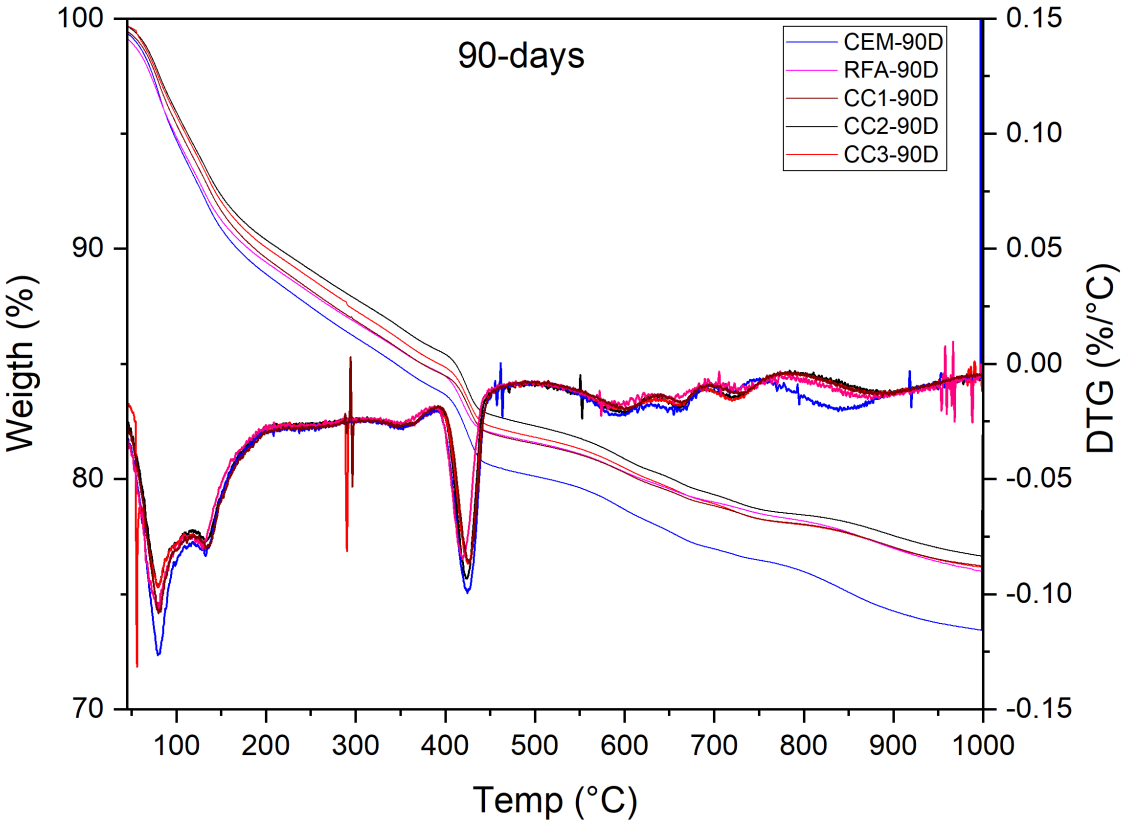

Figure 5.26 TG/DTG curves for simulated fly ash at 90 days of hydration

Table 5.4 Chemically bound water in simulated fly ash mixes

Sample	Age (days)	Ldh (%)	Ldx (%)	Ldc (%)	Wb (%)
CEM	3	7.99	2.92	6.31	13.5 (0.249)
	7	9.14	2.6	5.2	13.87 (0.295)
	28	9.74	3.11	4.9	14.86 (0.254)
	90	10.95	3.23	6.8	16.97 (0.258)
RFA	3	7.05	2.31	3.93	10.96 (0.22)
	7	8.18	2.23	5.15	12.52 (0.281)
	28	10.31	2.38	4.29	14.44 (0.35)
	90	10.28	2.61	5.57	15.17 (0.243)
CC1	3	6.83	2.25	5.2	11.21 (0.208)
	7	8.15	2.45	5.96	13.04 (0.228)
	28	9.61	2.36	5.13	14.08 (0.275)
	90	10.84	2.65	5.41	15.70 (0.242)
CC2	3	6.83	2.22	4.17	10.76 (0.204)
	7	8.31	2.65	4.97	13.00 (0.226)
	28	9.59	2.49	4.89	14.09 (0.266)
	90	10.41	2.78	5.74	15.54 (0.235)
CC3	3	6.97	2.25	5.11	11.32 (0.212)
	7	8.02	2.37	5.45	12.63 (0.232)
	28	9.53	2.46	4.29	13.75 (0.249)
	90	10.91	2.7	5.93	16.04 (0.242)

5.4 Compressive Strength Development

The compressive strength experiments were conducted on the simulated fly ashes, the real fly ash, and the cement only. Below are the results for compressive strength for 3,7, 28 and 90 days (Figure 5.27).

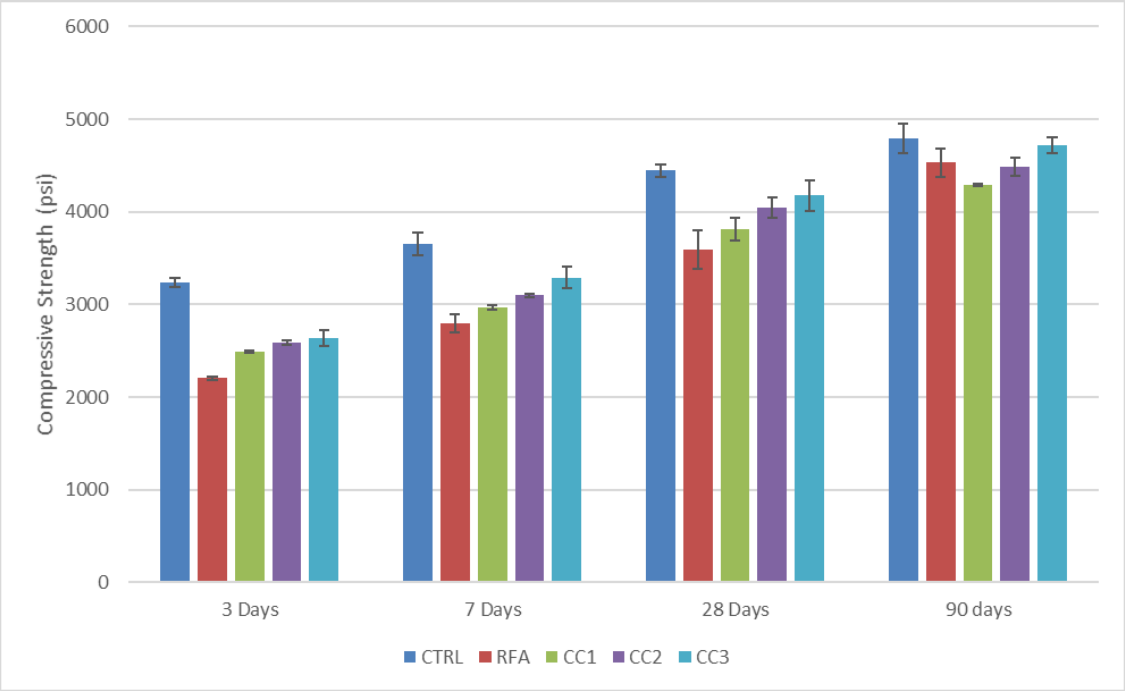

Figure 5.27 Compressive strength of mortar samples

The compressive strength results show that the fly ash reduces the strength at early ages as expected of Class F fly ashes. This is due to the dilution effect of the fly ash. All the fly ash samples gain strength with time. A plot of the relative compressive strength with respect to the control reveals the rate of strength gain of the simulated fly ash samples (Figure 5.28). The 80% relative strength line is the theoretical strength of mortar with 80% cement and 20% inert material with the same particle size distribution as the fly ash. Theoretically, this will be the strength if the fly ash was replaced with an inert material. At 3 days, the simulated fly ash samples have similar strength around 80% of the control. At 7 days, the strengths of the simulated fly ash samples are slightly higher than 80%, indicating an accelerating effect of the fly ash on the relative strength gain. This could be due to the filler effect of the fly ash, where the fine particles serve as nucleation sites for formation of

hydration products. The rate of strength gain for the fly ashes continues to improve with time, with the real fly ash reaching the 80% mark for the first time at 28 days. Between 28 and 90 days, the fly ashes see a significant gain in strength. This could be explained by the pozzolanic reaction of the fly ash finally beginning to influence the hydration. The rate of strength gain is more significant with the real fly ash, which appears to be more reactive than the simulated fly ashes. The CC2 fly ash is more reactive than CC1 in terms of compressive strength; however, it is not significant within the margin of error. This is consistent across all days. The CC3 fly ash, which has more AlSi glass than the rest, has the highest compressive strength. This is due to importance of alumina and silica in the pozzolanic reaction, which leads to the formation of C-S-H and C-A-S-H. The real fly ash has the lowest strength at earlier times, but performs better at 90 days, perhaps due to better overall reactivity.

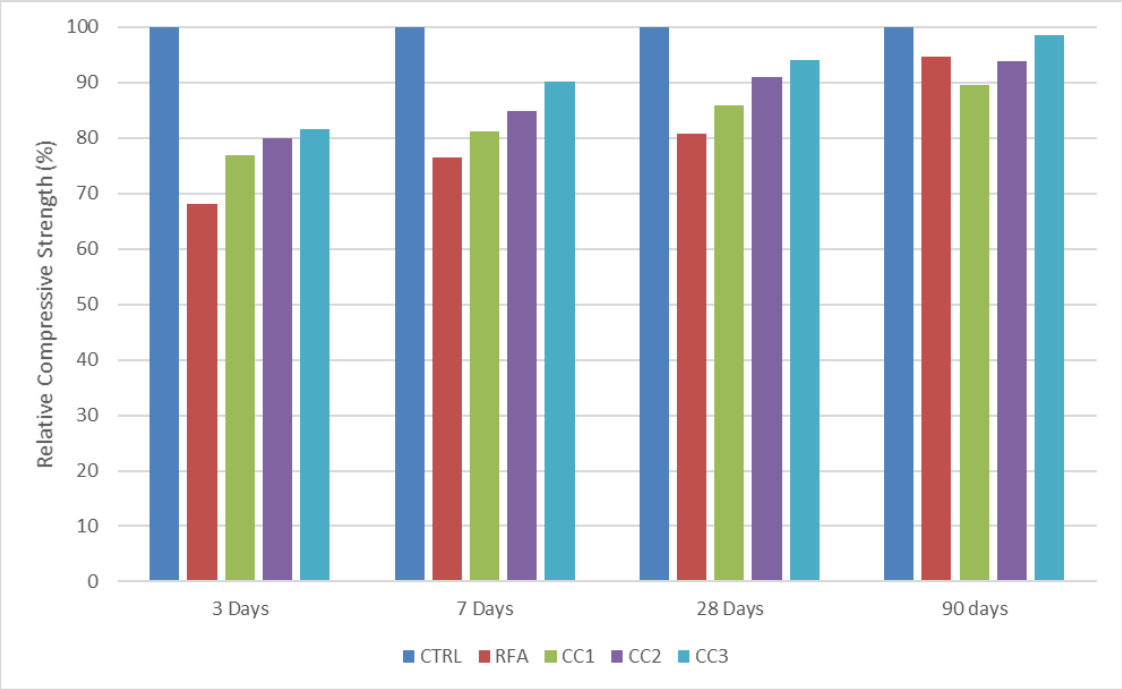

Figure 5.28 Relative compressive strength of mortar samples

5.5 Degree of Fly Ash Glass Reaction

The degree of fly ash glass reaction was determined using SEM with Multipsectral Image Analysis (SEM/IA). An image set from the EDS element maps is presented here to illustrate the processing steps and the resulting images. Figure 5.29 shows the raw element maps obtained from the SEM/EDS system, shown in false colors applied by the SEM/EDS system. The Si element map image shown in Figure 5.30 is used as an example to illustrate the steps used to process the images for multispectral image analysis. The raw unprocessed Si element map image from the SEM/EDS was converted to grayscale in ImageJ to remove the false color applied by the EDS software. The image was cropped to remove the scale and title text (in some cases, the image was saved without the title text). The resulting greyscale image is

shown in Figure 5.31. After conversion to grayscale, a median filter of radius 2 was applied to reduce background noise in the image. The resulting image is shown in Figure 5.32. The noise or background signal was then clipped from the image using the Image Adjustment – Brightness/Contrast feature of ImageJ. The brightness is also enhanced at this stage. The resulting clipped image is shown in Figure 5.33.

Each elemental image was preprocessed as described above in ImageJ except the backscatter image, which was not subjected to background noise reduction and clipping, before being linked to form a multispectral image stack in MultiSpec.

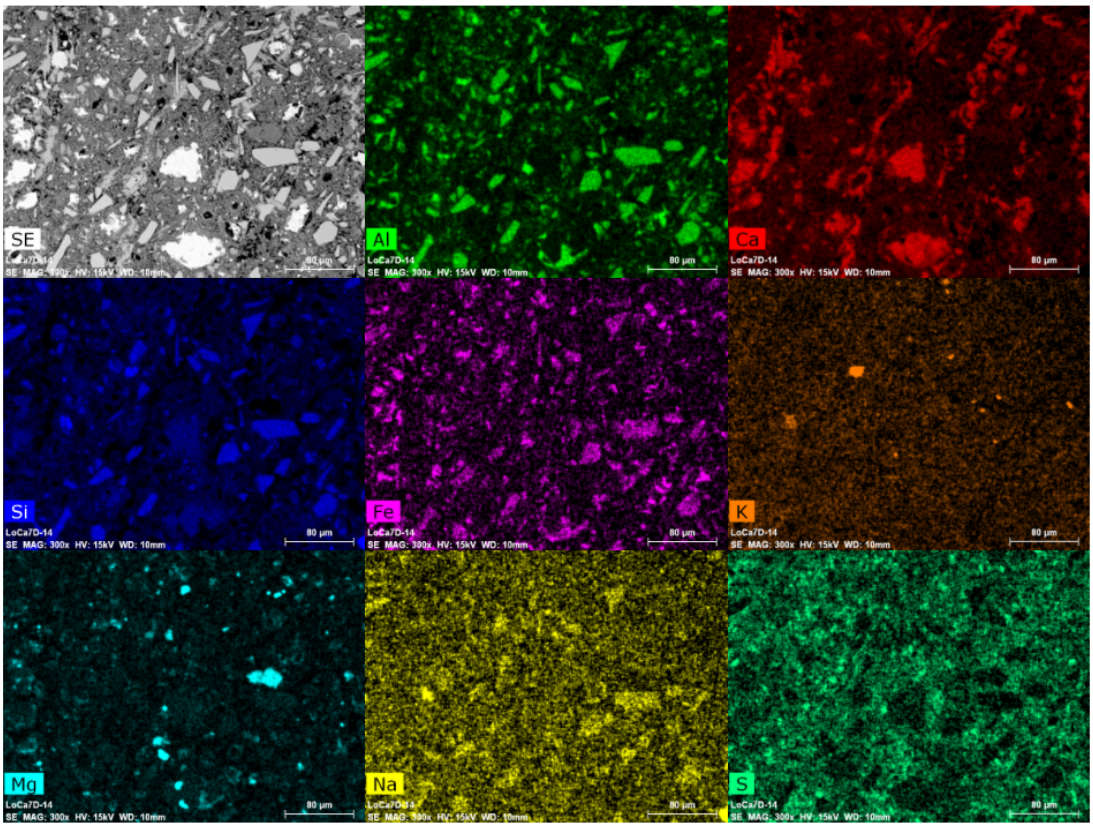

Figure 5.29 EDS element maps for various elements (LoCa at 7 days)

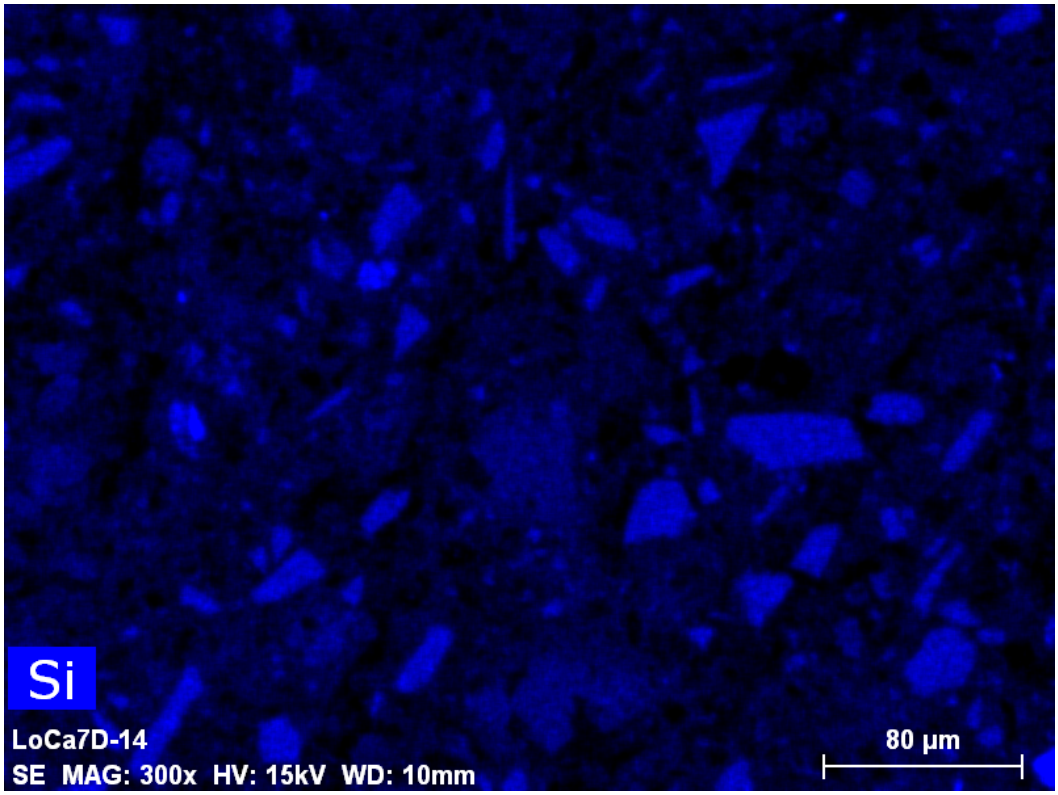

Figure 5.30 EDS element map for Si

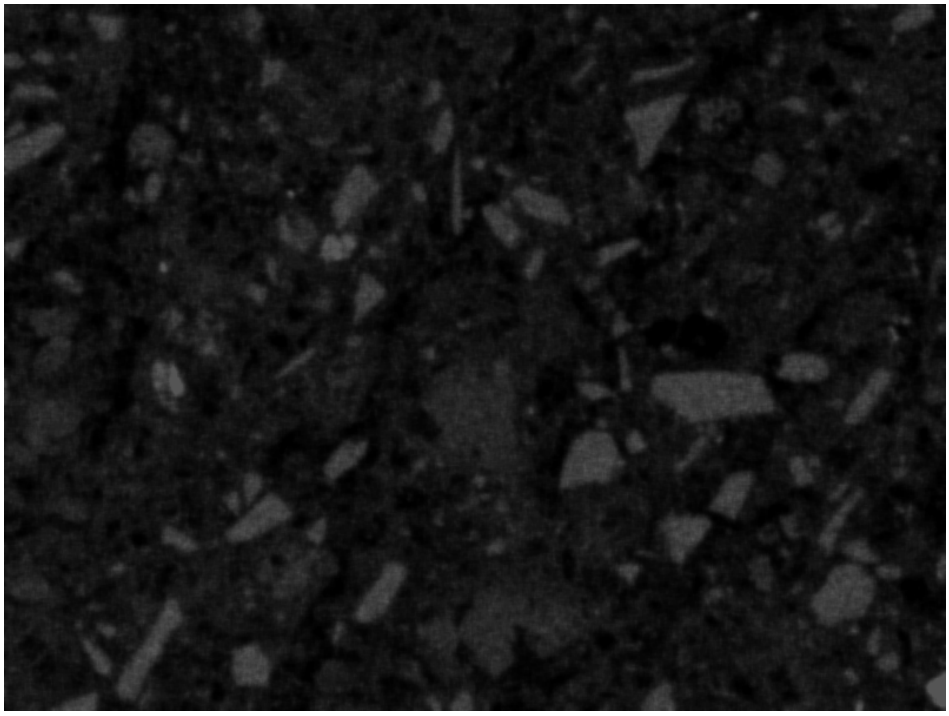

Figure 5.31 EDS grayscale image for Si

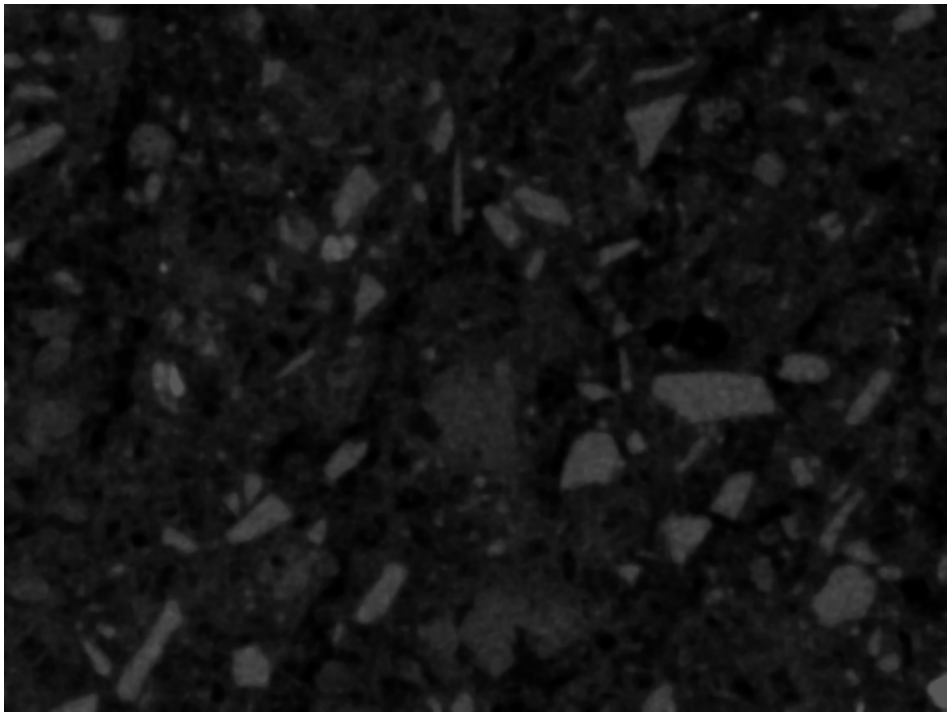

Figure 5.32 Median filtered grayscale image of Si

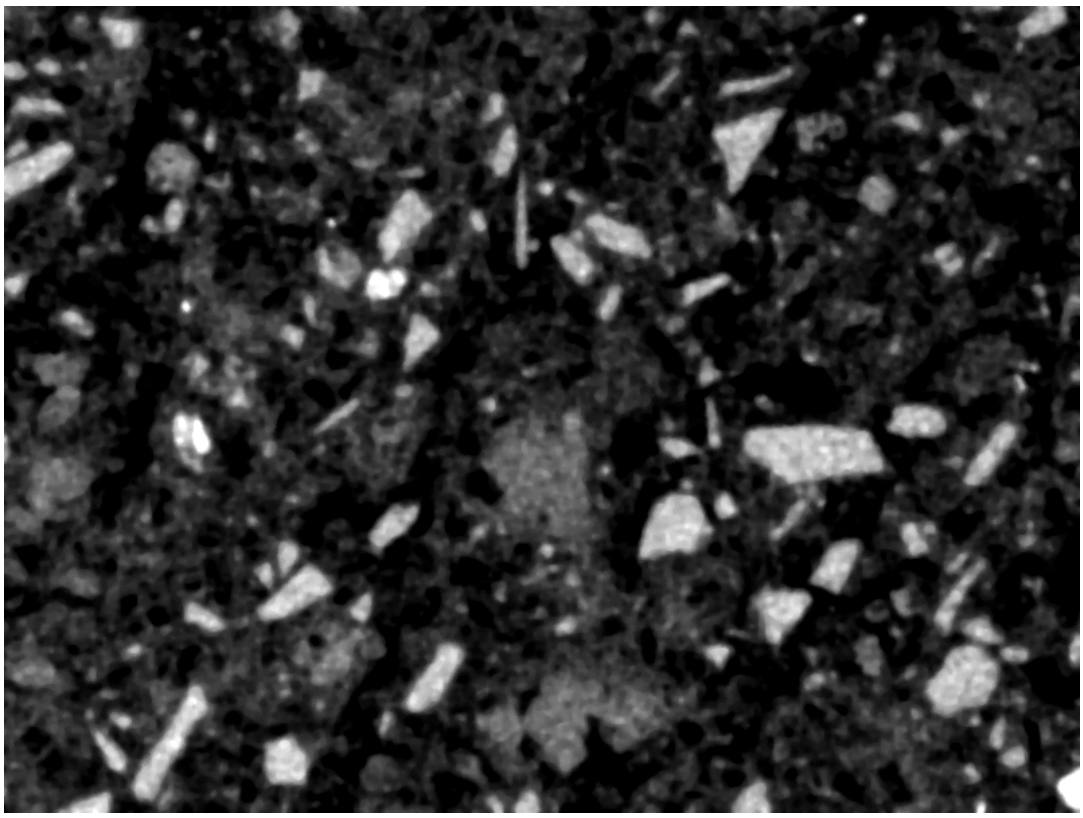

Figure 5.33 Clipped and enhanced grayscale image for Si

After processing, each elemental image was linked in MultiSpec to form a multispectral image stack following procedures outlined in Lyndon (2005). The viewing of the image overlays in the stack is limited to three images (elements) at a time, one each in the red, green, and blue (RGB) color images (Figure 5.34).

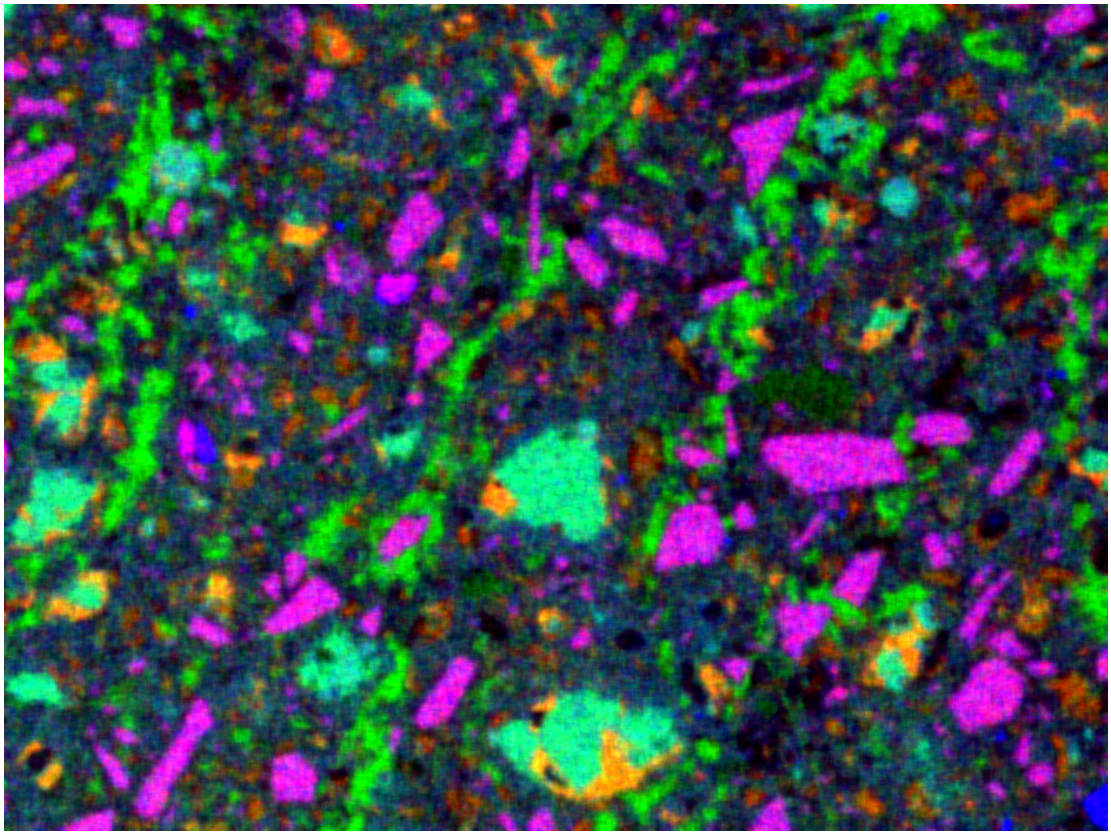

Figure 5.34 Multispectral overlay of Al, Ca, and Si (Red, Green, and Blue, respectively)

A cluster analysis was performed to identify, segment, and quantify the remaining glass particles. As explained earlier, the unsupervised cluster analysis method was used to auto generate clusters in order to avoid operator bias in the supervised training sets methods. The ISODATA method of cluster analysis in Multispec was used. This cluster analysis method starts with a pre-determined initial set of clusters, the number of which is set by the user. According to (Lyndon 2005), this number should be about three times the number of mineral phases (channels) known to be present in the sample. The Na, K, and S images (channels) were discarded since they are very minor (trace) elements of the glass and had a lot of

noise in the images. This resulted in 5 mineral element map images, therefore, 15 clusters were used for the preliminary clusters. About five clusters had area fractions less than 1%. Therefore, the number of clusters was reduced to 10 for the analysis, since Ca, Al and Si were the main components of the glass. This work is focused on finding the remaining glass. Preliminary testing showed that using the BSE, Si, Al, and Ca images was enough to identify and segment the glass particles. A visual comparison of the clustered image and the BEI image was made after each analysis to ensure that all the glass particles have been identified and clustered. The resulting clustered image is shown in Figure 5.35.

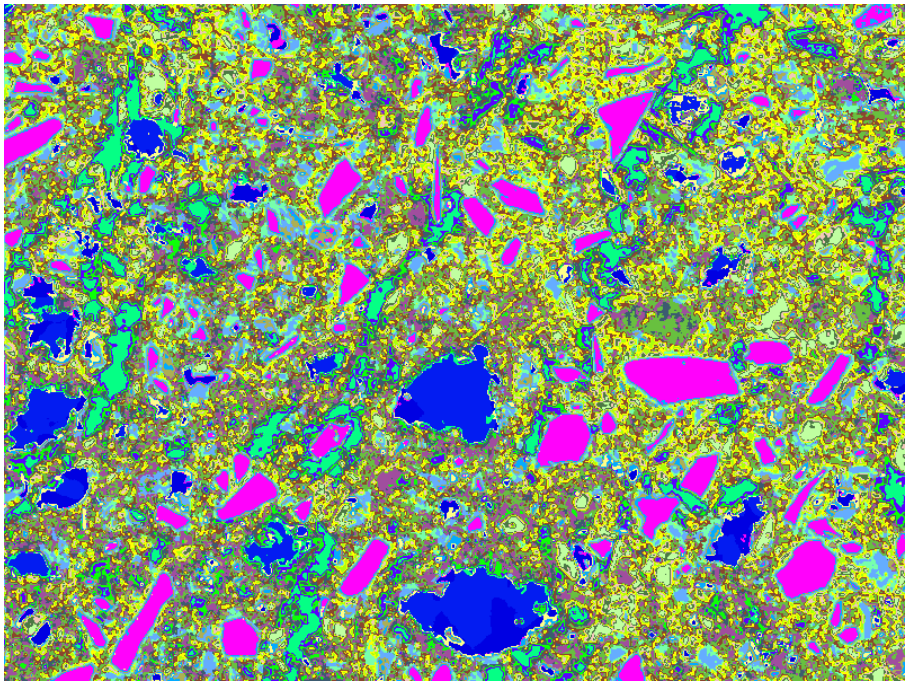

Figure 5.35 Cluster map showing synthetic fly ash glasses

The Multispec analysis was used to quantify the area fractions of the remaining glass, from which the degree for hydration was calculated. Figure 5.36 shows the degree of hydration.

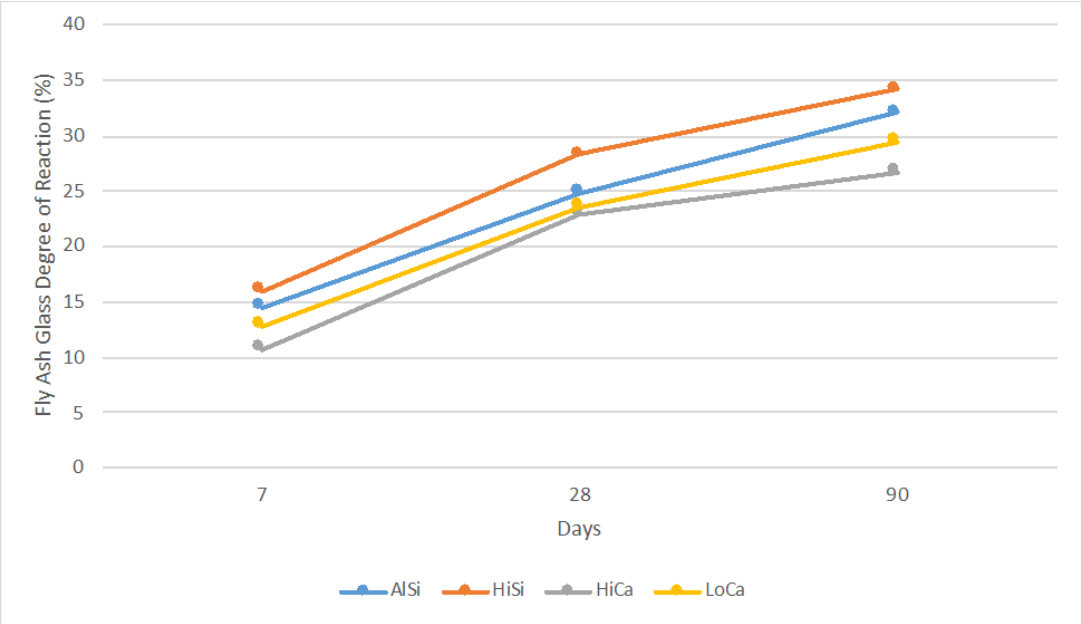

Figure 5.36 Degree of reaction of fly ash glass

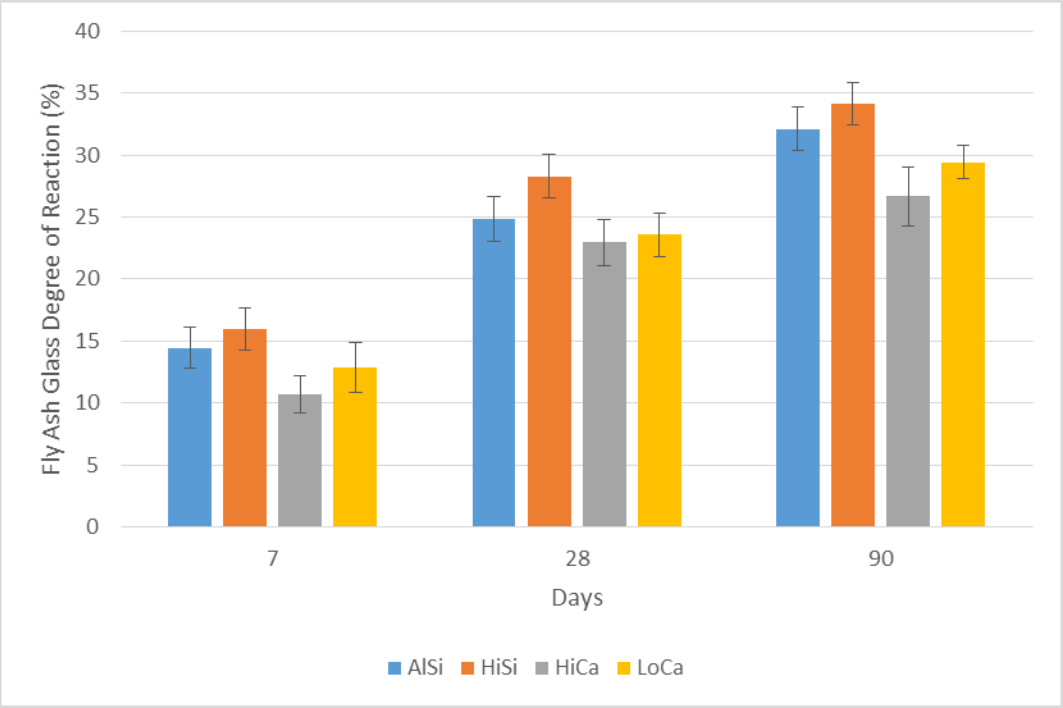

Figure 5.37 Degree of fly ash glass reaction

The HiCa glass appears to be the least reactive, with the HiSi and AlSi being the most reactive (Figure 5.37). However, the glasses have similar reactivities within the margin of error.

5.5.1 Particle Size Analysis of Remaining Glass

Particle size analysis was performed to determine how the particle size distribution of the remain glass changes with time, using the histogram of the remaining glass after image analysis. The remaining glass identified in Multispec was exported to ImageJ for particle size analysis. This involved counting the remaining particles and determining the size of each particle. This was done to determine the particle size distribution of the remaining glass. Figure 5.38 shows the glass particles

and the counting procedure in ImageJ. Figure 5.39 shows the distribution of the particles in a histogram of relative frequencies.

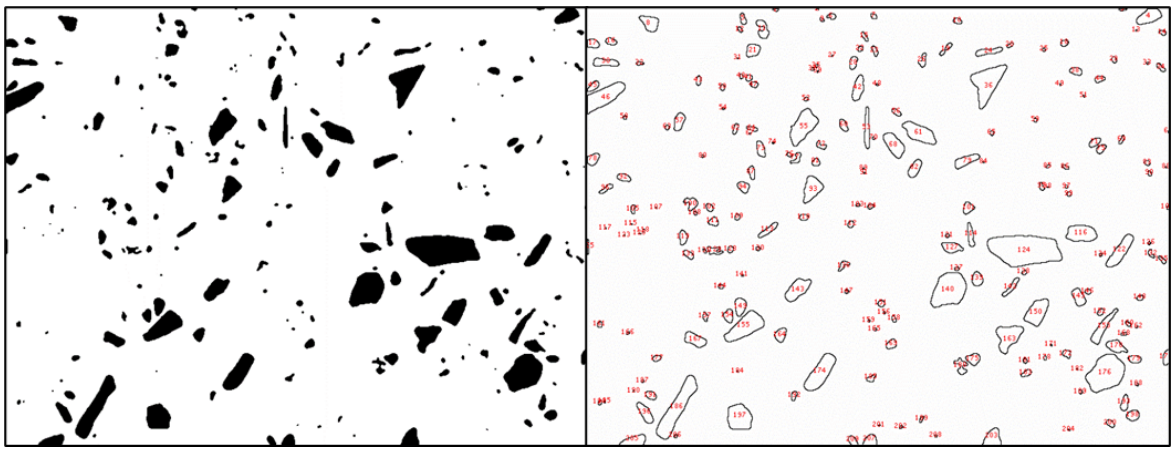

Figure 5.38 Particle counting of remaining glass in ImageJ

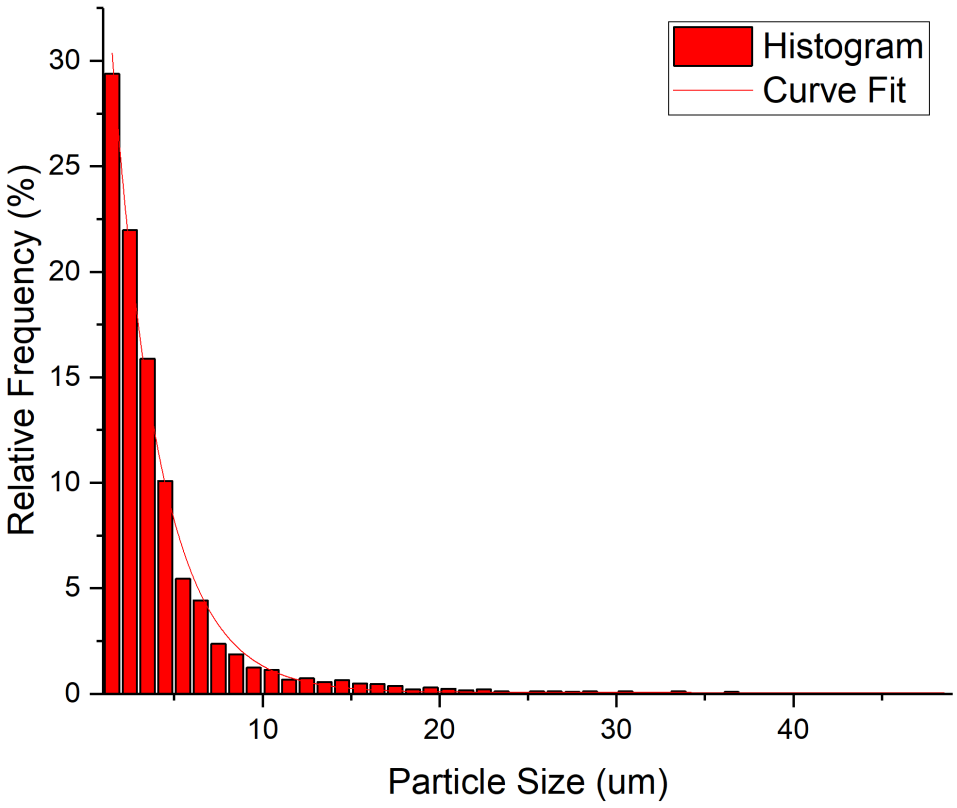

Figure 5.39 Histogram of particle size distribution of remaining glass

The histogram of the particle sizes follows an exponential decay curve. This implies that the proportion of smaller particles is higher in number than the proportion or larger particles. In order to semi-quantitatively characterize the nature of this exponential distribution of the histogram, an exponential curve was fitted to this histogram. An exponential decay function of the form of Equation 5.1 was fitted to the histograms.

$$y = y_0 + Ae^{-k(x-x_0)} \qquad 5.1$$

where x is the particle size, x_o is the minimum possible particle size, y is the frequency, A is the frequency at x_o, k is the decay constant and y_o is the background,

Each of the curves was fitted with the above exponential curve, and the $T_{1/2}$ (the half life) was determined. This was done using Origin Pro graphing software. Figure 5.40 shows a plot of the exponential curve fits for the HiSi sample at 7, 28, and 90 days of hydration.

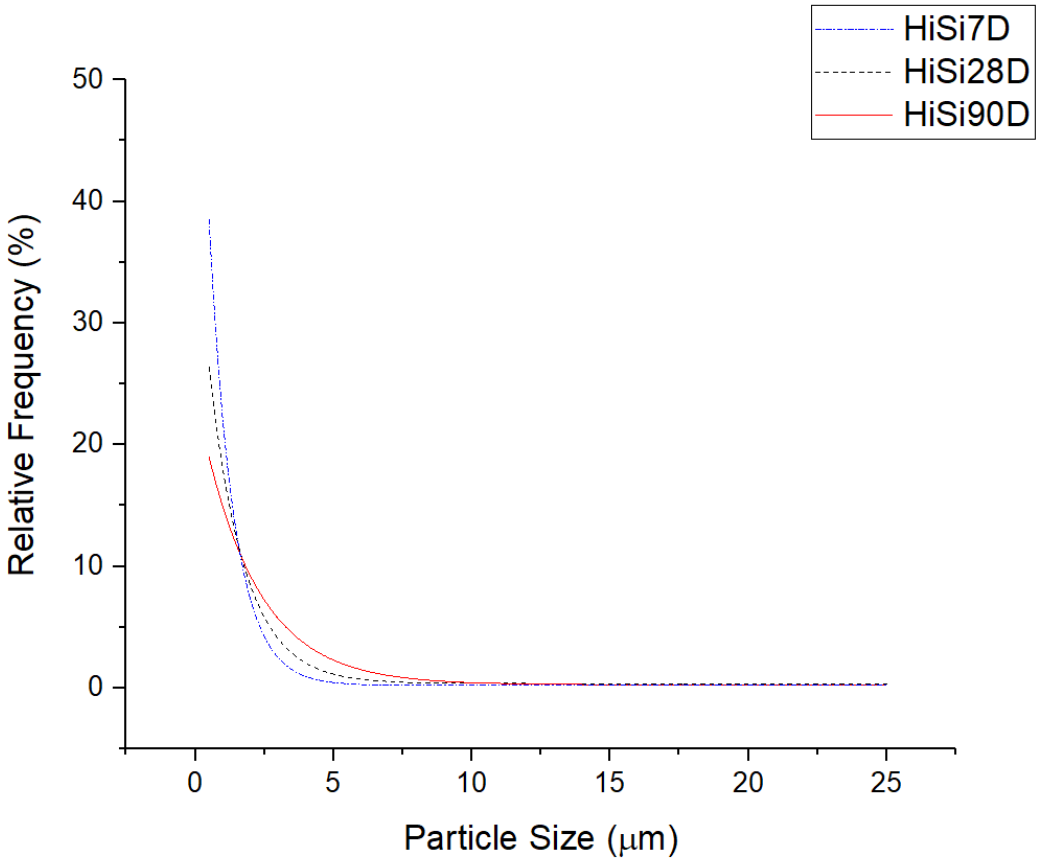

Figure 5.40 Fitted exponential decay curves for remaining HiSi glass particle sizes

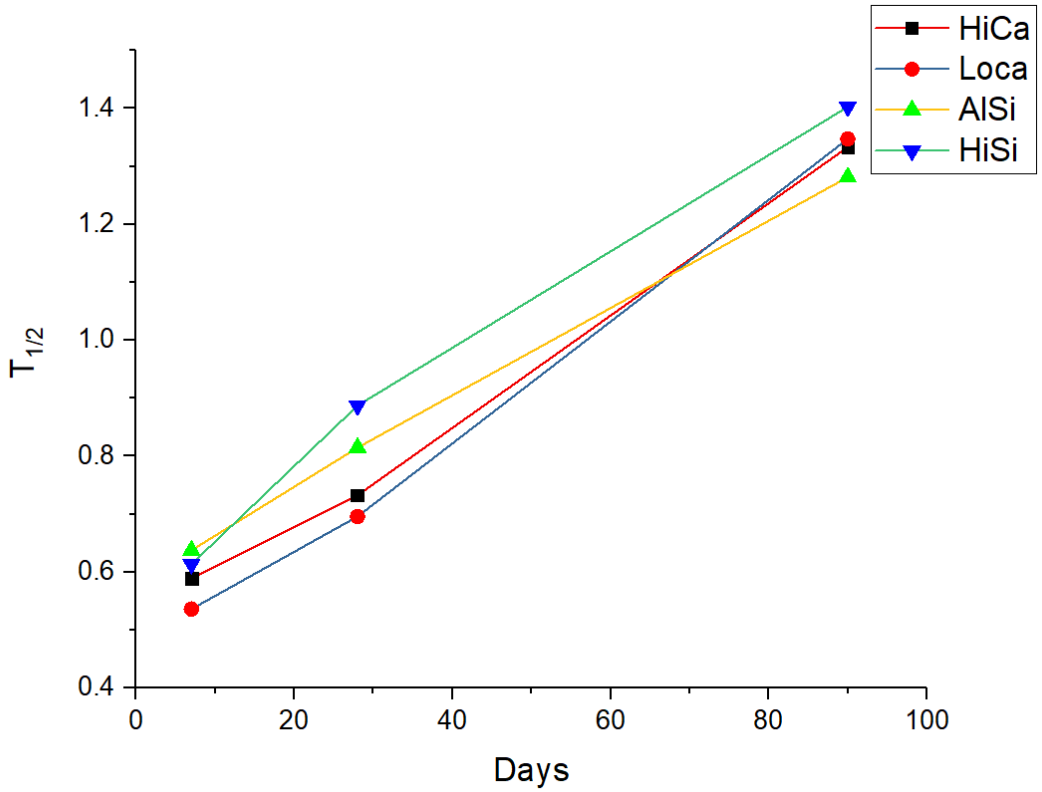

Figure 5.41 $T_{1/2}$ of exponential decay curves for synthetic fly ash glasses at 90 days

There appears to be a correlation between the slope of the fitted curve of the histogram and the age of the sample. The older the sample, the flatter the slope of the curve. This can be explained by a shift in the bin location of a particle that has shrunk (reduced in size) due to hydration at the rims, or particles becoming so small as they react to the point where they are observable at the resolution of the SEM.

5.6 XRD

XRD coupled with Rietveld analysis can only be used to quantify crystalline phases, or the total amount of amorphous materials if an internal or external standard is used. However, this approach is not very useful in blended cementitious materials where the main hydrate C-S-H and the SCMs are all amorphous. Therefore XRD is

used for qualitative analysis only in this research. The hydration products identified by XRD include ettringite, AFm, calcium hydroxide, and C_4AH_{13}. The AFm phases result in relatively broad peaks due to the poor crystallinity of AFm.

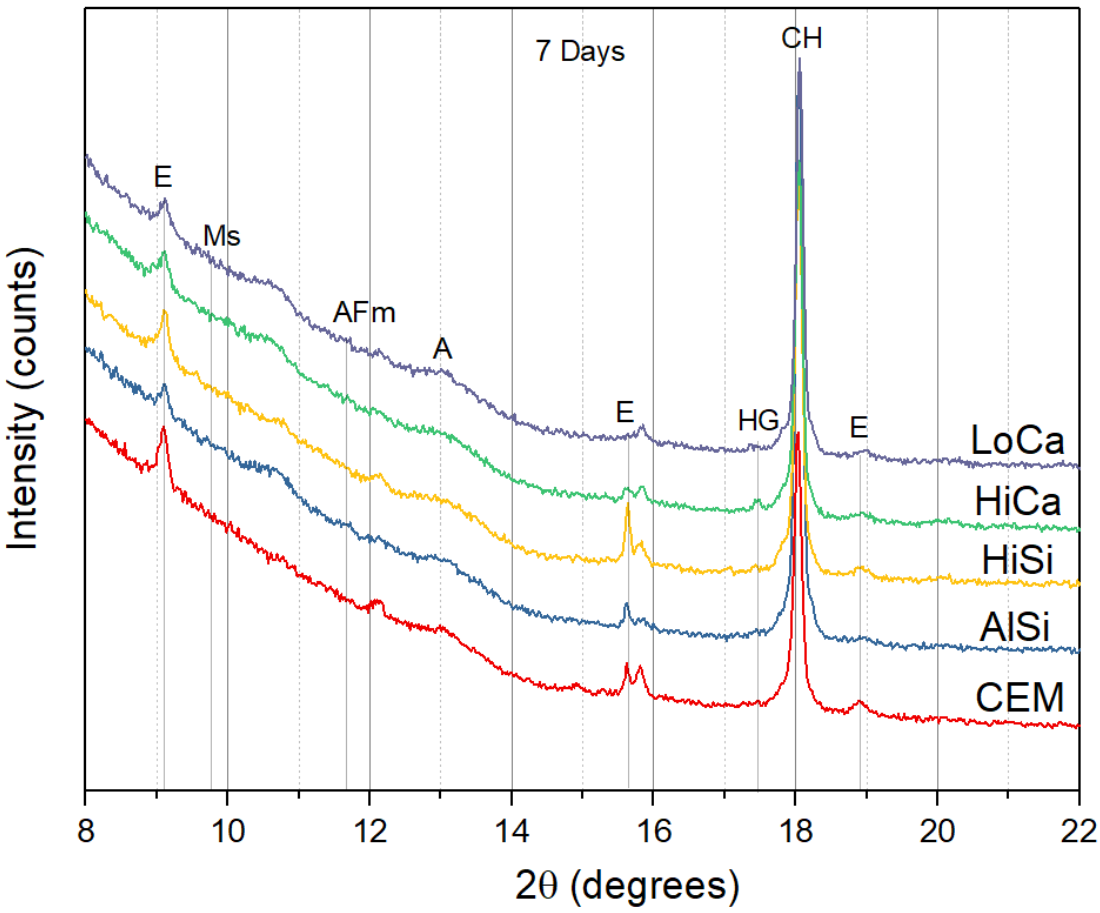

Figure 5.42 XRD pattern of synthetic fly ash cement samples after 7 days. E-ettringite, Ms-monosulfate, AFm, CH-calcium hydroxide, HG-hydrogarnet, Ht-hydrotalcite, A-C_4AH_{13}

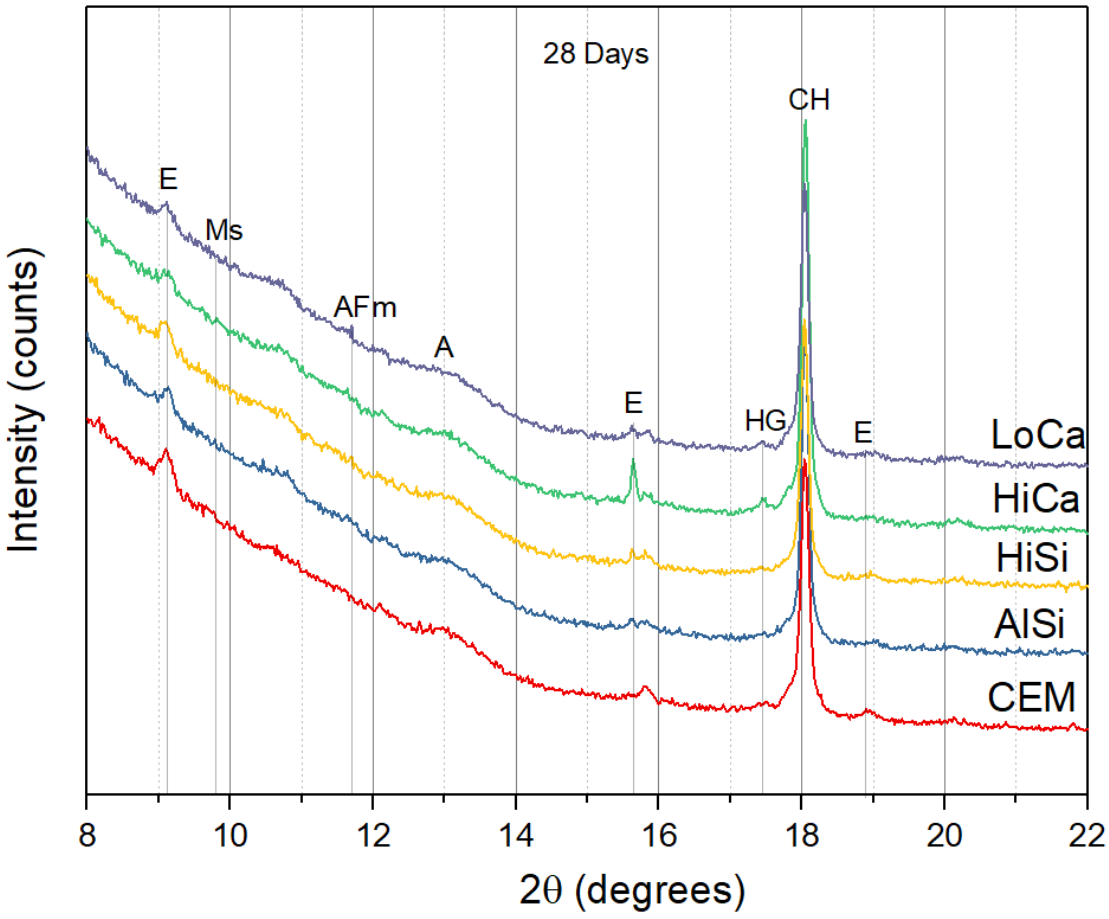

Figure 5.43 XRD pattern of synthetic fly ash cement samples after 28 days. E-ettringite, Ms-monosulfate, AFm, CH-calcium hydroxide, HG-hydrogarnet, Ht-hydrotalcite, A-C_4AH_{13}

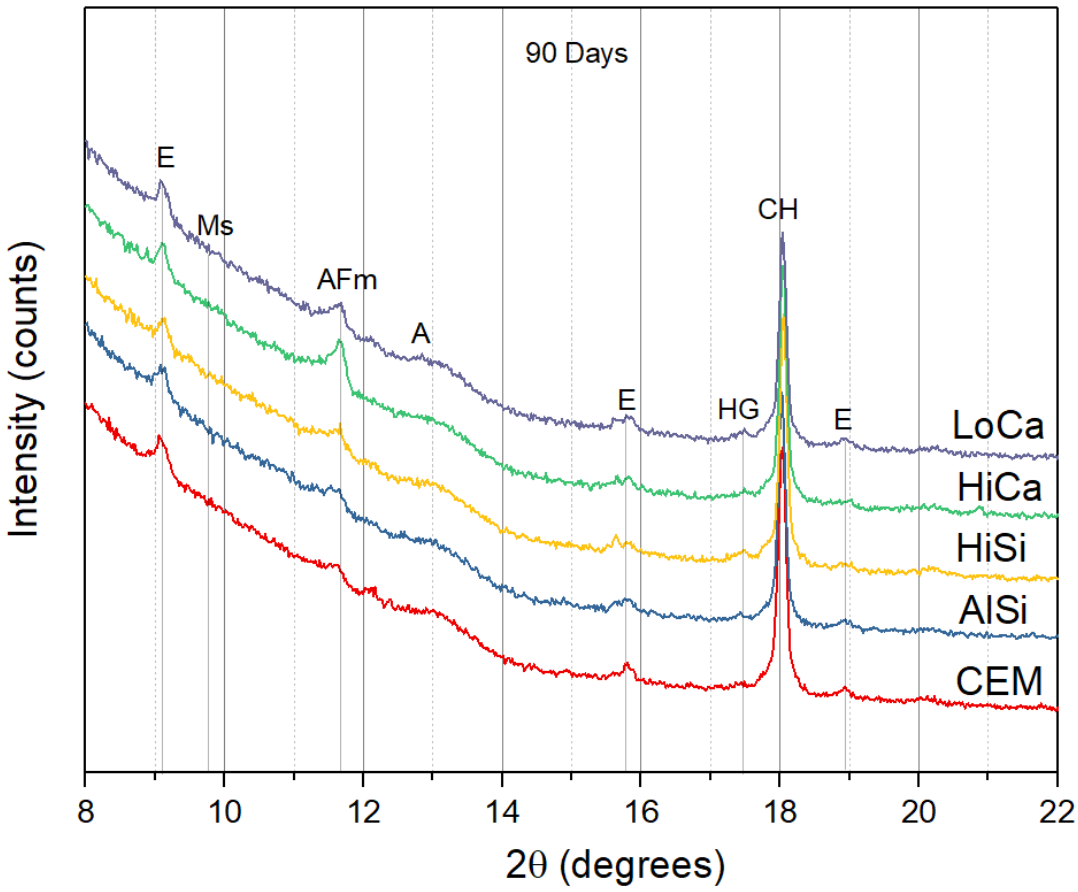

Figure 5.44 XRD pattern of synthetic fly ash cement samples after 90 days. E-ettringite, Ms-monosulfate, AFm, CH-calcium hydroxide, HG-hydrogarnet, Ht-hydrotalcite, A-C_4AH_{13}

5.7 Probe Analysis

The microprobe analyses were carried out on the synthetic fly ash glass and cement mixes to characterize the C-S-H phase, which is mainly amorphous and not detectable by XRD. Spot analyses were targeted at the outer product in the matrix of the hydrates and the inner product of the fly ash and clinker. Due to the interaction volume of electrons with the specimen and the intergrowth of hydrates during the hydration process, the detected X-rays of one spot often consist of a mix of two or

more phases (Scrivener 2004). The composition of the spots analyzed is presented in element ratio plots of Al/Ca versus Si/Ca as shown in Figure 5.45 (Deschner et al. 2012). The analysis was performed for the 90 days samples. The Al/Si ratio of C–S–H is determined by the slope of a line drawn through the points with the lowest Al/Ca ratio and represents mixed analyses of portlandite and C-S-H without AFm or ettringite. The range of Si/Ca ratios of the C–S–H is represented by the bulk of the data points along this line (Deschner et al. 2012). The points with lower Si/Ca ratios represent mixed analysis of C-S-H and portlandite. The measurements of the fly ash glass blends are more scattered than that of the pure cement as the hydrates are analyzed together with fly ash glass particles of variable composition. The modification of the C-S-H by the fly ash due to the uptake of Al in the C-S-H leads to higher Al/Si ratios and lower Si/Ca ratios. The C-S-H composition of the HiSi, AlSi, LoCa samples are not significant within the margin of error. The lower Ca/Si ratios in the fly ash blended OPC are due to the additional Si, provided by the fly ash dissolution, which is incorporated in the C–S–H and results in longer silicate chain lengths. This in turn leads to an increased uptake of aluminum, which is incorporated in the bridging tetrahedra of the silicate chains. The AlSi glass had the highest Al/Si ratio, due to its higher aluminum content, followed by HiSi, LoCa, HiCa, and the neat cement paste.

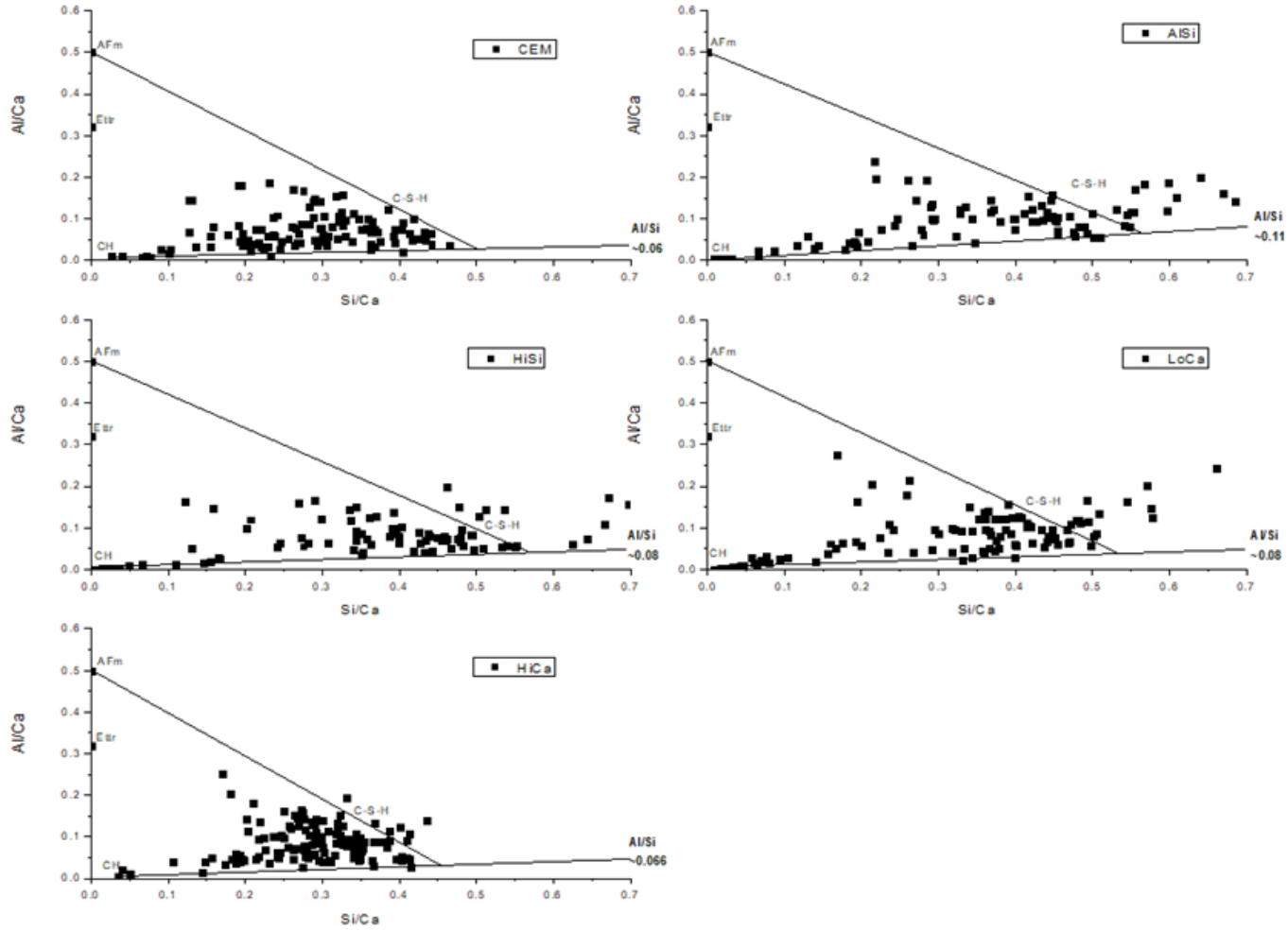

Figure 5.45 Plot of Al/Ca versus Si/Ca atomic ratios for cement and blended fly ash glass samples at 90 days

5.8 SANS Analysis

The analysis of the SANS data showed inconsistent results. This was attributed to the difficulties of comparing the data from the multiple samples repeatably. Therefore, the data was regarded as unusable.

5.9 Discussion of Results

5.9.1 Relative Reactivity of Fly Ash Glasses

Several tests of reactivity were applied to the samples in this research. The results are summarized in Table 5.5 and Table 5.6. Each test method measured a different variable related to reactivity. Consequently, it is not possible to develop a common score that can be compared across the various methods. Instead, a nonparametric approach is used. The samples are ranked from highest to lowest in each column according to the values measured by that test method. For each method, the ranking of reactivity is based on the latest times measurements were taken. Also, some tests were not feasible depending on the form of the sample.

Table 5.5 Relative reactivities of synthetic fly ash glasses

Calorimetry	**TGA**	**SEM-EDS Image Analysis**	**Particle Size**
HiCa	AlSi	HiSi	HiSi
LoCa	LoCa	AlSi	LoCa
AlSi	HiSi	LoCa	HiCa
HiSi	HiCa	HiCa	AlSi

Table 5.6 Relative reactivities of simulated fly ashes

Calorimetry	**TGA**	**Thermoporosimetry**	**Compressive Strength**
CC3	CC3	CC3	CC3
CC2	CC1	CC2	CC2
CC1	CC2	CC1	CC1

For the synthetic fly ash glasses, the rankings are inconsistent. In the most extreme case, HiCa is ranked highest by calorimetry but lowest by SEM-EDS image analysis. The opposite is true for the HiSi glass. This may reflect the fact for some methods the differences in reactivity measured are so small that they are within experimental uncertainties. For the simulated fly ashes, the rankings are more consistent, with CC3 top ranked for all three methods, and CC2 ranked second in two out of three.

5.9.2 The Role of Ca in Glass Reactivity

The study of glass corrosion has shown that the various ions play different roles in controlling the stability of glasses exposed to aqueous solutions (Doremus

1994). The group Si, Al and Fe are glass network formers while the alkalis K and Na are network destroyers because they are readily leachable. The alkaline earths Ca and Mg act as network modifiers. Depending on the other ions such as aluminum that are present in the glass, the Ca ion can have either stabilizing or a destabilizing effect. This is characterized by the aluminum saturation index (ASI) which is calculated as the molar formula:

$$ASI = \frac{Al}{2Ca + K + Na} \qquad 5.2$$

Table 5.7 ASI of synthetic fly ash glasses

HiSi	**LoCa**	**AlSi**	**HiCa**
0.295	0.181	0.580	0.101

The calculated values are presented in Table 5.7. A comparison of these results with the measured reactivities in Table 5.5 does not show a consistent pattern.

5.9.3 The Role of Fly Ash as Filler vs Reactant

As described in the literature review, there is a debate about the role that the fly ash particles play in the development of the C-S-H gel. It could serve simply as an inert filler, which provides more surface area for the nucleation and growth of the C-S-H and other hydration products produced by the main cement hydration reactions, in which case the chemical composition of the fly ash glass is irrelevant. Alternatively, it could play an active role by generating additional C-S-H through the pozzolanic reaction, in which case the chemical composition would be relevant.

The results of the various reactivity tests indicate that the fly ash glass plays both roles at different times. The calorimetry and TGA results show that at early stages the amount of gel increases with the presence of fly ash. However, the glass does not appear to be very reactive at this stage, which implies that it is serving mainly as a filled. In contrast, the SEM-EDS and EPMA results show that at later stages, the glasses are in fact reacting to form C-S-H gel and other hydration products.

5.9.4 Reactivity Measurement Methods

Although the primary objective of this research was to characterize the reactivity of fly ash glass as a function of chemical composition, it also provided some insights into the performance of the various reactivity test methods.

5.9.5 Glass vs Raw Fly Ash

A major innovation of this research is the use of synthetic glass particles instead of raw fly ash to investigate reactivity. This enabled the study of how the chemical composition affects the reactivity. It also avoided the confounding effect of particle size distribution. Within the resources available it was possible to make only four individual glass compositions. Thus, it was not possible to systematically explore the full composition space of fly ash. Moreover, it was difficult to make alumino-silicate glasses with low Ca and alkali content because of their high melting temperatures and viscosities.

Nevertheless, the synthetic glass samples provide a means of investigating the effects of chemical composition on reactivity that would be very difficult to do with raw fly ash. Therefore, it would be worthwhile to expand the set of synthetic glasses

to cover the fly ash compositional space more fully. The problem of making glasses with high aluminum and silicate content could be handled by using less refractory starting materials such as kaolinite rather than the oxides.

5.9.6 Bulk vs Particle-based Characterization

This research applied both bulk analysis methods such as TGA and particle-based methods such as SEM/EDS to characterize the reactivity of the fly ash glasses. The advantages of the bulk methods are minimal sample preparation, well-established standard procedures, and relatively fast data acquisition. The major disadvantage is their inability to measure the individual rates of reaction of the amorphous glass phases present. Conversely, particle-based methods require extensive sample preparation to produce polished thin sections. The image analysis is time-consuming and relies upon skilled operators. All things considered; the particle-based methods are preferable because of their greater accuracy. This is also the conclusion reached by the RILEM Committee TC 238 on the hydration of SCM (Scrivener et al. 2015b). The use of synthetic glasses rather than raw fly ashes can speed up the process considerably because many more particles of the same chemical composition can be found in a given image.

5.9.7 Reactants vs Products

The progress of the fly ash pozzolanic reaction can be quantified either in terms of the consumption of the initial reactants or the growth of the reaction products. However, the methods for measuring the consumption of reactants are difficult to apply in this case. Quantitative XRD cannot be used to measure the reduction in the

fly ash glass particles because they are amorphous, not crystalline. It could be used to measure the other reactant, calcium hydroxide. However, this can be ambiguous because the fly ash itself can also be a source of Ca. This limitation also applies to the use of TGA to measure calcium hydroxide consumption.

The amorphous glasses phases can be quantified by SEM/EDX as described above. The sensitivity of the method is limited by the spatial resolution, or pixel size, of the image which makes it hard to detect small changes in particle size resulting from slow reaction rates.

On the other side of the equation the quantification of the C-S-H gel growth is hampered because it is also amorphous. The available methods do not measure the mass of the gel directly, but rather the changes in porosity. TGA measures the water in the pores, but this can be confounded by water bound up in other phases such as ettringite. SANS has been used previously by Bumronjaroen et al. (2009) to measure the growth of nanopores. However, its application in this research proved to be inconclusive due to experimental issues.

In summary, the most promising methods for measuring the consumption of reactants is SEM-EDX and for measuring the growth of reaction products is SANS. Both methods need to be refined and standardized.

5.9.8 Heat Rate vs Reaction Progress

The vast majority of the research on cement and fly ash hydration has relied upon isothermal calorimetry. This measures the rate of heat release during the reaction. The heat rate can be integrated to give the cumulative heat. This is often treated as a measure of reaction progress by assuming a fixed value of heat released

per unit of reactant consumed. This may be justified in the case of a single reactant, e.g., the hydration of C_3S. However, in the case of Portland cement hydration in which several phases are reacting simultaneously, it becomes problematic. Moreover, calorimetry is feasible only during the early stages of hydration when the heat rate is high enough to be detected. However, the pozzolanic reaction involving fly ash only becomes significant at longer times. Consequently, calorimetry may not be as reliable a measure of fly ash reactivity compared to other methods like SEM-EDS mapping that measures the reaction progress directly. This could explain the discrepancy in the rankings shown in Table 5.5.

5.9.9 Other factors for future investigation.

There were several important factors in fly ash reactivity that could not be investigated during this research because of limited time and experimental resources. These include the replacement factor, the water/cement ratio and the particle size distribution. These were kept constant in order to isolate the effects of fly ash glass chemistry. This procedure can be reversed in future research by keeping the fly ash composition fixed and varying the individual factors systematically. The replacement factor involves two competing processes: the creation of additional C-S-H by the pozzolanic reaction and the reduction of excess CH by dilution of the cement content. The industry practice has been to use a fixed replacement factor of 20% of cement. However, Livingston and Bumrongjaroen (2005), using a chemographic model, showed that the optimum value ranged from 15-20% and depends on the chemical compositions of both the fly ash and the cement. This model assumes that the reactions go to completion. However, this may not be achievable within a civil

engineering time frame. An experimental approach to determine the optimum replacement factor for a given composition of fly ash and concrete would be to make up a set of mixes using synthetic fly ash at different replacement factors and measure the degree of reaction after a specified time interval.

The water/cement ratio determines the initial porosity. If this is less than the volume of C-S-H that can be produced by the combination of the main C_3S hydration reaction and the fly ash pozzolanic reaction, then they cannot go to completion. The particle size distribution of the fly ash determines the available surface area for reaction. This can be modified by grinding or by sieving.

5.9.10 Improved Fly Ash Classification Methods

The current ASTM method for classification of fly ash, ASTM C618-19, has many drawbacks. Livingston et al. (2019) have shown that based on automated individual particle analysis (ASEM) that the bulk XRF method used as the basis for this standard cannot accurately describe the glass content. Consequently, they have proposed an improved classification method based on ASEM and a set of standard glass compositions (Bumrongjaroen et al. 2011). Durdziński et al. (2015) have reached a similar conclusion that the bulk XRF method must be replaced by individual particle analysis as the basis for classification. The major differences in the proposals of the two groups are in the analysis method and in the development of the classes. Durdziński et al propose the use of SEM/EDX image maps to quantify the composition of the fly ash particles. This limits the number of particles that can be analyzed in a fly ash to the frame size and resolution of the SEM/BSE images. It also requires operator input to threshold background pixels from gray-level histograms.

The automated method proposed by Bumrongjaroen et al. can analyze 10,00 particles per sample, providing a much more accurate characterization of the fly ash.

Durdziński et al. propose a set of 4 classes based on analysis of the reactivity of raw fly ashes. The drawbacks of this approach have been discussed above. The approach proposed by Bumrongjaroen et al. to develop the classes is based on the cluster analysis of a large number of fly ashes by ASEM. The number of classes would then be set by the range in reactivity associated with variations in the characteristic reactivity of each cluster. This in turn would be determined from synthetic fly ash glass samples using the methods investigated in this research.

Chapter 6: Conclusions and Recommendations

This research utilized simulated fly ash to investigate the effects of variations in the chemical composition on the performance of the fly ash in cement paste samples. This is part of efforts to improve the classification of fly ash for optimal use in concrete using a standard set of glasses. The simulated fly ashes and the synthetic glasses alter the performance of the blended pastes in various ways. Various analytical techniques were used to assess the performance of the fly ashes on various length scales.

6.1 Conclusions

1. Automated particle SEM shows that fly ash glass particle compositions are not random, but rather occur in characteristic clusters.
2. Synthetic fly ash glass is a valuable tool for investigating fly ash reactivity compared to raw fly ash because it enables independent control of composition and particle size distribution.
3. Isothermal calorimetry indicated that during the first 48 hours of hydration the fly ash serves mainly as a filler which provides additional surface area for C-S-H gel growth.
4. The calorimetry also showed larger peaks for AFM phases in the fly ash mixes suggesting that the fly ash provided calcium, aluminum and sulfate ions. This effect was also seen in the TGA results.
5. Among the reactivity test methods, SEM/EDS with mutispectral image analysis is the most sensitive measurement of the degree of fly ash glass

hydration. The use of synthetic fly ash glasses significantly reduced the effort needed for this method over the use of raw fly ash because a greater number of particles with the same chemistry were found in a given image.

6. The SEM/EDS analysis indicated that the HiSi glass is the most reactive is followed by the AlSi, LoCa, and HiCa glass. The HiCa glass appears to be the least reactive, which may suggest that levels of Ca in the HiCa glass may not be sufficient to be pozzolanic on its own.
7. The fly ash glasses modify C-S-H due to the uptake of Al in the C-S-H, leading the formation of C-(A)-S-H and higher Al/Si ratios.
8. Fly ash classification methods such as ASTM C618 based on bulk characterization techniques are unreliable and need to be replaced by particle-level analyses.

6.2 Recommendations for Future Work

1. The performance of the simulated fly ashes and synthetic fly ash glasses were similar within the bounds of experimental error. This is most likely due to the 20% replacement factor. Higher replacement factors such as 35% and 40% should be investigated.
2. Synthetic fly ash glasses with higher variations in chemical compositions should be investigated.
3. The effect of varying the water to cement ratio should be investigated.

4. The results are cofounded by the challenges of the state-of-the-art in determining the reactivity of fly ash using various analytical techniques. More studies are needed to further refine the analytical techniques.
5. More analytical techniques such as Nuclear Magnetic Resonance Spectroscopy (NMR) should be used to study the molecular structure of the C-S-H.
6. SANS is a promising tool for measuring the growth of reaction products that should be investigated further and standardized.

Bibliography

ACI 232. (2003). *Use of fly ash in concrete*. *ACI Committee 232*.

Alarcon-Ruiz, L., Platret, G., Massieu, E., and Ehrlacher, A. (2005). "The use of thermal analysis in assessing the effect of temperature on a cement paste." *Cement and Concrete Research*, 35(3), 609–613.

Aligizaki, K. K. (2006). *Pore structure of cement-based materials : testing, interpretation and requirements*. Taylor & Francis.

American Coal Ash Association. (2020). "Coal Combustion Product (CCP) Production and Use Survey." *American Coal Ash Association*, Denver, CO.

Andrew, R. M. (2018). "Global CO2 emissions from cement production, 1928-2017." *Earth Syst. Sci. Data*, 10, 2213–2239.

ASTM C109/C109M. (2009). "Standard Test Method for Compressive Strength of Hydraulic Cement Mortars (Using 2-in. or [50-mm] Cube Specimens)." ASTM International.

ASTM C618-15. (2015). *Standard Specification for Coal Fly Ash and Raw or Calcined Natural Pozzolan for Use in Concrete*. ASTM International, West Conshohocken, PA.

ASTM C778-09. (2009). "Standard Specification for Standard Sand." ASTM International.

Aughenbaugh, K. L., Stutzman, P., and Juenger, M. C. G. (2016). "Identifying glass compositions in fly ash." *Frontiers in Materials*, 3.

Baert, G., Hoste, S., De Schutter, G., and De Belie, N. (2008). "Reactivity of fly ash in cement paste studied by means of thermogravimetry and isothermal

calorimetry." *Journal of Thermal Analysis and Calorimetry*, Springer Netherlands, 94(2), 485–492.

Bager, D. H., and Sellevold, E. J. (1986a). "Ice formation in hardened cement paste, Part I - room temperature cured pastes with variable moisture contents." *Cement and Concrete Research*, 16(5), 709–720.

Bager, D. H., and Sellevold, E. J. (1986b). "Ice formation in hardened cement paste, Part II — drying and resaturation on room temperature cured pastes." *Cement and Concrete Research*, 16(6), 835–844.

Barret, P., and Ménétrier, D. (1980). "Filter dissolution of C3S as a function of the lime concentration in a limited amount of lime water." *Cement and Concrete Research*, 10(4), 521–534.

Barret, P., Ménétrier, D., and Bertrandie, D. (1983). "Mechanism of C3S dissolution and problem of the congruency in the very initial period and later on." *Cement and Concrete Research*, 13(5), 728–738.

Bentz, D. P. (2006). "Influence of water-to-cement ratio on hydration kinetics: Simple models based on spatial considerations." *Cement and Concrete Research*, 36(2), 238–244.

Bentz, D. P., and Stutzman, P. E. (2006). "Curing, hydration, and microstructure of cement paste." *ACI Materials Journal*, 103(5), 348–356.

Bentz, D. P., Stutzman, P. E., Haecker, C., and Remond, S. (1999). "SEM/X-Ray Imaging of Cement-Based Materials." *Microscopy Applied to Building Materials, 7th Euroseminar Proceedings*, H. S. Pietersen, J. A. Larbi, and H. H. A. Janssen, eds., Delft University of Technology, Delft, NL, 457–466.

Berodier, E., and Scrivener, K. (2015). “Evolution of pore structure in blended systems.” *Cement and Concrete Research*, 73, 25–35.

Bhatty, J. I. (1986). “Hydration versus strength in a portland cement developed from domestic mineral wastes - a comparative study.” *Thermochimica Acta*, Elsevier, 106(C), 93–103.

Bullard, J. W., Jennings, H. M., Livingston, R. A., Nonat, A., Scherer, G. W., Schweitzer, J. S., Scrivener, K. L., and Thomas, J. J. (2011). “Mechanisms of cement hydration.” *Cement and Concrete Research*, Elsevier B.V., 41(12), 1208–1223.

Bumrongjaroen, W., Livingston, R. A., Neumann, D. A., and Allen, A. J. (2009). “Characterization of fly ash reactivity in hydrating cement by neutron scattering.” *Journal of Materials Research*, 24(7), 2435–2448.

Bumrongjaroen, W., Muller, I., Livingston, R. A., and Davis, J. (2011). “A Performance-based Fly Ash Classification System Using Glassy Particle Chemical Composition Data.” *World of Coal Ash*, Denver, CO.

Bye, G. C. (1999). “Portland cement: Composition, production and properties.” Thomas Telford, London.

Carette, G. G., and Malhotra, V. M. (1987). “Characterization of Canadian fly ashes and their relative performance in concrete.” *Canadian journal of civil engineering*, 14(5), 667–682.

Chancey, R. T., Stutzman, P., Juenger, M. C. G., and Fowler, D. W. (2010). “Comprehensive phase characterization of crystalline and amorphous phases of a Class F fly ash.” *Cement and Concrete Research*, 40(1), 146–156.

Corstanje, W. A., Stein, W. N., and Stevels, J. M. (1974). “Hydration reactions in pastes C3S + C3A + CaSO4 .2aq. + water at 25°C.III.” *Cement and Concrete Research*, 4(3), 417–431.

Cyr, M., Lawrence, P., and Ringot, E. (2006). “Efficiency of mineral admixtures in mortars: Quantification of the physical and chemical effects of fine admixtures in relation with compressive strength.” *Cement and Concrete Research*, 36(2), 264–277.

Deboucha, W., Leklou, N., Khelidj, A., and Oudjit, M. N. (2017). “Hydration development of mineral additives blended cement using thermogravimetric analysis (TGA): Methodology of calculating the degree of hydration.” *Construction and Building Materials*, 146, 687–701.

Deschner, F., Münch, B., Winnefeld, F., and Lothenbach, B. (2013). “Quantification of fly ash in hydrated, blended Portland cement pastes by backscattered electron imaging.” *Journal of Microscopy*, 251(2), 188–204.

Deschner, F., Winnefeld, F., Lothenbach, B., Seufert, S., Schwesig, P., Dittrich, S., Goetz-Neunhoeffer, F., and Neubauer, J. (2012). “Hydration of Portland cement with high replacement by siliceous fly ash.” *Cement and Concrete Research*, Elsevier Ltd, 42(10), 1389–1400.

Diamond, S. (1983). “On the glass present in low-calcium and in high-calcium fly ashes.” *Cement and Concrete Research*, 13(4), 459–464.

Doremus, R. H. (1994). *Glass science*. Wiley, New York :

Durdziński, P. T., Dunant, C. F., Haha, M. Ben, and Scrivener, K. L. (2015). “A new quantification method based on SEM-EDS to assess fly ash composition and

study the reaction of its individual components in hydrating cement paste." *Cement and Concrete Research*, 73, 111–122.

Durdziński, P. T., Ben Haha, M., Bernal, S. A., De Belie, N., Gruyaert, E., Lothenbach, B., Menéndez Méndez, E., Provis, J. L., Schöler, A., Stabler, C., Tan, Z., Villagrán Zaccardi, Y., Vollpracht, A., Winnefeld, F., Zając, M., and Scrivener, K. L. (2017). "Outcomes of the RILEM round robin on degree of reaction of slag and fly ash in blended cements." *Materials and Structures*, Springer Netherlands, 50(2), 135.

Esteves, L. P. (2011). "On the hydration of water-entrained cement-silica systems: Combined SEM, XRD and thermal analysis in cement pastes." *Thermochimica Acta*, 518(1–2), 27–35.

Fagerlund, G. (1973). "Determination of pore-size distribution from freezing-point depression." *Matériaux et Constructions*, Springer, 6(3), 215–225.

Feng, X., Garboczi, E. J., Bentz, D. P., Stutzman, P. E., and Mason, T. O. (2004). "Estimation of the degree of hydration of blended cement pastes by a scanning electron microscope point-counting procedure." *Cement and Concrete Research*, 34(10), 1787–1793.

Gallucci, E., Mathur, P., and Scrivener, K. (2010). "Microstructural development of early age hydration shells around cement grains." *Cement and Concrete Research*, 40(1), 4–13.

Garrault-Gauffinet, S., and Nonat, A. (1999). *Experimental investigation of calcium silicate hydrate (C-S-H) nucleation*. *Journal of Crystal Growth*.

Garrault, S., Finot, E., Lesniewska, E., and Nonat, A. (2005). "Study of C-S-H

growth on C3S surface during its early hydration." *Materials and Structures*, 38(4), 435–442.

Garrault, S., and Nonat, A. (2001). "Hydrated layer formation on tricalcium and dicalcium silicate surfaces: Experimental study and numerical simulations." *Langmuir*, 17(26), 8131–8138.

Gartner, E. M., Young, J. F., Damidot, D. A., and Jawed, I. (2002). "Hydration of Portland Cement." *Structure and Performance of Cements*, J. Bensted and P. Barnes, eds., Spon Press, New York, 57–113.

Goldstein, J. I., Newbury, D. E., Echlin, P., Joy, D. C., Lyman, C. E., Lifshin, E., Sawyer, L., and Michael, J. R. (2003). *Scanning Electron Microscopy and X-ray Microanalysis*. Springer US, Boston, MA.

Grutzeck, M. W., Fajun, W., and Roy, D. M. (1984). "Retardation Effects in the Hydration of Cement-Fly Ash Pastes." *MRS Proceedings*, Materials Research Soc, 43, 65.

Gruyaert, E. (2010). "Effect of Blast-Furnace Slag as Cement Replacement on Hydration, Microstructure, Strength and Durability of Concrete." Ghent University.

Gutteridge, W. A., and Dalziel, J. A. (1990). "Filler cement: the effect of the secondary component on the hydration of Portland cement: part I. A fine non-hydraulic fille." *Cement and Concrete Research*, Pergamon Press, 20(5).

Haha, M. Ben, De Weerdt, K., and Lothenbach, B. (2010). "Quantification of the degree of reaction of fly ash." *Cement and Concrete Research*, 40(11), 1620–1629.

Helmuth, R. (1987). *Fly ash in cement and concrete*. Portland Cement Association, Skokie, Ill.

Hemmings, R. T., and Berry, E. E. (1987). "On the Glass in Coal Fly Ashes: Recent Advances." *MRS Proceedings TA*, 113.

Hemmings, R. T., Berry, E. E., Cornelius, B. J., and Scheetz, B. E. (1986). "Speciation in Size and Density Fractionated Fly Ash II. Characterization of a Low-Calcium, High-Iron Fly Ash." *MRS Proceedings*, Cambridge University Press, 86, 81.

Igarashi, S., Kawamura, M., and Watanabe, A. (2004). "Analysis of cement pastes and mortars by a combination of backscatter-based SEM image analysis and calculations based on the Powers model." *Cement and Concrete Composites*, 26(8), 977–985.

Jawed, L., and Skalny, J. (1981). "Hydration of Tricalcium Silicate in the Presence of Fly Ash." *Proceedings, Symposium N, Effects of Fly Ash Incorporation in Cement and Concrete*, Materials Research Society, Pittsburgh, 60–69.

Jennings, H. M. (2008). "Refinements to colloid model of C-S-H in cement: CM-II." *Cement and Concrete Research*, 38(3), 275–289.

Juenger, M. C. G., and Siddique, R. (2015). "Recent advances in understanding the role of supplementary cementitious materials in concrete." *Cement and Concrete Research*, 78, 71–80.

Kadri, E. H., Aggoun, S., De Schutter, G., and Ezziane, K. (2010). "Combined effect of chemical nature and fineness of mineral powders on Portland cement hydration." *Materials and Structures*, 43(5), 665–673.

Kjeldsen, A. M., and Geiker, M. R. (2008). “On the interpretation of low temperature calorimetry data.” *Materials and Structures*, 41(1), 213–224.

Lasaga, A. C. (1981). “Rate laws in chemical reactions, in:” *Kinetics of Geochemical Processes, No.8 in Reviews in Mineralogy*, A. C. Lasaga and R. J. Kirkpatrick, eds., Mineralogical Society of America, 1–68.

Lawrence, P., Cyr, M., and Ringot, E. (2005). “Mineral admixtures in mortars effect of type, amount and fineness of fine constituents on compressive strength.” *Cement and Concrete Research*, 35(6), 1092–1105.

Livingston, R. A., and Bumrongjaroen, W. (2005). “Optimization of Silica Fume, Fly Ash and Cement Mixes for High Performance Concrete.” *World of Coal Ash (WOCA) Conference*, American Coal Ash Association, Lexington, KY.

Livingston, R. A., Bumrongjaroen, W., Essien, S., and Amde, A. M. (2019). “Application of Individual Glass Particle Data to Estimate Uncertainties in Bulk Fly Ash Chemical Compositions.” *Advances in Cement Analysis and Concrete Petrography, ASTM STP1613*, D. Chong and D. Broton, eds., ASTM International, West Conshohocken, PA, 41–54.

Lothenbach, B., Scrivener, K., and Hooton, R. D. (2011). “Supplementary cementitious materials.” *Cement and Concrete Research*, 41(12), 1244–1256.

Lyndon, J. W. (2005). *The measurement of the modal mineralogy of rocks from SEM imagery: the use of Multispec and ImageJ freeware*. *Geological Survey of Canada, Open File 4941*.

Massazza, F. (1998). “Pozzolana and Pozzolanic Cements.” *Lea’s Chemistry of Cement and Concrete*, P. C. Hewlett, ed., Elsevier, Oxford, 471–635.

McCarthy, G. J., SOLEM, J. K., Manz, O. E., and Hassett, D. J. (1989). "Use of a Database of Chemical, Mineralogical and Physical Properties of North American Fly Ash to Study the Nature of Fly Ash and Its Utilization as a Mineral Admixture in Concrete." *MRS Proceedings*, Cambridge University Press, New York, USA, 178.

McCarthy, G. J., Swanson, K. D., Keller, L. P., and Blatter, W. C. (1984). "Mineralogy of western fly ash." *Cement and Concrete Research*, Pergamon, 14(4), 471–478.

Minard, H., Garrault, S., Regnaud, L., and Nonat, A. (2007). "Mechanisms and parameters controlling the tricalcium aluminate reactivity in the presence of gypsum." *Cement and Concrete Research*, 37(10), 1418–1426.

Morel, F. M. . (1983). *Principles of Aquatic Chemistry*. Wiley-Interscience, New York.

Odler, I. (1998). "Hydration, Setting and Hardening of Portland Cement." *Lea's Chemistry of Cement and Concrete*, P. C. Hewlett, ed., Elsevier, Oxford, 241–297.

Oey, T., Timmons, J., Stutzman, P., Bullard, J. W., Balonis, M., Bauchy, M., and Sant, G. (2017). "An improved basis for characterizing the suitability of fly ash as a cement replacement agent." *Journal of the American Ceramic Society*, 100(10), 4785–4800.

Pane, I., and Hansen, W. (2005). "Investigation of blended cement hydration by isothermal calorimetry and thermal analysis." *Cement and Concrete Research*, 35(6), 1155–1164.

Pecharsky, V. K., and Zavalij, P. Y. (2009). *Fundamentals of Powder Diffraction and Structural Characterization of Materials*. *Powder Diffraction*.

Quennoz, A., and Scrivener, K. L. (2013). "Interactions between alite and C3A-gypsum hydrations in model cements." *Cement and Concrete Research*, 44, 46–54.

Richardson, I. G., and Groves, G. W. (1993). "The incorporation of minor and trace elements into calcium silicate hydrate (C-S-H) gel in hardened cement pastes." *CEMENT and CONCRETE RESEARCH*, 23, 131–138.

Ridi, F., Fratini, E., and Baglioni, P. (2013). "Fractal Structure Evolution during Cement Hydration by Differential Scanning Calorimetry: Effect of Organic Additives." *The Journal of Physical Chemistry C*, 117(48), 25478–25487.

Ridi, F., Luciani, P., Fratini, E., and Baglioni, P. (2009). "Water Confined in Cement Pastes as a Probe of Cement Microstructure Evolution Water Confined in Cement Pastes as a Probe of Cement Microstructure Evolution." *The journal of physical chemistry. B*, 113(10), 3080–7.

Roy, D. M., Luke, K., and Diamond, S. (1984). "Characterization of Fly Ash and its Reactions in Concrete." *MRS Proceedings*, Materials Research Soc, 43, 3.

Sakai, E., Miyahara, S., Ohsawa, S., Lee, S.-H., and Daimon, M. (2005). "Hydration of fly ash cement." *Cement and Concrete Research*, 35(6), 1135–1140.

Scrivener, K. L. (2004). "Backscattered electron imaging of cementitious microstructures: Understanding and quantification." *Cement and Concrete Composites*, 26(8), 935–945.

Scrivener, K. L., Füllmann, T., Gallucci, E., Walenta, G., and Bermejo, E. (2004).

"Quantitative study of Portland cement hydration by X-ray diffraction/Rietveld analysis and independent methods." *Cement and Concrete Research*, 34(9), 1541–1547.

Scrivener, K. L., Juilland, P., and Monteiro, P. J. M. (2015a). "Advances in understanding hydration of Portland cement." *Cement and Concrete Research*, 78, 38–56.

Scrivener, K. L., Lothenbach, B., De Belie, N., Gruyaert, E., Skibsted, J., Snellings, R., and Vollpracht, A. (2015b). "TC 238-SCM: hydration and microstructure of concrete with SCMs." *Materials and Structures*, 48(4), 835–862.

Scrivener, K. L., and Nonat, A. (2011). "Hydration of cementitious materials, present and future." *Cement and Concrete Research*, 41(7), 651–665.

Scrivener, K. L., Patel, H. H., Pratt, P. ., and Parrott, L. . (1986). "Analysis of Phases in Cement Pastes using Backscattered Electron Images, Methanol Adsorption and Thermogravimetric Analysis." *Materials Research Society Symposia Proceedings: Microstructural development during hydration of cement*, 85.

Siddique, R., and Khan, M. I. (2011). *Supplementary Cementing Materials*. Engineering Materials, Springer Berlin Heidelberg, Berlin, Heidelberg.

Snellings, R., Salze, A., and Scrivener, K. L. (2014). "Use of X-ray diffraction to quantify amorphous supplementary cementitious materials in anhydrous and hydrated blended cements." *Cement and Concrete Research*, Elsevier Ltd, 64, 89–98.

Snyder, K. A., and Bentz, D. P. (2004). "Suspended hydration and loss of freezable water in cement pastes exposed to 90% relative humidity." *Cement and Concrete*

Research, 34(11), 2045–2056.

Snyder, K. A., and Stutzman, P. E. (2013). *Hydrated Phases in Blended Cement Systems and Hydrated Phases in Blended Cement Systems and Synthetic Saltstone Grouts*.

Stein, H. N., and Stevels, J. M. (1964). "Influence of silica on the hydration of 3 CaO,SiO2." *Journal of Applied Chemistry*, John Wiley & Sons, Ltd, 14(8), 338–346.

Stutzman, P. (2007). "Multi-Spectral SEM Imaging of Cementitious Materials." *Proceedings of the 29th Conference on Cement Microscopy*, 1–13.

Takemoto, K., and Uchikawa, H. (1980). "Hydration of Pozzolanic Cement." *Proceedings of the 7th International Congress on the Chemistry of Cement*, 1.

Taylor, H. F. W. (1997). *Cement chemistry*. T. Telford, London :

Thomas, J. J., Allen, A. J., and Jennings, H. M. (2009). "Hydration kinetics and microstructure development of normal and CaCl 2-accelerated tricalcium silicate pastes." *Journal of Physical Chemistry C*, 113(46), 19836–19844.

Thomas, J. J., Biernacki, J. J., Bullard, J. W., Bishnoi, S., Dolado, J. S., Scherer, G. W., and Luttge, A. (2011). "Modeling and simulation of cement hydration kinetics and microstructure development." *Cement and Concrete Research*, 41(12), 1257–1278.

Thomas, M. D. A. (2013). *Supplementary cementing materials in concrete*. CRC Press/Taylor & Francis Group, Boca Raton, FL.

Vu, T.-H., Frizon, F., Lorente, S., and Vafai, K. (2010). "Application of Thermoporometry to Evaluate the Mesoporosity of Cement Pastes." 21(2010),

21–26.

Williams, P. J., Biernacki, J. J., Rawn, C. J., Walker, L., and Bai, J. (2005). "Microanalytical and Computational Analysis of Class F Fly Ash." *ACI Materials Journal*, American Concrete Institute, Farmington Hills, 102(5), 330.

Winburn, R. S., Grier, D. G., McCarthy, G. J., and Peterson, R. B. (2000). "Rietveld quantitative X-ray diffraction analysis of NIST fly ash standard reference materials." *Powder Diffraction*, 15(3), 163–172.

Worrell, E., Price, L., Martin, N., Hendriks, C., and Meida, L. O. (2001). "CARBON DIOXIDE EMISSIONS FROM THE GLOBAL CEMENT INDUSTRY." *Annual Review of Energy and the Environment*, Annual Reviews, 26(1), 303–329.

Zhang, J., and Scherer, G. W. (2011). "Comparison of methods for arresting hydration of cement." *Cement and Concrete Research*, Elsevier Ltd, 41(10), 1024–1036.

Zhao, H., and Darwin, D. (1992). "Quantitative backscattered electron analysis of cement paste." *Cement and Concrete Research*, 22(4), 695–706.